

Nanostructured Layers for Catalytic Applications

Guest Editors: M. R. Bayati, A. Kajbafvala, P. Sangpour,
and H. R. Zargar





Nanostructured Layers for Catalytic Applications

Nanostructured Layers for Catalytic Applications

Guest Editors: M. R. Bayati, A. Kajbafvala, P. Sangpour,
and H. R. Zargar



Copyright © 2012 Hindawi Publishing Corporation. All rights reserved.

This is a special issue published in "Journal of Nanomaterials." All articles are open access articles distributed under the Creative Commons Attribution License, which permits unrestricted use, distribution, and reproduction in any medium, provided the original work is properly cited.

Editorial Board

Katerina Aifantis, Greece
Nageh K. Allam, USA
Margarida Amaral, Portugal
Xuedong Bai, China
L. Balan, France
Enrico Bergamaschi, Italy
Theodorian Borca-Tasciuc, USA
C. Jeffrey Brinker, USA
Christian Brosseau, France
Xuebo Cao, China
Shafiul Chowdhury, USA
Cui ChunXiang, China
Miguel A. Correa-Duarte, Spain
Shadi A. Dayeh, USA
Ali Eftekhari, USA
Claude Estournes, France
Alan Fuchs, USA
Lian Gao, China
Russell E. Gorga, USA
Hongchen Chen Gu, China
Mustafa O. Guler, Turkey
John Zhanhu Guo, USA
Smrati Gupta, Germany
Michael Harris, USA
Zhongkui Hong, USA
Michael Z. Hu, USA
David Hui, USA
Y.-K. Jeong, Republic of Korea
Sheng-Rui Jian, Taiwan
Wanqin Jin, China
Rakesh K. Joshi, India
Zhenhui Kang, China
Fathallah Karimzadeh, Iran
Do Kyung Kim, Republic of Korea
Kin Tak Lau, Australia
Burtrand Lee, USA
Benxia Li, China
Jun Li, Singapore
Shijun Liao, China
Gong Ru Lin, Taiwan
J.-Y. Liu, USA
Jun Liu, USA
Tianxi Liu, China
Songwei Lu, USA
Daniel Lu, China
Jue Lu, USA
Ed Ma, USA
Gaurav Mago, USA
Sanjay R. Mathur, Germany
A. McCormick, USA
Vikas Mittal, UAE
Weihai Ni, Germany
Sherine Obare, USA
Edward Andrew Payzant, USA
Kui-Qing Peng, China
Anukorn Phuruangrat, Thailand
Ugur Serincan, Turkey
Huaiyu Shao, Japan
Donglu Shi, USA
Suprakas Sinha Ray, South Africa
Vladimir Sivakov, Germany
Marinella Striccoli, Italy
Bohua Sun, South Africa
Saikat Talapatra, USA
Nairong Tao, China
Titipun Thongtem, Thailand
Somchai Thongtem, Thailand
Valeri P. Tolstoy, Russia
Tsung-Yen Tsai, Taiwan
Takuya Tsuzuki, Australia
Raquel Verdejo, Spain
Mat U. Wahit, Malaysia
Shiren Wang, USA
Yong Wang, USA
Cheng Wang, China
Zhenbo Wang, China
Jinquan Wei, China
Ching Ping Wong, USA
Xingcai Wu, China
Guodong Xia, Hong Kong
Zhi Li Xiao, USA
Ping Xiao, UK
Shuangxi Xing, China
Yangchuan Xing, USA
N. Xu, China
Doron Yadlovker, Israel
Ying-Kui Yang, China
Khaled Youssef, USA
Kui Yu, Canada
William W. Yu, USA
Haibo Zeng, China
Tianyou Zhai, Japan
Renyun Zhang, Sweden
Yanbao Zhao, China
Lianxi Zheng, Singapore
Chunyi Zhi, Japan

Contents

Nanostructured Layers for Catalytic Applications, M. R. Bayati, A. Kajbafvala, P. Sangpour, and H. R. Zargar
Volume 2012, Article ID 502034, 2 pages

Modification of Clays by Sol-Gel Reaction and Their Use in the Ethylene In Situ Polymerization for Obtaining Nanocomposites, E. Moncada, R. Quijada, and P. Zapata
Volume 2012, Article ID 348156, 7 pages

Ti³⁺ in the Surface of Titanium Dioxide: Generation, Properties and Photocatalytic Application, Liang-Bin Xiong, Jia-Lin Li, Bo Yang, and Ying Yu
Volume 2012, Article ID 831524, 13 pages

Porous Diatomite-Immobilized CuNi Bimetallic Nanocatalysts for Direct Synthesis of Dimethyl Carbonate, Yong Chen, Min Xiao, Shuanjin Wang, Dongmei Han, Yixin Lu, and Yuezhong Meng
Volume 2012, Article ID 610410, 8 pages

ZnO Nanoparticles on Si, Si/Au, and Si/Au/ZnO Substrates by Mist-Atomisation, Z. Khusaimi, M. H. Mamat, N. Abdullah, and M. Rusop
Volume 2012, Article ID 872856, 8 pages

Fabrication of Photofunctional Nanoporous Membrane and Its Photoinactivation Effect of Vesicular Stomatitis Virus, Kang-Kyun Wang, Bong-Jin Kim, Si-Hwan Ko, Dong Hoon Choi, and Yong-Rok Kim
Volume 2012, Article ID 454507, 7 pages

Ag-Cu Bimetallic Nanoparticles Prepared by Microemulsion Method as Catalyst for Epoxidation of Styrene, Hong-Kui Wang, Chao-Yong Yi, Li Tian, Wen-Juan Wang, Jian Fang, Ji-Hua Zhao, and Wei-Guo Shen
Volume 2012, Article ID 453915, 8 pages

A Decrease in NiO-MgO Phase Through Its Solid Solution Equilibrium with Tetragonal (La_{1-z}Sr_z)₂Ni_{1-y}Mg_yO_{4-δ}: Effect on Catalytic Partial Oxidation of Methane, Xiong Yin, Liang Hong, and Zhengliang Gong
Volume 2012, Article ID 263568, 10 pages

Catalytic Activity of ZrO₂ Nanotube Arrays Prepared by Anodization Method, Xixin Wang, Jianling Zhao, Xiaorui Hou, Qi He, and Chengchun Tang
Volume 2012, Article ID 409571, 5 pages

The Physical Properties of Erbium-Doped Yttrium Iron Garnet Films Prepared by Sol-Gel Method, Ramadan Shaiboub, Noor Baa'yah Ibrahim, Mustafa Abdullah, and Ftema Abdulhade
Volume 2012, Article ID 524903, 5 pages

Editorial

Nanostructured Layers for Catalytic Applications

M. R. Bayati,¹ A. Kajbafvala,¹ P. Sangpour,² and H. R. Zargar³

¹ Department of Materials Science and Engineering, North Carolina State University, Raleigh, NC 27695, USA

² Materials and Energy Research Center, Tehran 19839, Iran

³ Department of Metals and Materials Engineering, The University of British Columbia, Vancouver BC, Canada V6T 1Z4

Correspondence should be addressed to M. R. Bayati, bayati@iust.ac.ir

Received 5 October 2011; Accepted 5 October 2011

Copyright © 2012 M. R. Bayati et al. This is an open access article distributed under the Creative Commons Attribution License, which permits unrestricted use, distribution, and reproduction in any medium, provided the original work is properly cited.

Higher energy consumption, which is a result of increasing the world population, gives rise to decreasing in fossil fuel reserves and creating environmental pollutions. Pollution is the introduction of contaminants into a natural environment that causes instability, disorder, harm, or discomfort to the ecosystem and can take the form of chemical substances or energy, such as noise, heat, or light. Remediation of the environmental pollutants is necessary. Since now three decades, advanced oxidation technologies “in particular photocatalysis” gained much attention by scientifics. In their point of view, to counter environmental pollutions, a simple and comprehensive photonic reaction system which converts the solar energy into the chemical energy of a redox system, namely, photocatalysis, would be helpful for the detoxification processes. Nowadays, heterogeneous photocatalysis is the most efficient method for destroying organic pollutants in especially aqueous media. This process is based on the use of ultraviolet or visible radiations to excite a semiconductor on whose surface the oxidation of the pollutants is performed. This special issue addresses advances in nanostructured layers for photocatalytic applications.

In the first paper of this special issue, ZnO nanoparticles were deposited on Si, Si/Au, and Si/Au/ZnO substrates by mist atomization, and effect of the substrates conditions on the structural, morphological, and photoluminescence properties of the nanoparticles was investigated. It was found that crystallite size and lattice strain were significantly affected by substrate surface type and temperature. Smallest crystallite size was obtained on Si/Au/ZnO at 400°C. The second paper deals with effect of Ti^{3+} on photocatalytic efficiency of titanium dioxide. The authors revealed that physical and chemical properties of TiO_2 were dominantly determined by its surface condition and especially presence of

Ti^{3+} species on its surface. A formation mechanism for the aforementioned defect was also proposed in this paper. Various generation methods for Ti^{3+} surface defect as well as its effect on optical and photocatalytic properties were discussed. It was shown that a detailed picture of Ti^{3+} surface defects would help to understand reactivity and overall material performance in photocatalytic applications. Ag-Cu bimetallic catalysts were prepared by microemulsion method, and their catalytic performance in epoxidation of styrene was evaluated in the third paper of this special issue. In this study, deposition of Ag-Cu bimetallic nanoparticles by the coreduction of Ag^+ and Cu^{2+} cations with $N_2H_4 \cdot H_2O$ as reductant on reticulate-like γ -alumina particles was studied. Ag-Cu bimetallic nanoparticles supported by γ -alumina showed better catalytic activity on the epoxidation of styrene as compared with the corresponding monometallic silver or copper catalysts. Herein, these could also be promising candidates for applications in many other reactions, namely, CO oxidation. In the next paper, porous diatomite immobilized Cu-Ni bimetallic nanocatalysts for direct synthesis of dimethyl carbonate. Upon various characterizations, it was shown that the bimetallic composite is effectively alloyed and well immobilized inside or outside the structural pores. In addition, the authors showed that existence of electron-rich and electron-deficient centers is resulted from the strong interaction of diatomite with Cu-Ni, and the synergy of Cu-Ni alloy may be responsible for the high performance of this catalyst. Fabrication of photofunctional nanoporous alumina membrane (PNAM) and its photoinactivation effect of vesicular stomatitis virus were reported in the fifth paper. To open the possibility for its environmental application, PNAM was applied for the removal of a virus without rendering cytotoxicity to the cells in vitro. The authors concluded

with the complete suppression of plaque-forming ability of vesicular stomatitis virus (VSV) by PNAM-mediated PACT (photodynamic antimicrobial chemotherapy). In the next paper entitled “*the physical properties of erbium-doped yttrium iron garnet films prepared by sol-gel method*” thin films of $\text{Er}_x\text{Y}_{3-x}\text{Fe}_5\text{O}_{12}$ were deposited through sol-gel method. These crystalline films were found to be soft magnetic materials. The saturation magnetization is reduced with Er substitution because the magnetic moments of Er^{3+} ions coupled antiferromagnetically to the effective moment formed by Fe^{3+} ions. The maximum coercivity was obtained at $x = 1.2$. In the next paper, a decrease in NiO-MgO phase through its solid solution equilibrium with tetragonal $(\text{La}_{1-z}\text{Sr}_z)_2\text{Ni}_{1-y}\text{Mg}_y\text{O}_{4-\delta}$ and its effect on catalytic partial oxidation of methane were investigated. The main concept of this study is utilizing the solid-state reaction equilibrium between the two solid solutions: the rock salt NiO-MgO and the tetragonal $(\text{La}_{1-z}\text{Sr}_z)_2\text{Ni}_{1-y}\text{Mg}_y\text{O}_{4-\delta}$ (LSNM) phase in order to reduce the size of NiO-MgO. This size reduction aimed to improve the coke resistance of the Ni^0 catalyst in the partial oxidation of methane (POM) without compromising the activity of catalyst. In the eighth paper, catalytic activity of ZrO_2 nanotube arrays prepared by anodizing method was studied, where nanotubes were prepared in aqueous electrolyte containing $(\text{NH}_4)_2\text{SO}_4$ and NH_4F . Calcination temperature and electrolyte concentration have a great influence on catalytic activity. Results indicate that nanotube arrays have highest catalytic activity when the concentration of $(\text{NH}_4)_2\text{SO}_4$ is 1 mol/L, the concentration of NH_4F is 1 wt%, and the calcination temperature is 400°C . Finally, modification of clays by sol-gel reaction and their use in the ethylene in situ polymerization for obtaining nanocomposites was reported. It was given away that the catalytic activity significantly increases when the clays were modified via sol-gel reaction under acidic or basic conditions compared with neutral condition.

M. R. Bayati
A. Kajbafvala
P. Sangpour
H. R. Zargar

Research Article

Modification of Clays by Sol-Gel Reaction and Their Use in the Ethylene *In Situ* Polymerization for Obtaining Nanocomposites

E. Moncada,¹ R. Quijada,^{2,3} and P. Zapata⁴

¹Grupo de Investigación en Materiales Avanzados y Energía, Centro de Investigaciones, Instituto Tecnológico Metropolitano, A.A 54959 Medellín, Colombia

²Departamento de Ingeniería Química, Facultad de Ciencias Físicas y Matemáticas, Universidad de Chile, Santiago, Chile

³Center for Advanced Interdisciplinary Research in Materials (CIMAT), Santiago, Chile

⁴Departamento de Química y Biología, Universidad Santiago de Chile, Santiago, Chile

Correspondence should be addressed to E. Moncada, edwinmoncada@itm.edu.co

Received 24 April 2011; Revised 11 August 2011; Accepted 30 August 2011

Academic Editor: Amir Kajbafvala

Copyright © 2012 E. Moncada et al. This is an open access article distributed under the Creative Commons Attribution License, which permits unrestricted use, distribution, and reproduction in any medium, provided the original work is properly cited.

The nanocomposites formation by *in situ* polymerization used a metallocene catalyst (butyl-2-cyclopentadienyl zirconium 2-chlorines) and a hectorite synthetic clay type which is discussed. This research was carried out in two phases. The first phase consisted of mixing the components of the metallocenic polymerization reaction (metallocene-methylaluminoxane-ethylene) with clay in a reactor. In the second phase, the metallocenic catalytic system was supported by clay particles and then a polymerization reaction was made. In this second phase, the clay particles were modified using a sol-gel reaction with different pH values: pH = 3, pH = 8, and pH = 12. The results were compared in terms of the catalytic activity in the different systems (phase 1 and phase 2) and the nanoparticle morphology of nanocomposites generated in this study.

1. Introduction

Inorganic nanoparticles filled in the polymer composites have received increased interest from material scientists. The filler/matrix interface in these nanocomposites might constitute a greater area and hence influence the composites properties to a greater extent with a low filler concentration, in comparison with conventional microparticles composites.

A number of polyolefin nanocomposites based on layered silicates have recently been studied [1, 2] and commercialized, such as the poly(propylene)-clay nanocomposites pioneered by General Motors, Basell, and Southern Clay in 2002 [3]. Several methods have been employed to produce polymer nanocomposites with a desired improved mechanical, thermal, optical and gases barriers (O₂, N₂, etc.), or other properties. These methods range from simply mixing polymer with fillers to more elaborated approaches such as *in situ* polymerization [4–10]. A key aspect in the preparation of inorganic/organic nanocomposite materials is the establishment of a good interaction between the polymer matrix and the nanoparticle.

Despite the prime importance of polyolefins in diverse applications, the synthesis of polyolefin-inorganic nanocomposites still remains a scientific challenge because of the poor compatibility of polyolefins with ionic silicates. Although melting intercalation could generate polyolefin nanocomposites [11, 12], in the *in situ* polymerization it has proved to be a promising method for preparing fully exfoliated nanocomposites of polyolefins [13–20]. Tudor et al. [13] reported that a low molecular weight PP was produced after the methylaluminoxane (MAO) activation of a cationic Ziegler-Natta catalyst. This had been ion-exchanged into the clay interlayer's, but dispersed nanocomposites were not obtained. Bergman et al. [15] intercalated a Brookhart catalyst cationic palladium-based into galleries of an organically modified fluorohectorite and obtained a rubbery polyethylene/clay nanocomposite. More recently, Alexandre et al. [21] prepared PE/clays nanocomposites using a polymerization-filling technique with a Ti-based geometry catalyst. During the polymerization, a chain transfer agent was added to obtain highly crystalline nanocomposites with improved mechanical properties.

Recent research studies have been carried out on the catalytic activity during the formation of polyethylene (PE)/clay nanocomposites by *in situ* polymerization with metallocenes. The modification of the clay with MAO catalyst and the intercalation with octadecylamine (ODA) surfactant were found to play an important role during the *in situ* formation of PE/clay nanocomposite. ODA-intercalated clay apparently facilitates the activation and monomer insertion processes on zirconocene centers located in internal sites of the clay structure [22].

Nanoparticles are commonly obtained either by the sol-gel method or by the intercalation method. Sol-gel nanocomposites (polymer/silica nanocomposites) are prepared by *in situ* hydrolysis and the condensation of mononuclear precursors such as tetraethoxysilane (TEOS) and tetramethoxysilane in organic polymer matrices [23–25]. On the other hand, nanoparticles are obtained by two different methods: The exfoliation of clays or the sol-gel method. Sol-gel nanoparticles are prepared by hydrolysis and condensation of mononuclear precursors such as tetraethoxysilane (TEOS) and tetramethoxysilane in organic polymer matrices [26].

In the literature there is a lot of work which uses sol-gel nanoparticles as a nanofiller [27], but no one has explored the different sol-gel reaction conditions which are aimed to obtain and modify morphology and different characteristics of nanoparticles. During this work the modification of clay was studied using sol-gel reaction at different pH value. Also the modified clay was used in the obtaining of nanocomposites by *in situ* polymerization. The present work was divided in two different phases. In the first phase (PHASE I) the components of the reaction, MAO, metallocene, and ethylene, were mixed with clay and the homogeneous polymerization was made. In the second phase (PHASE II), the clay was modified with sol-gel at different pH values and thereafter the metallocene was supported in the modified clay and the heterogeneous polymerization was made. The activity of the different catalytic system was compared with the dispersion of clay and/or nanoparticles in the nanocomposites obtained.

2. Experimental Section

2.1. Materials. The employed clay, synthetic hectorite (HS), was donated by Netherland Organization for Applied Scientific Research—TNO. The characteristics of this clay are described elsewhere [28]. For modification of the clay, tetraethoxy silane (TEOS) of Aldrich and metilaluminoxane (MAO; Witco) were used. The metallocene *butyl-2-cyclopentadienyl zirconium 2-chlorine* was used for ethylene polymerization catalyst which had MAO as the cocatalyst. Ethylene was deoxygenated and dried by passing through columns of Cu catalyst (BASF) and activated by molecular sieve (13X), respectively. Toluene (solvent) was purified by refluxing, and it was freshly distilled under nitrogen from an Na/benzophenone system. All manipulations during the catalyst were carried out in an inert nitrogen atmosphere using the Schlenk technique.

2.2. Methods

2.2.1. Clay. The clays used in the homogeneous polymerization were used without previous treatment.

2.2.2. Modified Clays. The clay was modified by a sol-gel reaction using tetraethylortosilicate (TEOS) at different pH values. In a typical procedure, ca. 2.0 g of clay was dispersed in ethanol and stirred for 10 minutes. Then HCl or NH₄OH drops (depending on the pH value) were added wisely up to reaching pH = 3.0 (T3), pH = 8.0 (T8), or pH = 12.0 (T12). Thereafter, 10 mL of TEOS was added under inert conditions. After 1 h, the suspension was washed, filtered, and the particles were dried at 200°C for a 12-hour period.

2.2.3. Preparation of the Supported Metallocene. Two grams of modified clay were previously dried with a vacuum for six hours at 130°C, then the clay particles were dispersed in 30 mL of purified toluene and placed in contact with 2 mL of MAO 1.66 mol/L for 3 hours with magnetic bar at 70°C. The slurry was then filtered through a glass filter. The solid was washed several times with toluene at 60°C and dried for 4 hours in a vacuum at room temperature. Then an amount of metallocene in solution was added with the metallocene in toluene solution for 3 hrs at 70°C. The slurry was filtered in a Schlenk equipped with a fritted/filter glass, and washed with toluene. The filtrate was stored and used for the ethylene polymerization. The samples obtained are:

HS T3 = catalytic system supported with modification sol-gel to pH = 3.

HS T8 = catalytic system supported with modification sol-gel to pH = 8.

HS T12 = catalytic system supported with modification sol-gel to pH = 12.

2.2.4. Homopolymerization Reaction. The polymerizations were carried out in a 1-liter Büchi autoclave reactor equipped with a temperature and internal pressure control system with a stirrer. The reactor was coupled to a Brook model 5860E ethylene flowmeter and connected to data recording software to monitor the consumption of monomer during the course of the reaction.

Catalyst was dissolved in a solvent (500 mL toluene) and it was introduced in the reactor by nitrogen overpressure and the necessary amount of MAO was also added. After evacuating the nitrogen from the reactor, the reaction started by introducing the ethylene until the desired pressure was reached. Reaction time was 30 minutes. The solvent volume was adjusted in such a way that the total volume inside the reactor was 500 mL. The reaction was stopped by the addition of a solution of acidified methanol (HCl 20%). The polymer was recovered through filtration and washed with methanol and acetone. Finally, the product was dried at room temperature.

Phase 1 (homogeneous polymerization in the presence of clay). The effect of clay addition in the homogeneous polymerization (interaction of clay with MAO and catalyst

TABLE 1: The addition of component sequences to the catalytic system of polymerization reactions.

Addition sequence	Code
Clay-MAO-catalyst	Hs-MAO-Cat
MAO-clay-catalyst	MAO-Hs-Cat
MAO-catalyst-clay	MAO-Cat-Hs

TABLE 2: The effect of the addition of catalytic system in the homopolymerization reaction.

Code	Conditions of preparation
HsT3	Metallocene supported in modification clay using sol-gel to pH = 3
HsT8	Metallocene supported in modification clays using sol-gel to pH = 8
HsT12	Metallocene supported in modification clays using sol-gel to pH = 2

TABLE 3: The effects of the components addition in the reaction characteristics using the catalyst (n-BuCp)₂Zr Cl₂.

System	Activity (kg·pol/mol*bar*h)	Clay (%)	Temperature of reactor
Homogeneous	12000	—	49–80
Hs-MAO-Cat	10210	1.2	49–80
MAO-Hs-Cat	10409	1.0	49–80
MAO-Cat-Hs	9100	1.1	49–63

Clay added (g) = 0.32,
mol Zr in the reactor = 3.06E-06,
ratio Al/Zr = 1400,
reaction time (hours) = 0.5.

in different sequence) was carried out on three different reactions. In all reactions, the ethylene was added at the start to the reactor. After that, the catalytic system component was introduced. The addition of component sequences to the catalytic system of polymerization reactions is shown in the Table 1. The aim of this study was to determine the condition of the effect in the polymerization reaction.

Phase 2 (heterogeneous polymerization). The reaction conditions were the same as those of the homogenous polymerization.

Three different samples were obtained and are listed in Table 2.

2.3. Characterization. The molecular weights and their distribution of the produced polyethylene were determined by gel permeation chromatography (GPC) in a Waters Alliance 2000 system equipped with a differential optical refractometer detector. Three separation columns, HT6E, HT5, and HT3 were previously calibrated with narrow molecular weight distribution polystyrene standards which were used. A 1,2,4-trichlorobenzene was used as the solvent. The flow rate for the analysis was 1 mL min⁻¹ at 135°C.

The morphology of the silica nanospheres and its dispersion in the composites were analyzed by transmission

electronic microscopy (TEM: JEOL, JEM-1200EXII). Ultra-thin specimens with a thickness of about 60 nm were cut with glass and/or diamond blades by using a cryogenic-ultramicrotome Leica model EMFCS at -80°C.

3. Results and Discussions

3.1. Phase 1

3.1.1. Establishment of the Reaction Conditions to Obtain Polyethylene Nanocomposites by Means of In Situ Polymerization. The first phase aimed to establish the optimized conditions for obtaining nanocomposites with clay material (1 wt.-%). Besides, it also studied the effects of other components (clay, MAO, and catalysts) in the catalytic activity. With this, the clay percentage in the nanocomposite can be determined. Also characteristics such as morphology and dispersion of the nanoparticles in the nanocomposite were investigated.

3.1.2. The Effects of the Addition of Components in the Polymerization Reaction. Shown in Table 1 is the influence of the addition of component sequences to the catalytic system of polymerization reactions and physical properties of nanocomposites. The results of polymerization reaction are shown in the Table 3, where a low decrease in the catalytic activity for the reactions in which clay was added is observed.

On the other hand, there were not many differences between the HS-MAO-Cat and MAO-HS-Cat systems. With MAO-Cat-Hs system a decrease in the catalytic activity was observed, reaching values of 9100 kg·pol/mol Zr*bar*h. It could be because in Hs-MAO-Cat and MAO-Cat-Hs the interaction between the MAO and the clay was done first, which inactivated the polar groups coming from clay that could deactivate the catalyst. In the MAO-Cat-Hs the clay was added when both (MAO and the catalyst) were in the reaction, slightly deactivating the catalyst.

Through observation of experimental data from the followup of the reaction in the temperature peak, a higher control in the polymerization reaction was found. For the MAO-Cat-Hs system, the temperature ranged between 49°C and 63°C (T reactor) while for the two other systems, it was between 49°C and 80°C (similar to the homogeneous reaction). This better control in the polymerization temperature could be due to the active specie stabilization MAO-Cat-Hs, because these two components were added in consecutive order, different to Hs-MAO-Cat and MAO-Hs-Cat systems. The clay percentage found in all the composites obtained was around 1%.

The physical characteristics of the resulting nanocomposites are shown in Table 4. There are no significant variations between the properties for the polymers produced in the presence of clays particles and what was obtained in the homogenous reaction (neat polyethylene without clay). Only the molecular weight (Mw) of the obtained polymers shows a difference according to the catalytic system: for MAO-Cat-Hs, Mw = 264 kg/mol. It is bigger than that found in other systems, even for the homopolymerization reaction.

TABLE 4: Physical characteristics of polyethylene nanocomposites obtained with the three different polymerization systems already studied.

System	Crystallinity (%)	Tc (°C)	Tf (°C)	Mw (kg/mol)	Mw/Mn
Homogenous	75	118	135	164	2.1
Hs-MAO-Cat	76	118	135	176	2.3
MAO-Hs-Cat	74	118	134	167	2.3
MAO-Cat-Hs	72	118	133	264	2.4

This is in agreement with the highest control of the reaction temperature (49°C–63°C) achieved for this system.

This better control of temperature might have minimized chain transfer and the beta elimination reactions, which are responsible for decreasing molecular weight during polymerization reaction. Apparently, for Hs-MAO-Cat and MAO-Hs-Cat systems, the behavior of the supported catalyst system is similar to that described by Tait: a bidimensional liquid, which favors the mobility of the active species. Which in turn produces polymers with characteristics closer to those obtained with the homogeneous systems [29]. It is worth noting that the supported species are indeed different in the third case, which seems as if it is really acting as a heterogeneous catalytic: species are immobilized and there is a lower probability of bimolecular deactivation reactions. Therefore polymer molecular weight increases [30]. To sum up, MAO-Cat-Hs showed the best conditions for the best control in the reaction and produced polymers of higher molecular weight. Therefore, in the next stage this system was further exploited. The melting and Crystallinity temperature of the nanocomposites did not significantly change compared to the neat PE, indicating the formation of linear polyethylene.

3.2. Phase 2

3.2.1. The Effects of Clay Modification by Means of the Sol-Gel Method with Different pH Values and Their Use as a Supported Metallocene System. Clay modifications were carried out by means of sol-gel synthesis at different pH values in order to identify its effect on the particle morphology during the sol-gel reaction as well as in the properties of resulting nanocomposites.

It is known that the sol-gel method allows the morphology manipulation of the particles as well as its size, depending on the pH value in which the synthesis is carried out [25, 31–33] as follows: for pH basic values (pH = 12) spherical morphologies are formed; where pH acid fibrillar morphologies (pH = 3) are obtained. With pH near to neuter values it is preferred to form morphologies in nets with fibrillar characteristics (pH = 8).

This modification of clay characteristics is carried out in order to increase its interlaminar space (due to the formation of these compounds within the interlaminar region) in order to easily render the dispersion of the nanosheets within the polymer. Furthermore, the influence of the particles morphology in the MAO-metallocene systems was investigated.

Three new systems were established for this phase by supporting the metallocene catalysts in the modified clay at different pH values, the samples are listed in Table 2.

Table 5 shows the reaction conditions established for the modified clay by means of sol-gel reaction at different pH values. The impregnation reactions of the catalyst in the different systems were done with similar amounts (0.72 g). The quantity of supported catalytic and experimentally obtained were more efficient for pH values of 3 and 8 than for a pH value of 12. When the modification of pH = 12 was used, a lower catalyst loading into the modified clay was achieved. This smaller incorporation could be due to the reduced number of OH groups resulting from the treatment with alkaline pH. One cannot neglect that different texture properties may also affect further research necessary to clarify this point.

On the other hand, for all the three cases, a considerable decrease in catalyst activity was observed when it was supported in modified clay by sol-gel reaction. Comparing it with both, the homopolymerization and the heterogeneous reactions (when the clay was added directly to the reactor without supporting it), the highest decrease in catalytic activity was observed in the case of HsT8 (up to 84%). For HsT3 and HsT12, the decrease in catalyst activity is low compared to the HsT8 system: its value is roughly one half of that obtained in the case of homopolymerization reaction. This decrease effect of catalytic activity with the clay support has been widely studied [34]. It is probably due to the clay surface which should work like an extremely huge ligand, proving more difficult to render access to the monomer.

The catalytic systems, which involved extreme pH values, that is, HsT3 (pH = 3) and HsT12 (pH = 12), showed higher catalyst activity in comparison to that carried out with HsT8 system. This behavior can be attributed to the potential generation of a higher OH density on the clay surface (when high basic or acid pH value are used, a higher amount of OH group are formed) which acts as capacitor plate, depending on the pH media.

The higher the OH density, the better it can afford a better interaction between the clay surface and MAO, which in turn allows the metallocene catalytic to be a more positive load in their active center and also to present an increase in the catalytic activity. Comparing this with the HsT8 system (pH = 8), which does not present a big formation of OH sites, therefore the MAO stays chemically more available to interact with catalytic and to decrease the activity as well.

It was observed that the modification with the sol-gel method in different pH values has a big influence on the metallocene catalytic system. It was obtained that acid pH values (pH = 3) and basic (pH = 12) show greater activity values compared to intermediate pH values (pH = 8). As one expects, this behavior (that the nanoparticle morphology depending on the pH) could have big repercussions in the mechanical properties of the obtained nanocomposites.

3.2.2. Transmission Electronic Microscopy. Figure 1 shows the TEM images of the different obtained nanocomposites. It can be appreciated that for the two phases, it found a good dispersion of nanoparticles in the polyethylene matrix and

TABLE 5: The effects of modification to clay using sol-gel, in the reaction conditions of polyethylene nanocomposites.

System	System (g)	% Zr (experimental)	Activity (kg·pol/mol*bar*h)	Clay %
Homogeneous	—	—	12000	—
HsT3	0.044	0,64	5142	0.3
HsT8	0.046	0,64	1901	0.8
HsT12	0.052	0,53	5250	0.4

Catalytic system (g) = 0.048,
 % Zr theoretical = 0.72,
 mol Zr in reactor = $3.08E - 06$,
 ratio Al/Zr = 1400,
 time of reaction (h) = 0.5.

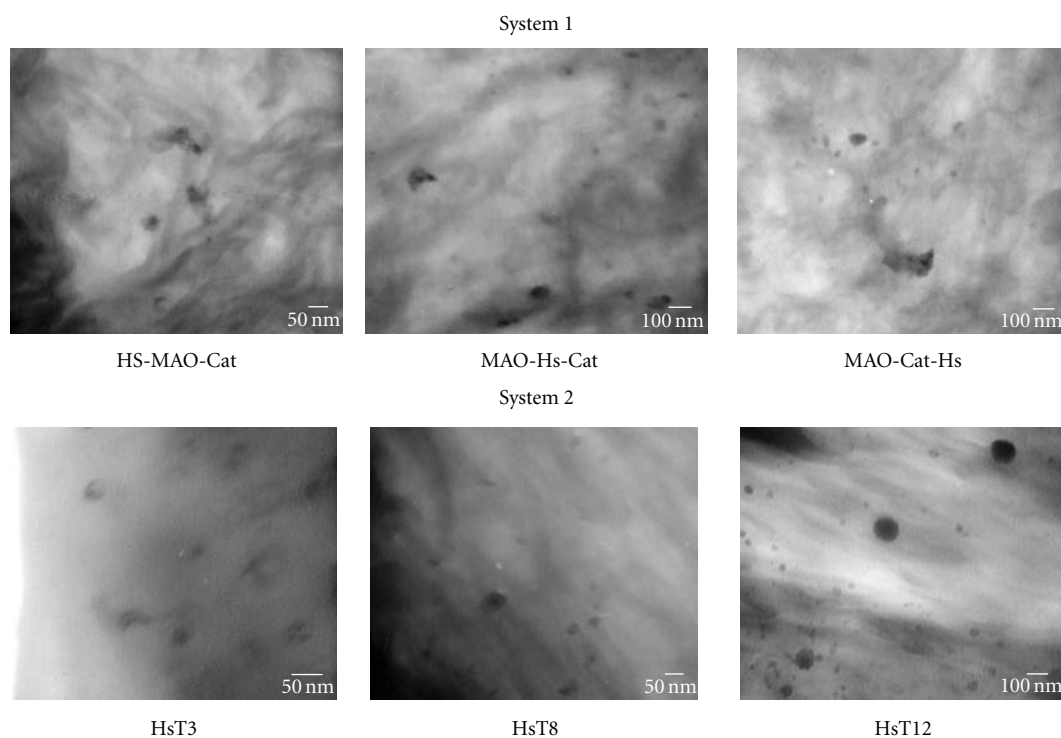


FIGURE 1: Transmission electronic microscopy images of different obtained nanocomposites.

various morphology nanoparticles were discovered. This could be because the clay used was synthetic and it could suffer a breaking of the laminated structure that changes the morphologies after of modification with sol-gel reaction.

In Figure 1 the first phase presents agglomerations of nanoparticles. Only in the MAO-Cat-Hs system is it possible to see agglomeration with greater size particles to 100 nm (nanoparticles of sizes lower than 100 nm and aggregates of approximately 200 nm); this system did not get a total exfoliation. For the two other studied systems, different sizes in nanoparticles were principally found, but all of them were lower than 100 nm in the polymeric matrix. What is mentioned above allows it to establish an adequate nanocomposites formation for the three studied systems.

In Figure 1 the second phase shows different morphologies of particles depending on pH value to which the clays were modified.

The particles modified with pH = 3 (with this condition of sol-gel reaction, fiber is the preferable morphology) can be observed in small aggregates with 5–10 sheets or fibers dispersed in the polymer. The size of these aggregates average from 20 nm in thickness and the length can reach 70 nm.

When the clay modification was carried out to a pH = 8 it was observed that the particles morphology, its distributions, and its size were similar to the results obtained in phase 1, showing nanoparticles dispersed in the polymer.

When the clay modification was at a pH = 12, it was possible to observe a preferably spherical morphology, which is normal in the morphology that was obtained for the sol-gel reaction at basic pH values. The different size particles were obtained from 5 nm to approximately 100 nm.

Evidently, the clay particles adopted a particle morphology generated by the sol-gel reaction; this would imply very strong sol-gel reaction conditions to be supported by

synthetic clay as the case in this research. Due to this fibrillates, layered, or spherical morphologies can be obtained, depending on the conditions of modification. On the other hand, smaller-sized particles were obtained through clay modifications with the sol-gel method, without taking into account the pH value used to compare it with the clay addition to the catalytic system.

4. Conclusion

The modifications of the layer of clays using the sol-gel technique at different pH values present new characteristics for the modification of the clays.

The clays modified with sol-gel technique at different pH values, present big modifications in the morphology, when used as catalytic support in the obtention of *in situ* polyolefins nanocomposites.

The catalytic activity presents large increases when the layers was modified with sol-gel reaction in acidic or a basic condition compared with neutral condition and with other works of the literature.

Best dispersion of nanoparticles is obtained when the clays are modified with sol-gel technique in the obtention of *in situ* nanocomposites.

Acknowledgments

The authors acknowledge the financial support of CONICYT under Projects FONDAP 11980002 and Fondecyt 1050651. The supply of commercial polypropylene clays by Dr. Hartmut Fischer from the Netherland Organization for Applied Scientific Research—TNO, is gratefully acknowledged. Special thanks are to Professor Dr. Gerhard Wegner and Dr. Ingo Lieberwirth of the Max Planck Institute for Polymer Research, Mainz, Germany, for providing the TEM equipment. E. Moncada thanks Professor Dr. João Henrique dos Santos of Universidade Federal do Rio Grande do Sul, Porto Alegre, Brazil, for the collaboration in the discussion of the result, and the Deutscher Akademischer Austauschdienst (DAAD) for a Ph.D. fellowship.

References

- [1] E. P. Giannelis, "Polymer layered silicate nanocomposites," *Advanced Materials*, vol. 8, no. 1, pp. 29–35, 1996.
- [2] R. A. Vaia, K. D. Jandt, E. J. Kramer, and E. P. Giannelis, "Microstructural evolution of melt intercalated polymer-organically modified layered silicates nanocomposites," *Chemistry of Materials*, vol. 8, no. 11, pp. 2628–2635, 1996.
- [3] R. Stewart, "Nanocomposites: microscopic reinforcements boost polymer performance," *Plastics Engineering*, vol. 60, no. 5, pp. 22–29, 2004.
- [4] P. Judeinstein and C. Sanchez, "Hybrid organic-inorganic materials: a land of multidisciplinary," *Journal of Materials Chemistry*, vol. 6, no. 4, pp. 511–525, 1996.
- [5] G. Kickelbick, "Concepts for the incorporation of inorganic building blocks into organic polymers on a nanoscale," *Progress in Polymer Science*, vol. 28, no. 1, pp. 83–114, 2003.
- [6] N. Y. Kim, N. L. Jeon, I. S. Choi et al., "Surface-initiated ring-opening metathesis polymerization on Si/SiO₂," *Macromolecules*, vol. 33, no. 8, pp. 2793–2795, 2000.
- [7] C. M. Chan, J. Wu, J. X. Li, and Y. K. Cheung, "Polypropylene/calcium carbonate nanocomposites," *Polymer*, vol. 43, no. 10, pp. 2981–2992, 2002.
- [8] R. C. Advincula, "Surface initiated polymerization from nanoparticle surfaces," *Journal of Dispersion Science and Technology*, vol. 24, no. 3-4, pp. 343–361, 2003.
- [9] Y. M. Cao, J. Sun, and D. H. Yu, "Swelling kinetics of poly(N-vinylimidazole-co-sodium styrenesulfonate) hydrogels," *Journal of Applied Polymer Science*, vol. 83, no. 1, pp. 191–200, 2002.
- [10] M. W. Weimer, H. Chen, E. P. Giannelis, and D. Y. Sogah, "Direct synthesis of dispersed nanocomposites by in situ living free radical polymerization using a silicate-anchored initiator," *Journal of the American Chemical Society*, vol. 121, no. 7, pp. 1615–1616, 1999.
- [11] M. Kawasumi, N. Hasegawa, M. Kato, A. Usuki, and A. Okada, "Preparation and mechanical properties of polypropylene-clay hybrids," *Macromolecules*, vol. 30, no. 20, pp. 6333–6338, 1997.
- [12] H. G. Jeon, H. T. Jung, S. W. Lee, and S. D. Hudson, "Morphology of polymer/silicate nanocomposites: high density polyethylene and a nitrile copolymer," *Polymer Bulletin*, vol. 41, no. 1, pp. 107–113, 1998.
- [13] J. Tudor, L. Willington, D. O'Hare, and B. Royan, "Intercalation of catalytically active metal complexes in phyllosilicates and their application as propene polymerisation catalysts," *Chemical Communications*, no. 17, pp. 2031–2032, 1996.
- [14] J. Tudor and D. O'Hare, "Stereospecific propene polymerisation catalysis using an organometallic modified mesoporous silicate," *Chemical Communications*, no. 6, pp. 603–604, 1997.
- [15] J. S. Bergman, H. Chen, E. P. Giannelis, M. G. Thomas, and G. W. Coates, "Synthesis and characterization of polyolefin-silicate nanocomposites: a catalyst intercalation and in situ polymerization approach," *Chemical Communications*, no. 21, pp. 2179–2180, 1999.
- [16] J. Heinemann, P. Reichert, R. Thomann, and R. Mülhaupt, "Polyolefin nanocomposites formed by melt compounding and transition metal catalyzed ethene homo- and copolymerization in the presence of layered silicates," *Macromolecular Rapid Communications*, vol. 20, no. 8, pp. 423–430, 1999.
- [17] M. Alexandre, P. Dubois, R. Jerome et al., "Polyolefin nanocomposites," *US Patent*, no. WO 9947598, 1999.
- [18] J. Wang, Z. Liu, C. Guo, Y. Chen, and D. Wang, "Preparation of a PE/MT composite by copolymerization of ethylene with in-situ produced ethylene oligomers under a dual functional catalyst system intercalated into MT layer," *Macromolecular Rapid Communications*, vol. 22, no. 17, pp. 1422–1426, 2001.
- [19] Y. H. Jin, H. J. Park, S. S. Im, S. Y. Kwak, and S. Kwak, "Polyethylene/clay nanocomposite by in-situ exfoliation of montmorillonite during Ziegler-Natta polymerization of ethylene," *Macromolecular Rapid Communications*, vol. 23, no. 2, pp. 135–140, 2002.
- [20] Q. Wang, Z. Zhou, L. Song, H. Xu, and L. Wang, "Nanoscale confinement effects on ethylene polymerization by intercalated silicate with metallocene catalyst," *Journal of Polymer Science A*, vol. 42, no. 1, pp. 38–43, 2004.
- [21] M. Alexandre, P. Dubois, T. Sun, J. M. Garces, and R. Geronime, "Polyethylene-layered silicate nanocomposites prepared by the polymerization-filling technique: synthesis and mechanical properties," *Polymer*, vol. 43, no. 8, pp. 2123–2132, 2002.

- [22] P. Zapata, R. Quijada, C. Covarrubias, E. Moncada, and J. Retuert, "Catalytic activity during the preparation of PE/clay nanocomposites by in situ polymerization with metallocene catalysts," *Journal of Applied Polymer Science*, vol. 113, no. 4, pp. 2368–2377, 2009.
- [23] H. P. Lin and M. Chung-Yuan, "Structural and morphological control of cationic surfactant-templated mesoporous silica," *Accounts of Chemical Research*, vol. 35, no. 11, pp. 927–935, 2002.
- [24] W. K. Dong, A. Blumstein, J. Kumar, and S. Tripathy, "Layered Aluminosilicate/Chromophore Nanocomposites and Their Electrostatic Layer-by-Layer Assembly," *Chemistry of Materials*, vol. 13, pp. 243–246, 2001.
- [25] G. J. D. A. A. Soler-Illia, C. Sanchez, B. Lebeau, and J. Patarin, "Chemical strategies to design textured materials: from microporous and mesoporous oxides to nanonetworks and hierarchical structures," *Chemical Reviews*, vol. 102, no. 11, pp. 4093–4138, 2002.
- [26] W. Liangming, T. Tao, and H. Baotong, "Synthesis and characterization of polyethylene/clay-silica nanocomposites: a montmorillonite/silica-hybrid-supported catalyst and in situ polymerization," *Journal of Polymer Science A*, vol. 42, no. 4, pp. 941–949, 2004.
- [27] P. Zapata, R. Quijada, and R. Benavente, "In situ formation of nanocomposites based on polyethylene and silica nanospheres," *Journal of Applied Polymer Science*, vol. 119, no. 3, pp. 1771–1780, 2011.
- [28] E. Moncada, R. Quijada, and J. Retuert, "Comparative effect of metallocene and Ziegler-Natta polypropylene on the exfoliation of montmorillonite and hectorite clays to obtain nanocomposites," *Journal of Applied Polymer Science*, vol. 103, no. 2, pp. 698–706, 2007.
- [29] A. M. Johannes and J. T. Peter, "The "comonomer effect" in ethylene/ α -olefin copolymerization using homogeneous and silica-supported Cp_2ZrCl_2/MAO catalyst systems: Some insights from the kinetics of polymerization, active center studies, and polymerization temperature," *Journal of Polymer Science A*, vol. 46, no. 1, pp. 267–277, 2007.
- [30] W. Kaminsky and F. Renner, "High melting polypropylenes by silicasupported zirconocene catalysts," *Die Makromolekulare Chemie, Rapid Communications*, vol. 14, no. 4, p. 239, 1993.
- [31] E. Moncada, R. Quijada, and J. Retuert, "Nanoparticles prepared by the sol-gel method and their use in the formation of nanocomposites with polypropylene," *Nanotechnology*, vol. 18, no. 33, Article ID 335606, 2007.
- [32] M. Ogawa, "Preparation of layered silicodialkyldimethylammonium bromide nanocomposites," *Langmuir*, vol. 13, no. 6, pp. 1853–1855, 1997.
- [33] S. K. Yun and J. Maier, "Layered and hexagonal aluminosilicate-hexadecylamine mesostructures: solid state transformation and ionic conductivity," *Inorganic Chemistry*, vol. 38, no. 3, pp. 545–549, 1999.
- [34] F. C. Franceschini, T. T. D. R. Tavares, J. H. Z. Dos Santos, M. L. Ferreira, and J. B. P. Soares, "Ethylene and propylene polymerization using in situ supported $Me_2Si(Ind)_2ZrCl_2$ Catalyst: experimental and theoretical study," *Macromolecular Materials and Engineering*, vol. 291, no. 3, pp. 279–287, 2006.

Review Article

Ti³⁺ in the Surface of Titanium Dioxide: Generation, Properties and Photocatalytic Application

Liang-Bin Xiong,^{1,2} Jia-Lin Li,³ Bo Yang,² and Ying Yu³

¹ Physics Department, Huanggang Normal University, Huanggang 438000, China

² Hubei Silver Dragon Pipe Industrial Co., LTD, Ezhou 436000, China

³ Institute of Nanoscience and Nanotechnology, Central China Normal University, Wuhan 430079, China

Correspondence should be addressed to Ying Yu, yuying@phy.ccn.u.edu.cn

Received 21 May 2011; Accepted 26 August 2011

Academic Editor: Hahmid Reza Zargar

Copyright © 2012 Liang-Bin Xiong et al. This is an open access article distributed under the Creative Commons Attribution License, which permits unrestricted use, distribution, and reproduction in any medium, provided the original work is properly cited.

Titanium dioxide (TiO₂) is the most investigated crystalline oxide in the surface science of metal oxides. Its physical and chemical properties are dominantly determined by its surface condition. Ti³⁺ surface defect (TSD) is one of the most important surface defects in TiO₂. According to publications by other groups and the studies carried out in our laboratory, the formation mechanism of TSD is proposed. The generation, properties, and photocatalytic application of TSD are overviewed; the recent exploration of TSD is summarized, analyzed, and evaluated as well in this paper.

1. Introduction

Titanium dioxide (TiO₂) has been studied extensively in the field of surface science due to the wide range of its applications and the expectation for insights into surface properties on the fundamental level [1]. These studies have been motivated in part by the discovery that TiO₂ is a photocatalyst with relatively high efficiency for the decomposition of water [2–8] and the degradation of organic species [9–19]. The photocatalytic activity of TiO₂ is often dependent on the nature and density of surface defect sites. Liu et al. [20] have shown that the dominant defects in TiO₂ surfaces are Ti³⁺ defects and oxygen vacancies. Much work has been focused on the TSD and the possible effect of the TSD in TiO₂. It has been shown that the chemistry of stoichiometric TiO₂ surfaces differs markedly from surfaces containing Ti³⁺. Ti³⁺ is considered to be an important reactive agent for many adsorbates; hence many surface reactions are influenced by these point defects [21]. Sirisuk et al. [22] reported that Ti³⁺ sites play an essential role in photocatalytic process over TiO₂ photocatalyst. Sakai and coworkers [23–25] reported that TSD in anatase is an important parameter controlling the hydrophilic property. Also, as a support with high-surface area of anatase, TSD

plays a significant role in enhancing the dispersion and stability of supported metal such as gold cluster and cobalt via the strong interaction between defect site and metal cluster [26]. Furthermore, for practical applications, pristine TiO₂ is not a good candidate, because it is only active under ultraviolet (UV) irradiation in order to overcome the band gap of above 3.0 eV. Reduced TiO₂ (TiO_{2-x}), which contains the Ti³⁺, however, has been demonstrated to exhibit visible light absorption [27–31]. It is therefore highly important to have a comprehensive understanding of the methods and the techniques of Ti³⁺ generation and monitoring as well as Ti³⁺ property exploration.

TSD is not hard to be produced because its generation does not need harsh preparation conditions. The reported methods to produce TiO₂ containing TSD include UV irradiation [29, 32, 33], heating TiO₂ under vacuum [34, 35], thermal annealing to high temperatures (above 500 K) [36], reducing conditions (C [37], H₂ [20]), plasma-treating [38], laser [39], and high-energy particle (neutron [40–42], Ar⁺ [43], electron [44], or γ -ray [45],) bombardment. Averaging spectroscopic techniques like X-ray photoelectron spectroscopy (XPS) [46–48], electron spin (or paramagnetic) resonance (ESR or EPR) [49–59], and temperature-programmed desorption (TPD) [22, 60] have given valuable

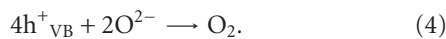
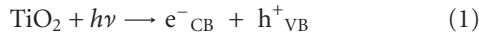
information for monitoring Ti^{3+} defects in TiO_2 surfaces. In addition, TiO_2 with TPD shows not only the properties of acidic oxide but also reducing characteristics. Besides photocatalysis, it can also be applied to gas absorption [61, 62], photochromism [30, 31], biology [63], and energy storage [28, 64].

Since Ti^{3+} strongly influences the surface chemistry of TiO_2 , a detailed picture of TSD may help to understand reactivity and overall material performance in photocatalytic applications. Up to now, the knowledge of TiO_2 has been reviewed extensively, but that of TiO_2 containing TSD has not yet been mentioned until now. According to the publications by other groups and studies carried out in our laboratory, we will present a general overview of the subject on the generation, properties, and photocatalytic application of Ti^{3+} in the surface of TiO_2 .

2. Generation of Ti^{3+} Surface Defects

2.1. Formation Mechanism of Ti^{3+} Surface Defects. TSD can be generated by reduction of Ti^{4+} ions. There are two typical processes for Ti^{4+} reduction to Ti^{3+} .

One is that a Ti^{4+} ion receives a photoelectron, which is usually generated due to UV irradiation on TiO_2 . As shown in Figure 1 [33], photogenerated electrons and holes are produced in TiO_2 under UV irradiation. The electrons can be trapped and tend to reduce Ti^{4+} cations to Ti^{3+} state, and the holes oxidize O^{2-} anions for the formation of O^- trapped hole or even oxygen gas [65]. The charge transfer steps are as follows:



Another process for Ti^{4+} reduction to Ti^{3+} is usually accompanied by a loss of oxygen from the surface of TiO_2 . TSD can be introduced deliberately by annealing in vacuum condition, thermal treatment under reducing atmosphere (H_2 , CO), or by bombardment using electron beam, neutron, or γ -ray. In these processes, Ti^{4+} ions receive electrons from these reducing gases or lattice oxygens which are usually removed from stoichiometric TiO_2 . Figure 2 [20] shows the EPR intensity of Ti^{3+} and oxygen vacancies versus H_2 treatment temperature during the H_2 treatment. Liu et al. [20] proposed that the interaction between H_2 and TiO_2 fell into three types. Firstly, hydrogen interacted physically with the adsorbed oxygen on the surface of TiO_2 at a temperature below $300^\circ C$. Secondly, when the temperature was higher than $300^\circ C$, electrons were transferred from the H atoms to the O atoms in the lattice of TiO_2 . Then, the oxygen vacancies were formed when the O atom left with the H atom in the form of H_2O . Thirdly, when the temperature was up to

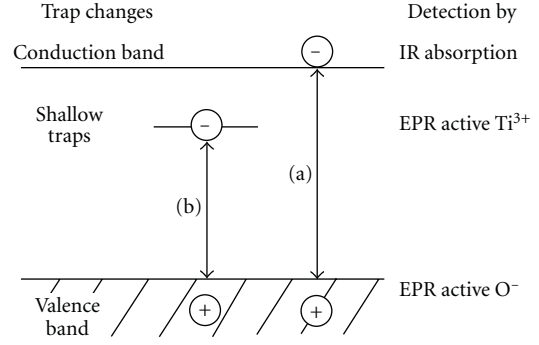


FIGURE 1: Scheme of UV induced charge separation in TiO_2 [33].

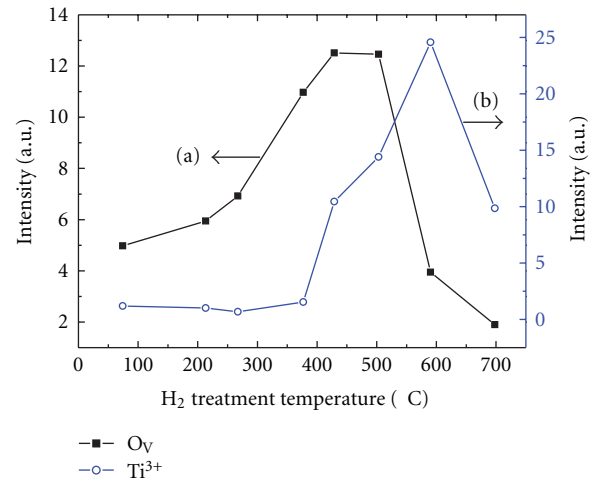


FIGURE 2: EPR intensity of Ti^{3+} and oxygen vacancies versus H_2 treatment temperature during the H_2 treatment [20].

$450^\circ C$, the interaction between H_2 and TiO_2 proceeded more drastically, in which the electrons transferred from oxygen vacancies to Ti^{4+} ions, and then Ti^{3+} ions were formed. In this case, the higher the temperature is, the more Ti^{3+} ions were produced. Furthermore, when the temperature increased to $560^\circ C$, more energy was supplied, and the electrons already in the oxygen vacancies were driven away and transferred to Ti^{4+} . This result is in accordance with the EPR data which indicated the intensity of oxygen vacancies decreased and that of Ti^{3+} increased.

Chen et al. [66] reported that some Ti^{4+} ions in the surface of TiO_2 were reduced into Ti^{3+} state by carbon formed from pyrolysis of titanyl organic compounds. The mechanism for this reduction reaction is that the carbon from organic component carbonizing could reduce Ti^{4+} to Ti^{3+} at high temperature, which is similar to Liu's report. However, Chen et al. may hold a wrong idea that TSD is the same as oxygen vacancies. According to the publications by Berger et al. [33] and Liu et al. [20], the TSD is quite different from the oxygen vacancies because both TSD and oxygen vacancies can be generated, respectively. Here, we can see that the principal character of the second reduction process different from the first one is that Ti^{4+} ions are not reduced

by photoelectrons generated by UV irradiation, but reduced by electron donors such as H_2 , C, or lattice oxygen in TiO_2 .

2.2. Generation Methods for Ti^{3+} Surface Defects

2.2.1. UV Irradiation. Figure 1 is a scheme for the generation of TSD in anatase TiO_2 powder at 140 K and below by UV irradiation. As discussed in Section 2.1, photogenerated electrons and holes are produced by UV radiation in TiO_2 , and the electrons can be trapped and tend to reduce Ti^{4+} cations to Ti^{3+} state. However, it has been shown that only a limited fraction of electrons are actually localized as in Ti^{3+} state, while the major fraction remains in the conduction band after UV excitation [36]. After discontinuation of UV exposure, the electrons trapped in Ti^{3+} can be stored for hours when TiO_2 particles are electronically isolated and kept at low temperatures. A high quantum yield and much longer life of the Ti^{3+} ions can be achieved in wet TiO_2 gels. Kuznetsov et al. [67] reported that the quantum yield of Ti^{3+} as high as 22–25% has been independently obtained from the absorption delay and extinction measurements. These Ti^{3+} centers can be produced by the wet TiO_2 gels under the UV irradiation in the spectral range between 3.25 and 4.4 eV. All photo-induced Ti^{3+} centers are chemically active and long lived. Under a prolonged UV-laser irradiation, their lifetime can be extremely long and exceeds months at room temperature in the absence of oxygen [28]. The electrons are stored in the gel network as small polarons, Ti^{3+} centers, whereas the holes are stored in the liquid phase as H^+ ions or radicals. Some other research groups also reported the generation of Ti^{3+} defects by UV irradiation [68, 69].

2.2.2. Annealing or Calcination. Vacuum annealing and calcination are widely used to generate TSD [34–36, 63, 70–72]. Guillemot et al. [63] reported that low-temperature vacuum annealing could create a controlled number of TSD ranging from low concentration (<3% Ti^{3+}/Ti^{4+}) to high concentration (around 21% Ti^{3+}/Ti^{4+}) at 323 and 573 K, respectively. Figure 3 shows the variation of the Ti^{3+} to Ti^{4+} ratio with vacuum annealing temperature. Nevertheless, TSD stability has been ascertained by first UHV annealed at 523 K and stored under different conditions. In fact, in relation to storage conditions, one night under UHV or one week under a laboratory atmosphere, the initial Ti^{3+}/Ti^{4+} only decreased from 9.1% to 8.7 or 3.4%, respectively.

Xu and coworkers [70] prepared TiO_2 ultrafine particles by the colloid chemical method. They found that as the calcining temperature decreased, the size of TiO_2 ultrafine particles decreased, and the contents of TSD and the number of hydroxyl active species increased, which were considered to be essential to the photocatalytic activity of the samples. Huizinga and Prins [71] reported that the reduction of Pt/ TiO_2 at 573 K led to the formation of a Ti^{3+} ESR signal. After reduction at 573 K, 0.3% of the total number of Ti^{4+} ions in TiO_2 was reduced to Ti^{3+} . They found that the reduction of the TiO_2 by hydrogen was catalyzed by the

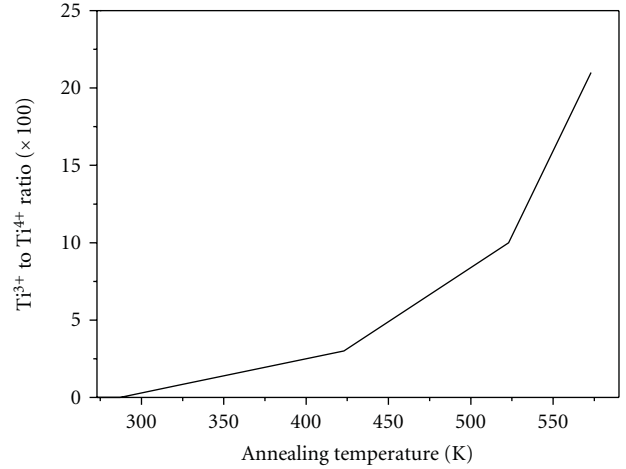
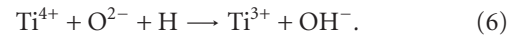
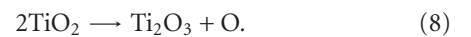


FIGURE 3: Variation of the Ti^{3+} to Ti^{4+} ratio with vacuum annealing temperature [63].

platinum. The reduction mechanism has been proposed as follows:



2.2.3. Particles (Electron, Neutron, and γ -Ray) Bombardment. Zhang et al. [47] prepared TiO_2/Si films on silicon substrates by the DC reactive sputtering method. The TiO_2/Si structures with different TiO_2 film thickness were irradiated by electron beams. It is found that the number of Ti^{3+} ions increased and Ti^{4+} ions decreased after the irradiation. The relative abundance can be calculated. The number of Ti^{3+} increased to 10% and that of Ti^{4+} decreased from 98% to 90%. This implies that in the transition layer, a fraction of Ti^{4+} ions turned to Ti^{3+} ions and the chemical composition changed as follows:



Jun et al. [44] reported the improvement of the photoactivity of TiO_2 which underwent electron beam (EB) treatment (1 MeV) as a function of the absorbed radiation dose (MGy). The radiation-induced effects on the TiO_2 crystal structure, for example, change of the Ti^{3+}/Ti^{4+} ratio, were investigated. As shown in Figure 4, the quantitative analyses of Ti^{4+} and Ti^{3+} surface states in EB-treated TiO_2 at different radiation doses are presented by XPS data. It shows that a maximum decrease of Ti^{4+} amount treated at higher EB doses and approximately the same amount of Ti^{3+} on the surface state in $Ti2p$ up to about 3 MGy is observed. Both $Ti2p_{1/2}$ and $Ti2p_{3/2}$ states showed a change in Ti^{3+} and Ti^{4+} , and the Ti^{3+} states increased by about 15% as a consequence of EB treatment. The Ti^{3+} state on TiO_2 surface is important because it can play a similar role as observed

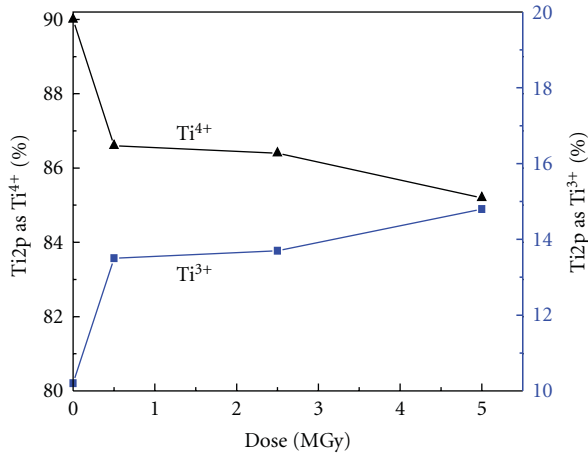


FIGURE 4: Surface of Ti as Ti^{3+} and Ti^{4+} of unirradiated and EB-treated TiO_2 samples as a function of absorbed radiation doses [44].

in TiO_2 doped with metal atoms, which can trap the photo-generated electrons and thereafter leave behind unpaired charges to promote photoactivity.

Figure 5(a) [45] shows the ESR signals of O^- anion radicals and Ti^{3+} cations on TiO_2 powder after γ -ray irradiation of 150 MR under N_2 atmosphere. Before γ -ray irradiation, no signal could be observed in the ESR signals, while after γ -ray irradiation, the ESR signals attributed to the O^- anion radicals and associated Ti^{3+} were observed. It increased with the increase of the γ -ray irradiation dosage shown in Figure 5(b) [45].

Huang et al. [30] reported that upon exposure to γ -radiation, a concentrated TiO_2 sol changed from colorless to deep blue with an absorption maximum at 540 nm. The absorption has been assigned to trapped electrons or Ti^{3+} ions in the solid matrix based on its spectroscopic similarity to the samples irradiated with UV light. The origin of the trapped electrons during γ -ray irradiation may be traced to a series of reducing species produced by the high-energy electrons, which in turn are the direct result of γ -ray irradiation. The absorption intensity is linearly related to the duration of exposure to γ -ray irradiation.

The reduction effect (from Ti^{4+} to Ti^{3+}) in rutile induced by neutron irradiation is also reported. Lu et al. [72] found that Ti^{4+} ions reduced to Ti^{3+} , Ti^{2+} , and even Ti^+ after the neutron irradiation by means of characteristic techniques of UV-VIS-IR, XPS, XRD, and AFM.

TiO_2 irradiated by UV light can create TSD with ease. However, a special gel structure, which has a poor chemical stability, is definitely needed for a high quantum yield of TSD. Thus, this method is subjected to the certain restriction in the practical photocatalytic application. Annealing and calcination can effectively control concentration of TSD and morphology of TiO_2 . Thus, both of them are extensively studied and used although they are still tedious, for example, high temperature, high vacuum, and atmosphere frequently needed. The bombardment method is atypical, but important.

3. Properties of Ti^{3+} Surface Defects

3.1. Structural Properties of Ti^{3+} Surface Defects. Lu et al. [72] described the structure of ideal rutile single crystal and rutile with insufficient oxygen. In the ideal rutile single crystal, each titanium ion is located in the center of oxygen octahedron. The symmetry of the oxygen octahedron is rhombic symmetry (D_{2h}). The parallel (R_{\parallel}°) and vertical (R_{\perp}°) Ti^{4+} - O^{2-} bonding lengths are 1.988 and 1.944 Å (see Figure 6), and the bonding angle in the vertical plane is about 80.83° . When a host Ti^{4+} ion is changed to Ti^{3+} ion, the local electrostatic balance is broken, and an O_V (oxygen vacancy) should be introduced because of charge compensation. In order to determine the position of the O_V as well as the local structure of the $[\text{Ti}^{3+}\text{-O}_V]$ center in the reduced rutile crystal, the structure model is established, and the optical spectra is calculated by using the crystal field theory. In this structure model, the axial O_V is located on the nearest position of central Ti^{3+} ion. When an O_V appears on the nearest position of central Ti^{3+} ion along the R_{\parallel}° direction of the oxygen octahedron, the local symmetry would change from D_{2h} to C_{2v} . Since the effective charge of the O_V is positive, the central Ti^{3+} is expected to shift away from the O_V along the R_{\parallel}° direction by an amount ΔR_c due to the electrostatic repulsion. Similarly, the four O^{2-} ions on the vertical plane would also move towards the O_V by an amount ΔR_p due to the electrostatic attraction (see Figure 6). Considering the much larger distance between the O_V and the remaining O^{2-} ion of the R_{\parallel}° direction, the displacement of the only axial O^{2-} ion may be much smaller than ΔR_c or ΔR_p and can be omitted for simplicity.

This model is in accordance with those proposed by Weyl and Forland [73] and Breckenridge and Hosler [74]. In their models, Ti^{3+} ions are also on sites adjacent to the oxygen vacancy. In addition, Weyl and coworkers have drawn a schematic picture of the structure of Ti^{3+} ions (Figure 7). Figure 7 [73] shows schematically what happens when a crystal of Ti^{4+}O_2 loses one oxygen atom, and the two electrons of the O^{2-} ion change two Ti^{4+} to Ti^{3+} ions. These Ti^{3+} ions are strongly polarized and a state is assumed, in which its extreme can be described as two Ti^{4+} ions and two additional electrons. The latter may assume the position of the missing O^{2-} ion. The intensive light absorption in such partly reduced crystals is the result of the strong distortion of the outer orbitals of the Ti^{3+} ions. Ti^{3+} ions in this state absorb light more intensively than undeformed Ti^{3+} ions.

3.2. Optical Properties of Ti^{3+} Surface Defects. Optical properties of TSD lie in two aspects. One is that Ti^{3+} ions are the origin of the blue coloration or coloration center [27, 58, 64, 74] and the other is that Ti^{3+} species has a characteristic visible absorption spectrum [27–31, 75–78]. Ookubo et al. [58] developed a method that examined the quantitative relation between degree of blue coloration and the concentration of the Ti^{3+} ions. The method has been proposed based on the phenomenon that a Ti^{3+} salt was hydrolyzed slowly with the presence of urea in an aqueous solution. With this method, a blue TiO_2 was obtained,

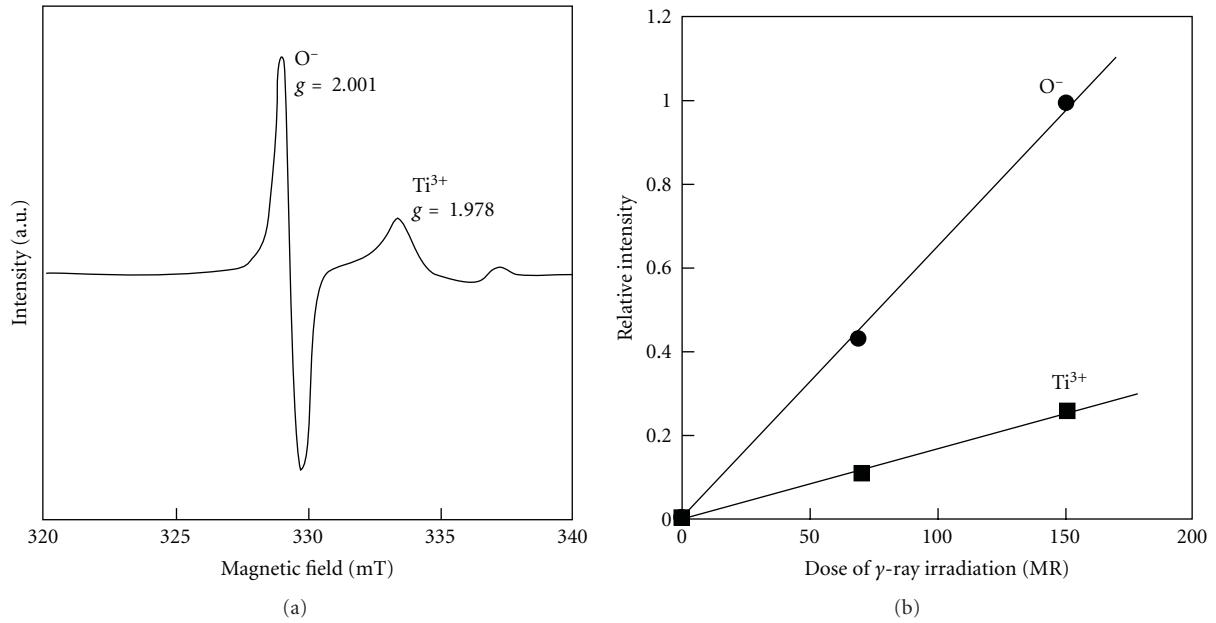


FIGURE 5: (a) ESR signals of O^- anion radicals and Ti^{3+} cations on the TiO_2 powder after γ -ray irradiation of 150 MR under N_2 atmosphere. (b) Variation of the intensity of the signals due to γ -ray induced O^- anion radicals and Ti^{3+} cations with γ -ray irradiation time under N_2 atmosphere [45].

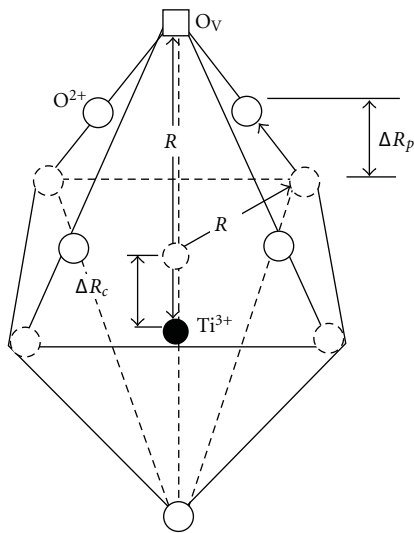


FIGURE 6: The schematic diagram model, that is, the central Ti^{3+} ion associated with an oxygen vacancy on its nearest position along the parallel direction [72].

and the degree of the coloration has been controlled by changing the period of refluxing the solution in the synthetic procedure. In addition, numerous studies have verified that the Ti^{3+} species induced oxygen vacancy states between the valence and the conduction bands, which would contribute to the visible response. Xiong et al. [64] identified the conversion of Ti^{4+} to Ti^{3+} in the TiO_2/Cu_2O bilayer film after the visible-light irradiation by the UV-vis diffuse reflectance measurement. Because Ti^{4+} has no response to visible light while Ti^{3+} does, the presence of Ti^{3+} ions leads to a weaker

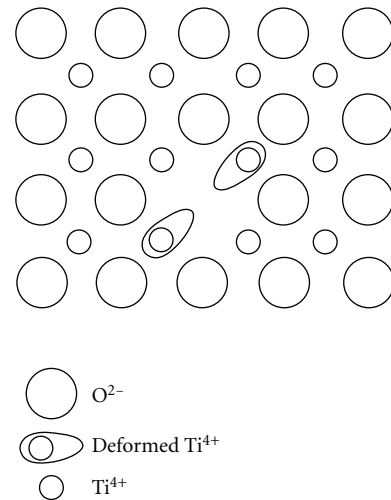


FIGURE 7: Schematic picture of a flaw on partly reduced TiO_2 [73].

absorbance of the bilayer film in the short wavelength range while stronger in the long wavelength range. It was also found that the transparent TiO_2 film turned blue under the irradiation (Figure 8(a)).

Bityurin et al. [29] proposed several models fitting the experimental data on the kinetics of UV laser-induced darkening in TiO_2 gels. Samples were exposed to various average laser intensities in the range of $0.05 \sim 0.5 \text{ W/cm}^2$ by using beam attenuators. After irradiation of a sample by a laser beam, the modified area looked like a dark spot on the transparent material surface (Figure 8(b)). The dark color spot was believed to be caused by the transformation of Ti^{4+} to Ti^{3+} . TiO_2 sol was also shown to change from

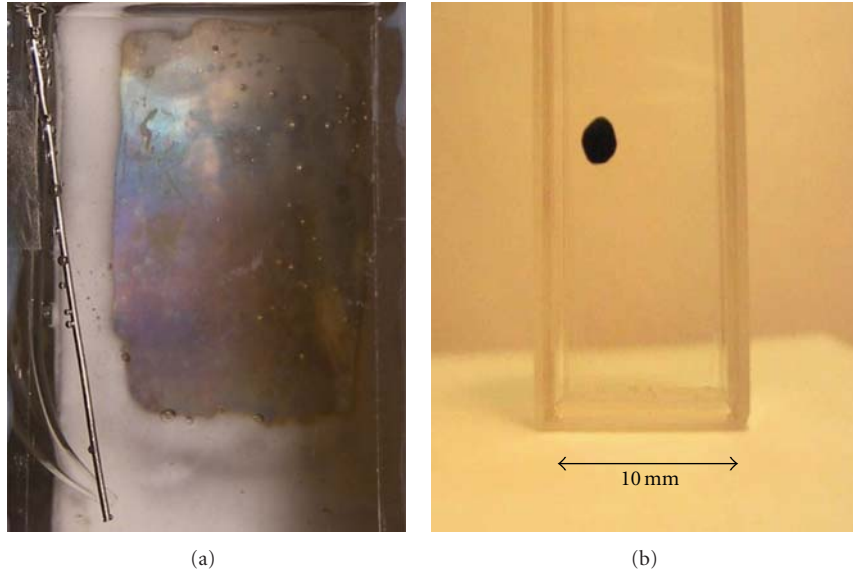


FIGURE 8: Light-induced color change in (a) $\text{TiO}_2/\text{Cu}_2\text{O}$ bilayer film [64] and (b) titanium-oxide gel [29].

colorless to deep blue with an absorption maximum at 540 nm upon exposure to γ -radiation [29]. The absorption has been assigned to trapped electrons or Ti^{3+} ions in the solid matrix based on its spectroscopic similarity to the samples irradiated with UV light.

3.3. XPS Properties of Ti^{3+} Surface Defects. According to the standard binding energy of $\text{Ti}2p_{3/2}$ in TiO_2 , that for Ti^{3+} is usually located at 457.7 eV and that for Ti^{4+} is at 459.5 eV. The O (1s) binding energy for TiO_2 is 529.3 eV [79]. Generally speaking, the binding energy peak of $\text{Ti}2p$ in stoichiometry TiO_2 is not broad and no shoulder peak. However, that for TiO_2 containing Ti^{3+} in the surface is usually tortured and turns into much broader. In this case, a fitting skill such as Gaussian of the Gauss-Lorentzian fitting can be taken to obtain the information of Ti^{3+} and Ti^{4+} in the surface of reduced TiO_2 . The relative contents of Ti^{3+} in the surface of reduced TiO_2 can also be obtained according to the XPS peak areas.

Greenlief et al. [46] reported the $\text{Ti}2p$ binding energy data of TiO_2 thin films with different monolayers on polycrystalline Pt after vacuum annealing by XPS technique. The measured binding energy 458.9 eV was the $\text{Ti}2p_{3/2}$ peak for the TiO_2 thin films with coverages more than 3 monolayers (1 monolayer is assumed to be an evenly dispersed film 2.6 Å thick). The O (1s) binding energy for these TiO_2 thin films were 530.3 eV. The O/Ti ratio (as determined by XPS peak areas) was stoichiometric (2.0) for these TiO_2 thin films. After vacuum annealing, the ratio dropped to between 1.0 and 1.5, and a mixture of Ti^{3+} and Ti^{4+} was obtained. The binding energy 458.9 eV was observed and attributed to Ti^{3+} state.

Recently, our group [64] found that the TSD can be generated in $\text{TiO}_2/\text{Cu}_2\text{O}$ bilayer film under visible-light irradiation. By means of XPS (Figure 9), it can be seen that the binding energy of $\text{Ti}2p_{3/2}$ in bilayer film without

the irradiation was 458.7 eV (Figure 9(a)). It is difficult to simulate this peak since the peak was not so broad, and there was no shoulder peak. The binding energy of $\text{Ti}2p_{3/2}$ in the bilayer film after the irradiation was 458.1 eV. Compared with the peak for $\text{Ti}2p_{3/2}$ in the same bilayer film without the irradiation, the one after the irradiation was much broader and there was 0.6 eV shift. This $\text{Ti}2p_{3/2}$ spectrum can be simulated with Gaussian simulation. The peaks at 457.8 eV and at 459.2 eV were attributed to Ti^{3+} and Ti^{4+} , respectively (Figure 9(b)). The result is in accordance with the reported data [79]. The content of Ti^{3+} ions was as high as 74% in $\text{TiO}_2/\text{Cu}_2\text{O}$ bilayer film after visible-light irradiation according to the comparison of the peaks area.

3.4. EPR Properties of Ti^{3+} Surface Defects. EPR is a highly sensitive technique which allows investigation of paramagnetic species having one or more unpaired electrons either in the bulk or at the surface of various solids. EPR technique is already widely used by many researchers to characterize TSD. The data of EPR signals assigned to Ti^{3+} in some published paper are shown in Table 1.

Tijana et al. also presented some published data of EPR signals of Ti^{3+} in the book edited by Kokorin and Bahnmann [90]. They proposed that Ti^{3+} in the surface and that in the bulk of TiO_2 can be distinguished by the differences of their EPR parameters. The values of the g -factors for surface Ti^{3+} particles are significantly lower than those usually found in bulk TiO_2 . Similar result was also reported by Nakaoka and Nosaka [91]. There is a small change in the g -values of the axially symmetrical g -tensor (previously identified as interstitial interior Ti^{3+} ions) upon the sample heating ($g_{||} = 1.957$, $g_{\perp} = 1.990$ for untreated sample and $g_{||} = 1.961$, $g_{\perp} = 1.992$ for sample heated at 700°C for 5 h). They attributed the first signal to the photo-generated electron trapped on the surface Ti^{3+} ions, and the second one to the inner Ti^{3+} ions.

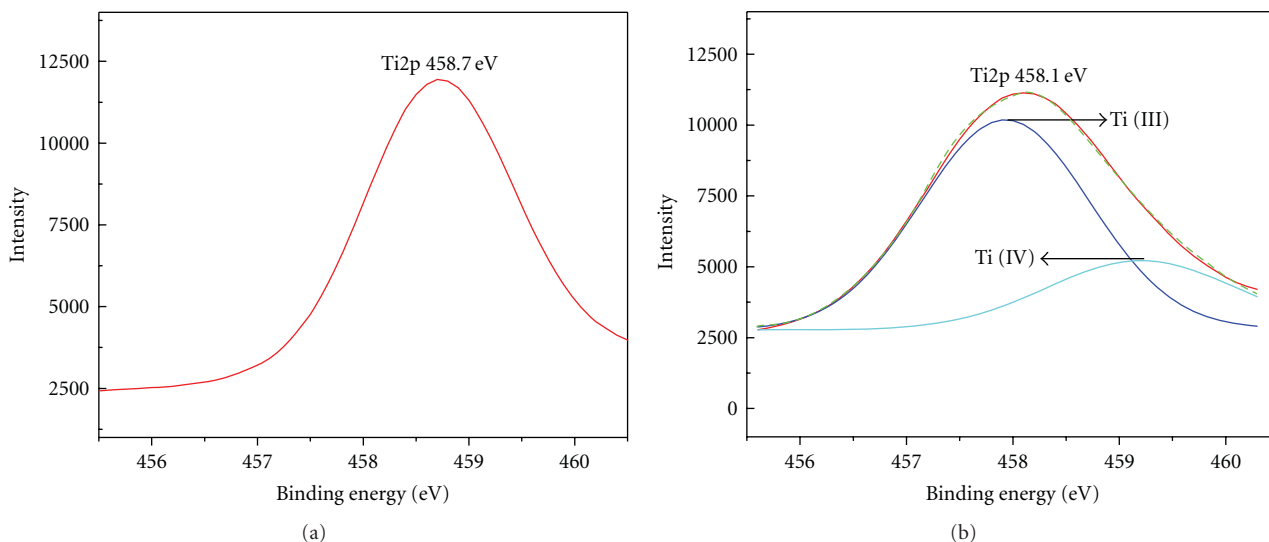


FIGURE 9: XPS of Ti2p of TiO₂/Cu₂O bilayer film before (a) and after irradiation (b). XPS of Ti2p is simulated by Gaussian equation [64].

In addition, Tijana et al. found the difference of EPR signal shapes for surface and inner Ti³⁺ ions. According to the characters of EPR signals, they proposed two general types of traps (Ti³⁺ ions): internal, having a narrow axially symmetric EPR signal, and surface, with broad EPR lines. Magnetic resonance parameters of the internal, interstitial (inner) Ti³⁺ ions slightly vary due to the different delocalization of the unpaired electron density and symmetry of the local surroundings (presence of vacancies and impurities in the nearest coordination sphere). It also happens for the surface electron trap. In this case, *g*-values and the linewidth of the surface Ti³⁺ ions mainly depend upon surface modification.

3.5. Temperature Program Reduction (TPD). Temperature-programmed desorption using carbon dioxide (CO₂-TPD) as a probe can be employed to monitor surface defects in TiO₂ [22, 60, 84, 92]. CO₂-TPD analysis indicates a signal of CO₂, which desorbs from the TiO₂ surface between the ranges of 123 and 253 K and results in two peaks: one peak at about 170 K attributed to CO₂ molecules bound to a regular five-coordinate Ti⁴⁺ site which was a perfect TiO₂ structure, and another peak at about 200 K corresponding to CO₂ molecules bound to Ti³⁺ which was a defected TiO₂ structure [60, 84] (Figure 10). The positions of the peaks are shifted slightly from those reported by Sirisuk and coworkers [22]. Thompson et al. [60] have observed the characteristic two-step desorption process which is indicative of the presence of both Ti³⁺ defects and nondefective TiO₂ sites. Moreover, they have measured the activation energy for both of the desorption peaks of CO₂. For CO₂ desorption from the fully oxidized (or perfected) surface, where the CO₂ is bound to Ti⁴⁺ sites, a zero-coverage activation energy for CO₂ desorption of 48.5 kJ/mol is measured. It is in approximate agreement with theoretical calculations value of 65 kJ/mol [93]. For CO₂ desorption from the Ti³⁺ sites produced by annealing TiO₂ (110) in vacuum, a zero-coverage activation energy of ~54 kJ/mol was measured. This indicates that Ti³⁺

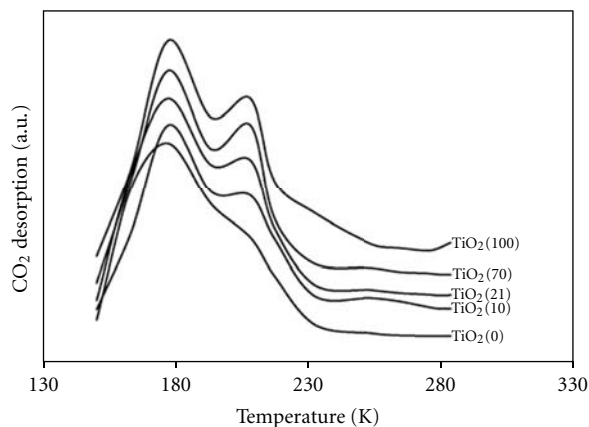


FIGURE 10: Thermal desorption spectra for CO₂ adsorbed on TiO₂ calcinations [84].

sites bind CO₂ slightly more strongly (TPD peak at 200 K) than the fivefold coordinated Ti⁴⁺ sites (TPD peak at 170 K) do.

4. Photocatalytic Application

4.1. Photocatalytic Reaction Mechanism of Ti³⁺ Surface Defects. The photocatalytic reaction mechanisms are widely studied. The principle of TiO₂ photocatalytic reaction is straightforward. Upon absorption of photons with energy larger than the band gap of semiconductor materials, electrons are excited from the valence band to the conduction band, producing electron-hole pairs. These charge carriers migrate to the surface and react with the chemicals adsorbed on the surface to decompose these chemicals. This photodecomposition process usually involves one or more of radicals or intermediate species such as •OH, O²⁻, H₂O₂, or O₂, which play important roles in the photocatalytic reaction. The photocatalytic activity of a semiconductor is largely

TABLE 1: The data of EPR signals assigned to Ti^{3+} in some published paper.

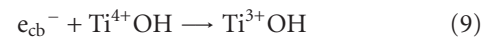
ESR parameters (g-value)		Condition	Ref.
$g_{ }$	g_{\perp}		
1.9495	1.9640	Anatase nanoparticles exposure to UV light	[33]
1.9600	1.990	Anatase nanoparticles exposure to UV light	[33]
1.902	1.953	Laser-irradiated TiO_2	[39]
1.962	1.960	Titanium silicalite	[49]
1.905	1.912	Ti- SiO_2 by a sol-gel method	[49]
1.88	1.925	Fe^{3+} -doped colloids: 6 g dm^{-3} TiO_2 , 0.5 wt% Fe, irradiated 6 h	[54]
1.988	1.897	Fe^{3+} -doped colloids: 5 g dm^{-3} TiO_2 , 0.1 wt% Fe, irradiated 3 h	[54]
1.975	1.944	Self-doped TiO_2	[78]
1.996	1.901	$KTa_{0.9}Nb_{0.1}O_3$	[80]
1.994	1.896	Hydrated TiO_2	[81]
1.9482	1.9707	Carbon-doped TiO_2	[82]
1.975	1.963	Ultrafine-powdered TiO_2	[83]
	1.996	TiO_2 powder was heated in hydrogen (H_2) gas	[20]
	1.990, 1.990, 1.960	Hydrated anatase	[32]
	1.970, 1.965	The untreated fresh and used TiO_2 catalysts	[51]
	1.93	TiO_2 exposure to flowing H_2 at 573 K for 4 h	[53]
	1.908, 1.981	Pt/ TiO_2 reduced at 623 K	[56]
	1.975	sol-gel processing of $Ti(i-OPr)_4$ (i-OPr isopropoxy group)	[69]
	1.92	Anatase reduction at 573 K	[75]
	1.9605, 2.0059	Nitrogen-doped TiO_2	[76]
	1.996	TiO_2 calcined at 21% O_2	[84]
	1.98	TiO_2 nanotubes	[85]
	1.996	TiO_2 obtained under vacuum	[86]
	1.964	Silver/ TiO_2 (1.026 wt.% loading)	[87]
	1.9880 ± 0.0005	Carbon-Doped TiO_2	[88]
	1.996	Nanocrystalline TiO_2 via solvothermal synthesis	[89]

controlled by (i) the light absorption properties, for example, light absorption spectrum and coefficient, (ii) reduction and oxidation rates on the surface by the electron and hole, (iii) and the electron-hole recombination rate [92].

As for TiO_2 containing TSD, its photocatalytic activity is definitely dominated by TSD. TSD improves the photocatalytic activity of pure TiO_2 from the following two aspects: (i) it extends the photoresponse of TiO_2 from UV to visible light region, which leads to visible-light photocatalytic activity; (ii) it provides important reactive agents for many adsorbates and results in the reduction of an electrohole pair recombination rate [44].

Park et al. [83] proposed the mechanism of TSD participating in photocatalytic reaction. When the TiO_2 photocatalysts were irradiated, e^-/h^+ pairs were formed. In

the absence of the electron and hole scavengers, most of them recombined with each other within a few nanoseconds. If the scavengers or surface defects were present to trap the electron or hole, e^-/h^+ recombinations could be prevented, and the subsequent reactions caused by the electrons and holes were dramatically enhanced. In this case, electrons donors reacted with holes. The electron can be trapped by Ti^{4+} to generate an isolated Ti^{3+} ion. In the presence of O_2 , the Ti^{3+} sites easily react with O_2 , leading to the formation of radicals such as $\bullet O_2^-$, $HO_2\bullet$, and $\bullet OH$. The charge transfer processes may be as follows:



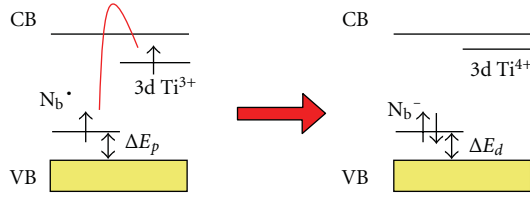
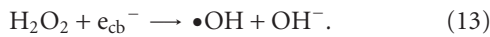
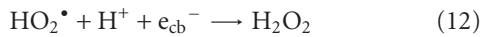
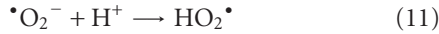


FIGURE 11: Electronic band structure modifications resulting from the interactions between N_b^\bullet (N_s^\bullet or N_i^\bullet) and Ti^{3+} defects [96].



4.2. Photocatalytic Application of Ti^{3+} Surface Defects

4.2.1. Ion-Doped TiO_2 Photocatalyst. A great deal of research has been focused on ion-doped TiO_2 with both transition metal and nonmetal impurities in order to lower the threshold energy and improve photocatalytic activity. Doping with transition metals has shown both positive and negative effects. Indeed, these metal-doped photocatalysts have been demonstrated to suffer from thermal instability, and metal centers acting as electron traps have reduced the photocatalytic efficiency [94].

Stimulated by the report of Asahi et al. in 2001 [95], there has been an explosion of interest in TiO_2 doping with nonmetal ions, N, C, S, B, especially with nitrogen. Livraghi et al. [96] reported the origin of photocatalytic activity of N-doped TiO_2 under visible light. As shown in Figure 11, the material contains single-atom nitrogen impurities that form either diamagnetic (N_b^-) or paramagnetic (N_b^\bullet) centers. Both types of N_b centers give rise to localized states in the band gap of the oxide. The relative abundance of these species depends on the oxidation state of the solid since upon reduction, electron transfer from Ti^{3+} ions to N_b results in the formation of Ti^{4+} and N_b^- . The presence of Ti^{3+} ions is helpful to form the N paramagnetic centers at the expense of the Ti^{3+} ions oxidized to Ti^{4+} . The photocatalytic activity of the N-doped TiO_2 catalyst was thought to be the synergistic effect of nitrogen and Ti^{3+} species [76, 97].

Sun et al. [76] reported that the N-doped TiO_2 catalyst showed higher photocatalytic activity for degradation of 4-CP than pure TiO_2 under not only visible but also UV irradiation due to the presence of Ti^{3+} . Qin et al. [98] demonstrated that the enhancement of methyl orange and 2-mercaptobenzothiazole photodegradation using the N-doped TiO_2 catalysts is mainly involved in the efficient separation of electron-hole pairs owing to the presence of Ti^{3+} and the improvement of the organic substrate adsorption in catalysts suspension and optical response in visible-light region. However, it is found that excessive Ti^{3+} acted as a recombination center for holes and electrons, which is the reason for an optimal content of Ti^{3+} in

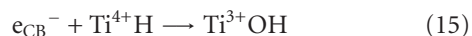
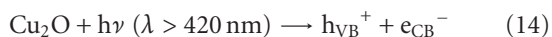
the nitrogen-doped TiO_2 . The N-doped TiO_2 with N/Ti proportioning of 20 mol% calcined at $400^\circ C$ exhibited the highest visible-light activity. Therefore, the presence and optimal content of Ti^{3+} might be the critical factors for the improvement of the photoactivity.

Carbon-doped TiO_2 has also shown much better photocatalytic activity due to the presence of TSD [37, 66, 82, 88, 92]. Chen et al. [66] reported that the C from pyrolyzing process of titanyl organic compounds could reduce the part of Ti^{4+} in the surface of TiO_2 into Ti^{3+} , and some OH groups were formed on crystal surface with the presence of water from pyrolysis. This allowed TiO_2 to possess abundant TSD, which acted as the active center for both photocatalytic reaction and matching OH at its surface. When Ti^{3+}/OH ratio in the surface of nanometer crystalline TiO_2 approaches 1, there is more effective photocatalytic activity. Li et al. [82] reported that the carbon-doped TiO_2 with high surface area and good crystallinity showed an obvious enlarged range of absorption up to 700 nm and had much better photocatalytic activity for gas phase photo-oxidation of benzene under artificial solar light than pure TiO_2 . The visible-light photocatalytic activity is ascribed to the presence of oxygen vacancy state because of the formation of Ti^{3+} species between the valence and the conduction bands in the TiO_2 band structure, which results in the as-synthesized carbon-doped TiO_2 responsive to the visible light.

4.2.2. Self-Doped TiO_2 Photocatalyst. Here, self-doped TiO_2 photocatalyst can be interpreted as Ti^{3+} -doped TiO_2 , in which nothing but Ti and O ions exists. As discussed in Section 2.2, self-doped TiO_2 photocatalyst can be produced by UV irradiation, heating under vacuum, thermal annealing to high temperatures (above 500 K), reducing conditions (C , H_2), plasma treating, laser, and high-energy particle (neutron, Ar^+ , electron, or γ -ray) bombardment. Abundant presented data and numerous valuable conclusions indicate that TSD in self-doped TiO_2 photocatalysts is responsible for the enhancement of photocatalytic activity [20, 34–36, 38–40, 42–44, 70, 83, 89, 99–102].

In addition, our group reported the high photocatalytic degradation of methylene blue by TiO_2/Cu_2O composite film [79] and photocatalytic water splitting by TiO_2/Cu_2O bilayer film owing to the presence of Ti^{3+} [64]. For photocatalytic degradation reaction, electrons excited from TiO_2/Cu_2O composite film under visible light were transferred from the conduction band of Cu_2O to that of TiO_2 . The formed intermediate state of Ti^{3+} ion was observed by X-ray photoelectron spectroscopy (XPS) on the TiO_2/Cu_2O composite film. Additionally, the accumulated electrons in the conduction band of TiO_2 were transferred to oxygen on the TiO_2 surface for the formation of O^{2-} or O_2^{2-} , which combines with H^+ to form H_2O_2 . The evolved H_2O_2 with $FeSO_4$ and EDTA forms Fenton reagent to degrade methylene blue. With regard to photocatalytic water splitting process, the photogenerated electrons from the conduction band of Cu_2O were captured by Ti^{4+} ions in TiO_2 , and Ti^{4+} ions were further reduced to Ti^{3+} ions. The Ti^{3+} ions have a long lifetime and bear the photogenerated electrons as a form

of energy. The electrons trapped in Ti^{3+} ions as stored energy lead to evolve H_2 from H_2O . The electron transfer processes may be as follows:



5. Concluding Remarks

An overview on current literature on the subject of TSD in TiO_2 has been provided here, but the works that have been done and the progresses that have been achieved on this subject are far from being completely resolved. While some of these results reviewed here might be turned out to be of mere fundamental interest and irrelevant for the particular environment and applications, some might help to understand the behavior of this material. Since TiO_2 is used in so many different fields, TSD would attract more attention. It is expected that this paper will help to link the more fundamental and more applied lines of research on this subject.

Acknowledgments

This work was financially supported by the Project of Hubei Provincial Department of Education (XD201010406), the Doctor Foundation of Huanggang Normal University. Professor Y. Yu thanks the National Natural Science Foundation of China (no. 20973070), the National Basic Research Program of China (no. 2009CB939704), the Key Project of Ministry of Chinese Education (no. 109116), and self-determined research funds of CCNU from the colleges' basic research and operation of MOE for financial support.

References

- [1] U. Diebold, "The surface science of titanium dioxide," *Surface Science Reports*, vol. 48, no. 5–8, pp. 53–229, 2003.
- [2] A. Fujishima and K. Honda, "Electrochemical photolysis of water at a semiconductor electrode," *Nature*, vol. 238, no. 5358, pp. 37–38, 1972.
- [3] A. J. Nozik, "Photoelectrolysis of water using semiconducting TiO_2 crystals," *Nature*, vol. 257, no. 5525, pp. 383–386, 1975.
- [4] J. H. Carey and B. G. Oliver, "Intensity effects in the electrochemical photolysis of water at the TiO_2 electrode," *Nature*, vol. 259, no. 5544, pp. 554–556, 1976.
- [5] O. Khaselev and J. A. Turner, "A monolithic photovoltaic-photoelectrochemical device for hydrogen production via water splitting," *Science*, vol. 280, no. 5362, pp. 425–427, 1998.
- [6] Z. Zou, J. Ye, K. Sayama, and H. Arakawa, "Direct splitting of water under visible light irradiation with an oxide semiconductor photocatalyst," *Nature*, vol. 414, no. 6864, pp. 625–627, 2001.
- [7] S. U. M. Khan, M. Al-Shahry, and W. B. Ingler, "Efficient photochemical water splitting by a chemically modified n- TiO_2 ," *Science*, vol. 297, no. 5590, pp. 2243–2245, 2002.
- [8] J. Tang, J. R. Durrant, and D. R. Klug, "Mechanism of photocatalytic water splitting in TiO_2 . Reaction of water with photoholes, importance of charge carrier dynamics, and evidence for four-hole chemistry," *Journal of the American Chemical Society*, vol. 130, no. 42, pp. 13885–13891, 2008.
- [9] Y. F. Li, Z. P. Liu, L. Liu, and W. Gao, "Mechanism and activity of photocatalytic oxygen evolution on titania anatase in aqueous surroundings," *Journal of the American Chemical Society*, vol. 132, no. 37, pp. 13008–13015, 2010.
- [10] X. Chen, L. Liu, P. Y. Yu, and S. S. Mao, "Increasing solar absorption for photocatalysis with black hydrogenated titanium dioxide nanocrystals," *Science*, vol. 331, no. 6018, pp. 746–750, 2011.
- [11] N. Wu, J. Wang, D. N. Tafen et al., "Shape-enhanced photocatalytic activity of single-crystalline anatase TiO_2 (101) nanobelts," *Journal of the American Chemical Society*, vol. 132, no. 19, pp. 6679–6685, 2010.
- [12] K. Lee, D. Kim, P. Roy et al., "Anodic formation of thick anatase TiO_2 mesosponge layers for high-efficiency photocatalysis," *Journal of the American Chemical Society*, vol. 132, no. 5, pp. 1478–1479, 2010.
- [13] G. Liu, G. Y. Hua, X. Wang et al., "Visible light responsive nitrogen doped anatase TiO_2 sheets with dominant {001} facets derived from TiN," *Journal of the American Chemical Society*, vol. 131, no. 36, pp. 12868–12869, 2009.
- [14] A. Wold, "Photocatalytic properties of titanium dioxide (TiO_2)," *Chemistry Materials*, vol. 5, no. 3, pp. 280–283, 1993.
- [15] J. Fang, F. Wang, K. Qian, H. Bao, Z. Jiang, and W. Huang, "Bifunctional N-doped mesoporous TiO_2 photocatalysts," *The Journal of Physical Chemistry C*, vol. 112, no. 46, pp. 18150–18156, 2008.
- [16] M. Alvaro, C. Aprile, M. Benitez, E. Carbonell, and H. García, "Photocatalytic activity of structured mesoporous TiO_2 materials," *The Journal of Physical Chemistry B*, vol. 110, no. 13, pp. 6661–6665, 2006.
- [17] Y. Du and J. Rabani, "The measure of TiO_2 photocatalytic efficiency and the comparison of different photocatalytic titania," *The Journal of Physical Chemistry B*, vol. 107, no. 43, pp. 11970–11978, 2003.
- [18] S. Liu, J. Yu, and M. Jaroniec, "Tunable photocatalytic selectivity of hollow TiO_2 microspheres composed of anatase polyhedra with exposed {001} facets," *Journal of the American Chemical Society*, vol. 132, no. 34, pp. 11914–11916, 2010.
- [19] G. Li, N. M. Dimitrijevic, L. Chen, J. M. Nichols, T. Rajh, and K. A. Gray, "The important role of tetrahedral Ti^{4+} sites in the phase transformation and photocatalytic activity of TiO_2 nanocomposites," *Journal of the American Chemical Society*, vol. 130, no. 16, pp. 5402–5403, 2008.
- [20] H. Liu, H. T. Ma, X. Z. Li, W. Z. Li, M. Wu, and X. H. Bao, "The enhancement of TiO_2 photocatalytic activity by hydrogen thermal treatment," *Chemosphere*, vol. 50, no. 1, pp. 39–46, 2003.
- [21] G. B. Raupp and J. A. Dumesic, "Adsorption of CO , CO_2 , H_2 , and H_2O on titania surfaces with different oxidation states," *The Journal of Physical Chemistry*, vol. 89, no. 24, pp. 5240–5246, 1985.
- [22] A. Sirisuk, E. Klansorn, and P. Praserttham, "Effects of reaction medium and crystallite size on Ti^{3+} surface defects in titanium dioxide nanoparticles prepared by solvothermal method," *Catalysis Communications*, vol. 9, no. 9, pp. 1810–1814, 2008.
- [23] N. Sakai, R. Wang, A. Fujishima, T. Watanabe, and K. Hashimoto, "Effect of ultrasonic treatment on highly

- hydrophilic TiO₂ surfaces," *Langmuir*, vol. 14, no. 20, pp. 5918–5920, 1998.
- [24] N. Sakai, A. Fujishima, T. Watanabe, and K. Hashimoto, "Enhancement of the photoinduced hydrophilic conversion rate of TiO₂ film electrode surfaces by anodic polarization," *The Journal of Physical Chemistry B*, vol. 105, no. 15, pp. 3023–3026, 2001.
- [25] N. Sakai, A. Fujishima, T. Watanabe, and K. Hashimoto, "Quantitative evaluation of the photoinduced hydrophilic conversion properties of TiO₂ thin film surfaces by the reciprocal of contact angle," *The Journal of Physical Chemistry B*, vol. 107, no. 4, pp. 1028–1035, 2003.
- [26] W. T. Wallace, B. K. Min, and D. W. Goodman, "The stabilization of supported gold clusters by surface defects," *Journal of Molecular Catalysis A*, vol. 228, no. 1-2, pp. 3–10, 2005.
- [27] C. Kormann, D. W. Bahnemann, and M. R. Hoffmann, "Preparation and characterization of quantum-size titanium dioxide," *The Journal of Physical Chemistry*, vol. 92, no. 18, pp. 5196–5201, 1988.
- [28] A. I. Kuznetsov, O. Kameneva, A. Alexandrov et al., "Light-induced charge separation and storage in titanium oxide gels," *Physical Review E*, vol. 71, no. 2, Article ID 021403, 7 pages, 2005.
- [29] N. Bityurin, A. I. Kuznetsov, and A. Kanaev, "Kinetics of UV-induced darkening of titanium-oxide gels," *Applied Surface Science*, vol. 248, no. 1–4, pp. 86–90, 2005.
- [30] J. Huang, M. Wang, J. Zhao, N. Gao, and Y. Li, "Application of concentrated TiO₂ sols for γ -ray radiation dosimetry," *Applied Radiation and Isotopes*, vol. 54, no. 3, pp. 475–481, 2001.
- [31] M. J. Norman, L. D. Morpeth, and J. C. McCallum, "Conditions for the formation of Ti³⁺ by ion implantation of a-axis α -Al₂O₃," *Materials Science and Engineering B*, vol. 106, no. 3, pp. 257–262, 2004.
- [32] R. F. Howe and M. Grätzel, "EPR study of hydrated anatase under UV irradiation," *The Journal of Physical Chemistry*, vol. 91, no. 14, pp. 3906–3909, 1987.
- [33] T. Berger, M. Sterrer, O. Diwald et al., "Light-induced charge separation in anatase TiO₂ particles," *The Journal of Physical Chemistry B*, vol. 109, no. 13, pp. 6061–6068, 2005.
- [34] U. Diebold, J. Lehman, T. Mahmoud et al., "Intrinsic defects on a TiO₂(110)(1 × 1) surface and their reaction with oxygen: a scanning tunneling microscopy study," *Surface Science*, vol. 411, no. 1-2, pp. 137–153, 1998.
- [35] V. E. Henrich and R. L. Kurtz, "Surface electronic structure of TiO₂: atomic geometry, ligand coordination, and the effect of adsorbed hydrogen," *Physical Review B*, vol. 23, no. 12, pp. 6280–6287, 1981.
- [36] G. Lu, A. Linsebigler, and J. T. Yates, "Ti³⁺ defect sites on TiO₂(110): production and chemical detection of active sites," *The Journal of Physical Chemistry*, vol. 98, no. 45, pp. 11733–11738, 1994.
- [37] Y. Li, X. Li, J. Li, and J. Yin, "TiO₂-coated active carbon composites with increased photocatalytic activity prepared by a properly controlled sol-gel method," *Materials Letters*, vol. 59, no. 21, pp. 2659–2663, 2005.
- [38] I. Nakamura, N. Negishi, S. Kutsuna, T. Ihara, S. Sugihara, and K. Takeuchi, "Role of oxygen vacancy in the plasma-treated TiO₂ photocatalyst with visible light activity for NO removal," *Journal of Molecular Catalysis A*, vol. 161, no. 1-2, pp. 205–212, 2000.
- [39] T. Le Mercier, J.-M. Mariot, P. Parent, M.-F. Fontaine, C. F. Hague, and M. Quarton, "Formation of Ti³⁺ ions at the surface of laser-irradiated rutile," *Applied Surface Science*, vol. 86, no. 1–4, pp. 382–386, 1995.
- [40] T. C. Lu, L. B. Lin, S. Y. Wu, C. P. Zhao, X. C. Xu, and Y. F. Tian, "Reduction effects in rutile induced by neutron irradiation," *Nuclear Instruments and Methods in Physics Research, Section B*, vol. 191, no. 1–4, pp. 291–295, 2002.
- [41] Y. Zheng, X. X. Wu, L. He, and W. C. Zheng, "EPR parameters and defect structures of the off-center Ti³⁺ ion on the Sr²⁺ site in neutron-irradiated SrTiO₃ crystal," *Journal of Physics and Chemistry of Solids*, vol. 68, no. 9, pp. 1652–1655, 2007.
- [42] G. D. Bromiley and A. A. Shiryaev, "Neutron irradiation and post-irradiation annealing of rutile (TiO_{2-x}): effect on hydrogen incorporation and optical absorption," *Physics and Chemistry of Minerals*, vol. 33, no. 6, pp. 426–434, 2006.
- [43] J. M. Pan, B. L. Maschhoff, U. Diebold, and T. E. Madey, "Interaction of water, oxygen, and hydrogen with TiO₂ (110) surface having different defect densities," *Journal of Vacuum Science and Technology A*, vol. 10, no. 4, pp. 2470–2476, 1992.
- [44] J. Jun, M. Dhayal, J. H. Shin, J. C. Kim, and N. Getoff, "Surface properties and photoactivity of TiO₂ treated with electron beam," *Radiation Physics and Chemistry*, vol. 75, no. 5, pp. 583–589, 2006.
- [45] S. Dohshi, M. Anpo, S. Okuda, and T. Kojima, "Effect of γ -ray irradiation on the wettability of TiO₂ single crystals," *Topics in Catalysis*, vol. 35, no. 3-4, pp. 327–330, 2005.
- [46] C. M. Greenlief, J. M. White, C. S. Ko, and R. J. Gorte, "An XPS investigation of TiO₂ thin films on polycrystalline Pt," *The Journal of Physical Chemistry*, vol. 89, no. 23, pp. 5025–5028, 1985.
- [47] J. D. Zhang, S. Fung, L. Li-Bin, and L. Zhi-Jun, "Ti ion valence variation induced by ionizing radiation at TiO₂/Si interface," *Surface and Coatings Technology*, vol. 158-159, pp. 238–241, 2002.
- [48] G. B. Hoflund, H. L. Yin, A. L. Grogan et al., "Surface study of the oxidative and reductive properties of TiO₂(001)," *Langmuir*, vol. 4, no. 2, pp. 346–350, 1988.
- [49] Y. Shiraishi, N. Saito, and T. Hirai, "Titanosilicate molecular sieve for size-screening photocatalytic conversion," *Journal of the American Chemical Society*, vol. 127, no. 23, pp. 8304–8306, 2005.
- [50] R. F. Howe and M. Grätzel, "EPR observation of trapped electrons in colloidal TiO₂," *The Journal of Physical Chemistry*, vol. 89, no. 21, pp. 4495–4499, 1985.
- [51] E. Abi Aad and A. Aboukaïs, "Characterisation by EPR spectroscopy," *Catalysis Today*, vol. 56, no. 4, pp. 371–378, 2000.
- [52] S. J. DeCanio, T. M. Apple, and C. R. Dybowski, "Electron spin resonance study of reduced Rh/TiO₂ and TiO₂," *The Journal of Physical Chemistry*, vol. 87, no. 2, pp. 194–196, 1983.
- [53] S. J. DeCanio, J. B. Miller, J. B. Michel, and C. Dybowski, "Electron spin resonance and nuclear magnetic resonance study of the reduction of Rh/TiO₂ systems at 298 K," *The Journal of Physical Chemistry*, vol. 87, no. 23, pp. 4619–4622, 1983.
- [54] M. Grätzel and R. F. Howe, "Electron paramagnetic resonance studies of doped TiO₂ colloids," *The Journal of Physical Chemistry*, vol. 94, no. 6, pp. 2566–2572, 1990.
- [55] J. Dumas, M. Continentino, J. J. Capponi, and J. L. Tholence, "Electron paramagnetic resonance study of the warwickites Mg_{1+x}Ti_{1-x}BO₄," *Solid State Communications*, vol. 106, no. 1, pp. 35–38, 1998.
- [56] T. M. Salama, H. K. Ebitani, H. Hattori, and H. Kita, "Electron paramagnetic resonance studies of reduced platinum

- supported on titanium oxide: effect of hydrogen adsorption-desorption on paramagnetic platinum(I) and titanium(III) species," *Chemistry of Materials*, vol. 6, no. 1, pp. 21–26, 1994.
- [57] J. M. Coronado and J. Soria, "ESR study of the initial stages of the photocatalytic oxidation of toluene over TiO₂ powders," *Catalysis Today*, vol. 123, no. 1–4, pp. 37–41, 2007.
- [58] A. Ookubo, E. Kanazaki, and K. Ooi, "ESR, XRD, and DRS studies of paramagnetic Ti³⁺ ions in a colloidal solid of titanium oxide prepared by the hydrolysis of TiCl₃," *Langmuir*, vol. 6, no. 1, pp. 206–209, 1990.
- [59] K. Komaguchi, H. Nakano, A. Araki, and Y. Harima, "Photoinduced electron transfer from anatase to rutile in partially reduced TiO₂ (P-25) nanoparticles: an ESR study," *Chemical Physics Letters*, vol. 428, no. 4–6, pp. 338–342, 2006.
- [60] T. L. Thompson, O. Diwald, and J. T. Yates Jr., "CO₂ as a probe for monitoring the surface defects on TiO₂(110)-temperature-programmed desorption," *The Journal of Physical Chemistry B*, vol. 107, no. 42, pp. 11700–11704, 2003.
- [61] G. Lu, A. Linsebigler, and J. T. Yates Jr., "Photooxidation of CH₃Cl on TiO₂(110): a mechanism not involving H₂O," *The Journal of Physical Chemistry*, vol. 99, no. 19, pp. 7626–7631, 1995.
- [62] A. Linsebigler, G. Lu, and J. T. Yates Jr., "CO photooxidation on TiO₂(110)," *The Journal of Physical Chemistry*, vol. 100, no. 16, pp. 6631–6636, 1996.
- [63] F. Guillemot, M. C. Porté, C. Labrugère, and C. Baquey, "Ti⁴⁺ to Ti³⁺ conversion of TiO₂ uppermost layer by low-temperature vacuum annealing: interest for titanium biomedical applications," *Journal of Colloid and Interface Science*, vol. 255, no. 1, pp. 75–78, 2002.
- [64] L. Xiong, M. Ouyang, L. Yan, J. Li, M. Qiu, and Y. Yu, "Visible-light energy storage by Ti³⁺ in TiO₂/Cu 2O bilayer film," *Chemistry Letters*, vol. 38, no. 12, pp. 1154–1155, 2009.
- [65] A. Fujishima, T. N. Rao, and D. A. Tryk, "Titanium dioxide photocatalysis," *Journal of Photochemistry and Photobiology C*, vol. 1, no. 1, pp. 1–21, 2000.
- [66] X.-Q. Chen, H.-B. Liu, and G.-B. Gu, "Preparation of nanometer crystalline TiO₂ with high photo-catalytic activity by pyrolysis of titanyl organic compounds and photocatalytic mechanism," *Materials Chemistry and Physics*, vol. 91, no. 2–3, pp. 317–324, 2005.
- [67] A. I. Kuznetsov, O. Kameneva, A. Alexandrov, N. Bityurin, K. Chhor, and A. Kanaev, "Chemical activity of photoinduced Ti³⁺ centers in titanium oxide gels," *The Journal of Physical Chemistry B*, vol. 110, no. 1, pp. 435–441, 2006.
- [68] A. I. Kuznetsov, O. Kameneva, L. Rozes, C. Sanchez, N. Bityurin, and A. Kanaev, "Extinction of photo-induced Ti³⁺ centres in titanium oxide gels and gel-based oxo-PHEMA hybrids," *Chemical Physics Letters*, vol. 429, no. 4–6, pp. 523–527, 2006.
- [69] K. Suriye, B. Jongsomjit, C. Satayaprasert, and P. Praserttham, "Surface defect (Ti³⁺) controlling in the first step on the anatase TiO₂ nanocrystal by using sol-gel technique," *Applied Surface Science*, vol. 255, no. 5, pp. 2759–2766, 2008.
- [70] Z. Xu, J. Shang, C. Liu, C. Kang, H. Guo, and Y. Du, "The preparation and characterization of TiO₂ ultrafine particles," *Materials Science and Engineering B*, vol. 63, no. 3, pp. 211–214, 1999.
- [71] T. Huizinga and R. Prins, "Behavior of Ti³⁺ centers in the low- and high-temperature reduction of Pt/TiO₂, studied by ESR," *The Journal of Physical Chemistry*, vol. 85, no. 15, pp. 2156–2158, 1981.
- [72] T. C. Lu, S. Y. Wu, L. B. Lin, and W. C. Zheng, "Defects in the reduced rutile single crystal," *Physica B*, vol. 304, no. 1–4, pp. 147–151, 2001.
- [73] W. A. Weyl and T. Forland, "Photochemistry of rutile," *Industrial and Engineering Chemistry*, vol. 42, no. 2, pp. 257–263, 1950.
- [74] R. G. Breckenridge and W. R. Hosler, "Electrical properties of titanium dioxide semiconductors," *Physical Review*, vol. 91, no. 4, pp. 793–802, 1953.
- [75] N. Bityurin, L. Znaidi, and A. Kanaev, "Laser-induced absorption in titanium oxide based gels," *Chemical Physics Letters*, vol. 374, no. 1–2, pp. 95–99, 2003.
- [76] H. Sun, Y. Bai, W. Jin, and N. Xu, "Visible-light-driven TiO₂ catalysts doped with low-concentration nitrogen species," *Solar Energy Materials and Solar Cells*, vol. 92, no. 1, pp. 76–83, 2008.
- [77] N. Abd El-Shafi and M. M. Morsi, "Optical absorption and infrared studies of some silicate glasses containing titanium," *Journal of Materials Science*, vol. 32, no. 19, pp. 5185–5189, 1997.
- [78] F. Zuo, L. Wang, T. Wu, Z. Zhang, D. Borchardt, and P. Feng, "Self-doped Ti³⁺ enhanced photocatalyst for hydrogen production under visible light," *Journal of the American Chemical Society*, vol. 132, no. 34, pp. 11856–11857, 2010.
- [79] Y. G. Zhang, L. L. Ma, J. L. Li, and Y. Yu, "In situ Fenton reagent generated from TiO₂/Cu₂O composite film: a new way to utilize TiO₂ under visible light irradiation," *Environmental Science and Technology*, vol. 41, no. 17, pp. 6264–6269, 2007.
- [80] V. V. Laguta, M. D. Glinchuk, R. O. Kuzian et al., "Electron spin resonance of Ti³⁺ in KTa_{0.9}Nb_{0.1}O₃," *Solid State Communications*, vol. 122, no. 5, pp. 277–281, 2002.
- [81] H. Tachikawa, T. Ichikawa, and H. Yoshida, "Hydration structure of titanium(III) ion. ESR and electron spin-echo study," *Journal of the American Chemical Society*, vol. 112, no. 3, pp. 977–982, 1990.
- [82] Y. Li, D. S. Hwang, N. H. Lee, and S. J. Kim, "Synthesis and characterization of carbon-doped titania as an artificial solar light sensitive photocatalyst," *Chemical Physics Letters*, vol. 404, no. 1–3, pp. 25–29, 2005.
- [83] D. R. Park, J. Zhang, K. Ikeue, H. Yamashita, and M. Anpo, "Photocatalytic oxidation of ethylene to CO₂ and H₂O on ultrafine powdered TiO₂ photocatalysts in the presence of O₂ and H₂O," *Journal of Catalysis*, vol. 185, no. 1, pp. 114–119, 1999.
- [84] K. Suriye, P. Praserttham, and B. Jongsomjit, "Impact of Ti³⁺ present in titania on characteristics and catalytic properties of the Co/TiO₂ catalyst," *Industrial and Engineering Chemistry Research*, vol. 44, no. 17, pp. 6599–6604, 2005.
- [85] J. M. Cho, J. M. Seo, J. K. Lee, H. Zhang, and R. Lamb, "Electronic properties of oxygen vacancies in titania nanotubes," *Physica B: Condensed Matter*, vol. 404, no. 1, pp. 127–130, 2009.
- [86] K. Suriye, P. Praserttham, and B. Jongsomjit, "Control of Ti³⁺ surface defect on TiO₂ nanocrystal using various calcination atmospheres as the first step for surface defect creation and its application in photocatalysis," *Applied Surface Science*, vol. 253, no. 8, pp. 3849–3855, 2007.
- [87] S. X. Liu, Z. P. Qu, X. W. Han, and C. L. Sun, "A mechanism for enhanced photocatalytic activity of silver-loaded titanium dioxide," *Catalysis Today*, vol. 93–95, pp. 877–884, 2004.
- [88] E. A. Konstantinova, A. I. Kokorin, S. Sakthivel, H. Kisch, and K. Lips, "Carbon-doped titanium dioxide: visible light

- photocatalysis and EPR investigation,” *Chimia*, vol. 61, no. 12, pp. 810–814, 2007.
- [89] W. Kongsuebchart, P. Praserthdam, J. Panpranot, A. Sirisuk, P. Supphasrironjaroen, and C. Satayaprasert, “Effect of crystallite size on the surface defect of nano-TiO₂ prepared via solvothermal synthesis,” *Journal of Crystal Growth*, vol. 297, no. 1, pp. 234–238, 2006.
- [90] A. I. Kokorin and D. W. Bahnemann, Eds., *Chemical Physics of Nanostructured Semiconductors VSP-Brill*, Academic Publishers, Utrecht, The Netherlands, 2003.
- [91] Y. Nakaoka and Y. Nosaka, “ESR Investigation into the effects of heat treatment and crystal structure on radicals produced over irradiated TiO₂ powder,” *Journal of Photochemistry and Photobiology A*, vol. 110, no. 3, pp. 299–305, 1997.
- [92] M. A. Henderson, “Evidence for bicarbonate formation on vacuum annealed TiO₂(110) resulting from a precursor-mediated interaction between CO₂ and H₂O,” *Surface Science*, vol. 400, no. 1–3, pp. 203–219, 1998.
- [93] A. Markovits, A. Fahmi, and C. Minot, “A theoretical study of CO₂ adsorption on TiO₂,” *Journal of Molecular Structure: THEOCHEM*, vol. 371, no. 1–3, pp. 219–235, 1996.
- [94] A. Fujishima and X. Zhang, “Titanium dioxide photocatalysis: present situation and future approaches,” *Comptes Rendus Chimie*, vol. 9, no. 5-6, pp. 750–760, 2006.
- [95] R. Asahi, T. Morikawa, T. Ohwaki, K. Aoki, and Y. Taga, “Visible-light photocatalysis in nitrogen-doped titanium oxides,” *Science*, vol. 293, no. 5528, pp. 269–271, 2001.
- [96] S. Livraghi, M. C. Paganini, E. Giamello, A. Selloni, C. Di Valentin, and G. Pacchioni, “Origin of photoactivity of nitrogen-doped titanium dioxide under visible light,” *Journal of the American Chemical Society*, vol. 128, no. 49, pp. 15666–15671, 2006.
- [97] C. Di Valentin, E. Finazzi, G. Pacchioni et al., “N-doped TiO₂: theory and experiment,” *Chemical Physics*, vol. 339, no. 1–3, pp. 44–56, 2007.
- [98] H. L. Qin, G. B. Gu, and S. Liu, “Preparation of nitrogen-doped titania with visible-light activity and its application,” *Comptes Rendus Chimie*, vol. 11, no. 1-2, pp. 95–100, 2008.
- [99] S. Yamazaki, S. Tanaka, and H. Tsukamoto, “Kinetic studies of oxidation of ethylene over a TiO₂ photocatalyst,” *Journal of Photochemistry and Photobiology A*, vol. 121, no. 1, pp. 55–61, 1999.
- [100] J. Yu, X. Zhao, and Q. Zhao, “Photocatalytic activity of nanometer TiO₂ thin films prepared by the sol-gel method,” *Materials Chemistry and Physics*, vol. 69, no. 1–3, pp. 25–29, 2001.
- [101] M. A. Henderson, “Photooxidation of acetone on TiO₂(110): conversion to acetate via methyl radical ejection,” *The Journal of Physical Chemistry B*, vol. 109, no. 24, pp. 12062–12070, 2005.
- [102] P. Supphasrironjaroen, P. Praserthdam, J. Panpranot, D. Naranong, and O. Mekasuwandumrong, “Effect of quenching medium on photocatalytic activity of nano-TiO₂ prepared by solvothermal method,” *Chemical Engineering Journal*, vol. 138, no. 1–3, pp. 622–627, 2008.

Research Article

Porous Diatomite-Immobilized Cu–Ni Bimetallic Nanocatalysts for Direct Synthesis of Dimethyl Carbonate

Yong Chen,¹ Min Xiao,¹ Shuanjin Wang,¹ Dongmei Han,¹ Yixin Lu,² and Yuezhong Meng¹

¹ State Key Laboratory of Optoelectronic Materials and Technologies and The Key Laboratory of Low-Carbon Chemistry & Energy Conservation of Guangdong Province, Sun Yat-Sen University, Guangzhou 510275, China

² Department of Chemistry and Medicinal Chemistry Program, Office of Life Sciences, National University of Singapore, 3 Science Drive 3, Singapore 117543

Correspondence should be addressed to Shuanjin Wang, wangshj@mail.sysu.edu.cn and Yuezhong Meng, mengyzh@mail.sysu.edu.cn

Received 23 March 2011; Revised 18 July 2011; Accepted 17 August 2011

Academic Editor: Mohammad Reza Bayati

Copyright © 2012 Yong Chen et al. This is an open access article distributed under the Creative Commons Attribution License, which permits unrestricted use, distribution, and reproduction in any medium, provided the original work is properly cited.

A series of diatomite-immobilized Cu–Ni bimetallic nanocatalysts was prepared under ultrasonication and evaluated for the direct synthesis of dimethyl carbonate under various conditions. Upon being fully characterized by TPR, TPD, BET, SEM, XRD, and XPS methodologies, it is found that the bimetallic composite is effectively alloyed and well immobilized inside or outside the pore of diatomite. Under the optimal conditions of 1.2 MPa and 120°C, the prepared catalyst with loading of 15% exhibited the highest methanol conversion of 6.50% with DMC selectivity of 91.2% as well as more than 10-hour lifetime. The possible reaction mechanism was proposed and discussed in detail. To our knowledge, this is the first report to use diatomite as a catalyst support for direct DMC synthesis from methanol and CO₂.

1. Introduction

Dimethyl carbonate (DMC), an environment-friendly chemical, has attracted much attention as methylating and carbonylating agents, fuel additives, as well as polar solvents [1–4]. Several commercial processes have been introduced for synthesis of DMC, including methanolysis of phosgene [5], ester exchange process [6, 7], methanolysis of urea [8], and gas-phase oxidative carbonylation of methanol [9]. However, all these processes use toxic, corrosive, flammable, and explosive gases such as phosgene, hydrogen chloride, and carbon monoxide. Therefore, direct synthesis of DMC from CH₃OH and CO₂ is highly desired since such an approach is environment friendly by nature [1].

Carbon dioxide, the main greenhouse gas, can be converted into synthetic gas, methanol, acetic acid, carbonate, and so forth, [10]. However, it is still a big challenge for synthetic chemists to utilize CO₂ effectively due to its in-built thermodynamic stability and kinetic inertness. Recently, a large number of catalysts have been reported for the

direct synthesis of DMC from CO₂ and CH₃OH including organometallic compounds [11], potassium methoxide [12], ZrO₂, Ce_{0.5}Zr_{0.5}O₂ and H₃PW₁₂O₄-Ce_xTi_{1-x}O₂, [13–15], H₃PO₄-V₂O₅ catalyst [16], and so forth. However, the highest DMC yield was still very low without addition of strong base and dehydrating agent due to the difficulties in activation of CO₂ and the deactivation of catalysts by in situ produced water. Copper and nickel composite, a type of novel bimetallic catalyst, was firstly proved highly active for direct synthesis of DMC by the Zhong Group [17]. In our group, Wu et al. further optimized the preparation condition and catalytic process of the catalysts [18]. For enhancing the efficiency of Cu–Ni catalysts, Wang et al. tested the similar Cu–(Ni,V,O)/SiO₂ catalyst with UV irradiation and pushed DMC yield close to 5% [19, 20]. Recently Bian et al. pioneered to support Cu–Ni composite on conductive carbon materials and firstly improved the methanol conversion to 10.13% with DMC selectivity of 90.2% [21, 22]. The catalysts above mentioned offer different advantages over others before them but also have considerable shortcomings

such as complicated preparation process, expensive support, and bleak prospect for industrialization. Therefore, new catalysts with low cost, high catalytic performance, and simple preparation process are urgently required.

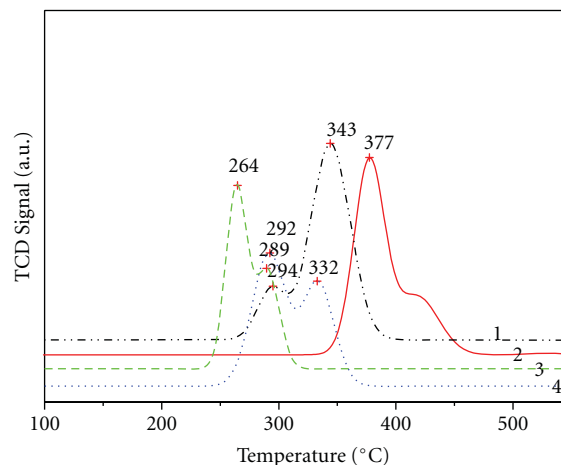
Diatomite, a type of widespread natural porous material, has been widely used as filler aid, adsorbent, and catalytic support in the reaction such as hydrogenation [23], oxidation [24], Fischer-Tropsch synthesis [25], CO₂ reduction [26] and so forth due to its unique high-adsorption capacity, high surface area, and cheap availability. In this connection, a series of Cu–Ni/diatomite bimetallic catalysts were prepared and evaluated under variable reaction conditions in this work.

2. Experimental

2.1. Catalyst Preparation. Natural diatomite was pretreated by calcining at 500°C for 3 h, soaking in 5% hydrochloric acid for 24 h, and washing and drying at 110°C overnight. Cu–Ni/diatomite nanocatalyst was prepared by the wetness impregnation method. Firstly Cu(NO₃)₂·3H₂O (0.517 g) and Ni(NO₃)₂·6H₂O (0.311 g) were dissolved in 25 mL of 25 wt% ammonia solution by stirring, then 5 g of diatomite was dispersed in metallic ammonia solution. The resulting mixture was stirred at room temperature for 24 h, ultrasonicated for another 3 h, followed by rotavaporation to remove the solvent. Thereafter, it was dried at 110°C overnight. The fully dried solid was calcined at 500°C for 5 h and further reduced by 5% H₂/N₂ mixture at 550°C for 6 h.

2.2. Catalyst Characterization. The surface area of the samples was detected in liquid N₂ by the Brunauer-Emmett-Teller (BET) approaches using a Micromeritics ASAP 2010 instrument. Thermogravimetric analyses (TGA) of samples were performed on a PerkinElmer Pyris Diamond SII thermal analyzer (high-purity N₂, 20°C/min). The morphologies of the samples were examined using a scanning electron microscopy (SEM) (JSM-5600LV system of JEOL) equipped with an energy dispersive X-ray spectrometer (EDX) to check the components of the catalysts. The phase structure of the samples were determined by X-ray diffraction (XRD) on a D/Max-III A power diffractometer using Cu (K α) (0.15406 nm) radiation source. X-ray photoelectron spectrum (XPS) of the catalysts was obtained by ESCALAB 250 (Thermo-VG Scientific) analyzer using the monochromatized Al (K α) radiation source. Temperature-programmed reduction (TPR)/temperature-programmed desorption of ammonia (NH₃-TPD) experiments of the samples were detected by Quantachrome ChemBET 3000 apparatus equipped with a thermal conductivity detector (TCD) [22].

The evaluation of the catalysts was performed in a continuous tubular fixed-bed microgaseous reactor with 2 g of the fresh catalyst and 2/1 molar ratio of CH₃OH/CO₂ (30 mL/min flux). It was carried out at different temperatures and different pressures. The product was analyzed by on-line GC (GC7890F) equipped with a flame ionization detector



- (1) 15% CuO/diatomite
- (2) 15% NiO/diatomite
- (3) 15% (2CuO-NiO)
- (4) 15% (2CuO-NiO)/diatomite

FIGURE 1: TPR test of the samples.

and GCMS-QP2010 Plus. The final results were calculated by the following equations:

$$\text{CH}_3\text{OH conversion (\%)} = \frac{[\text{CH}_3\text{OH reacted}]}{[\text{CH}_3\text{OH total}]} \times 100\%,$$

$$\text{DMC selectivity (\%)} = \frac{[\text{DMC}]}{[\text{DMC} + \text{Byproduct}]} \times 100\%,$$

$$\text{DMC yield (\%)} = \text{CH}_3\text{OH conversion} \\ \times \text{DMC selectivity} \times 100\%.$$

(1)

3. Results and Discussion

3.1. Structural Investigation of the Catalysts. Natural diatomite was simply pretreated to further enlarge the surface area. Intensive stirring and more than 3 h strong ultrasonication were pretty favorable for impregnation of bimetallic solution. TPR of the samples was shown in Figure 1. The supported bimetallic catalyst shows two closely overlapped reduction peaks, one was the reduction of CuO (292°C) and the other was the reduction of NiO (332°C). Moreover, the reduction temperature of supported bimetallic catalyst shifted to lower temperature than monometallic catalyst, indicating the tremendous contribution of strong interaction of copper and nickel. In addition, the reduction temperature of supported bimetallic catalyst was higher than unsupported bimetallic composite (CuO 264°C, NiO 289°C), attributing to the strong interaction of bimetallic composite with support.

Morphology of the samples was observed by SEM as presented in Figure 2. Diatomite was porous disc with some blocked pore before pretreatment (a). After pretreatment, it was disintegrated into fragment with all-over straightway

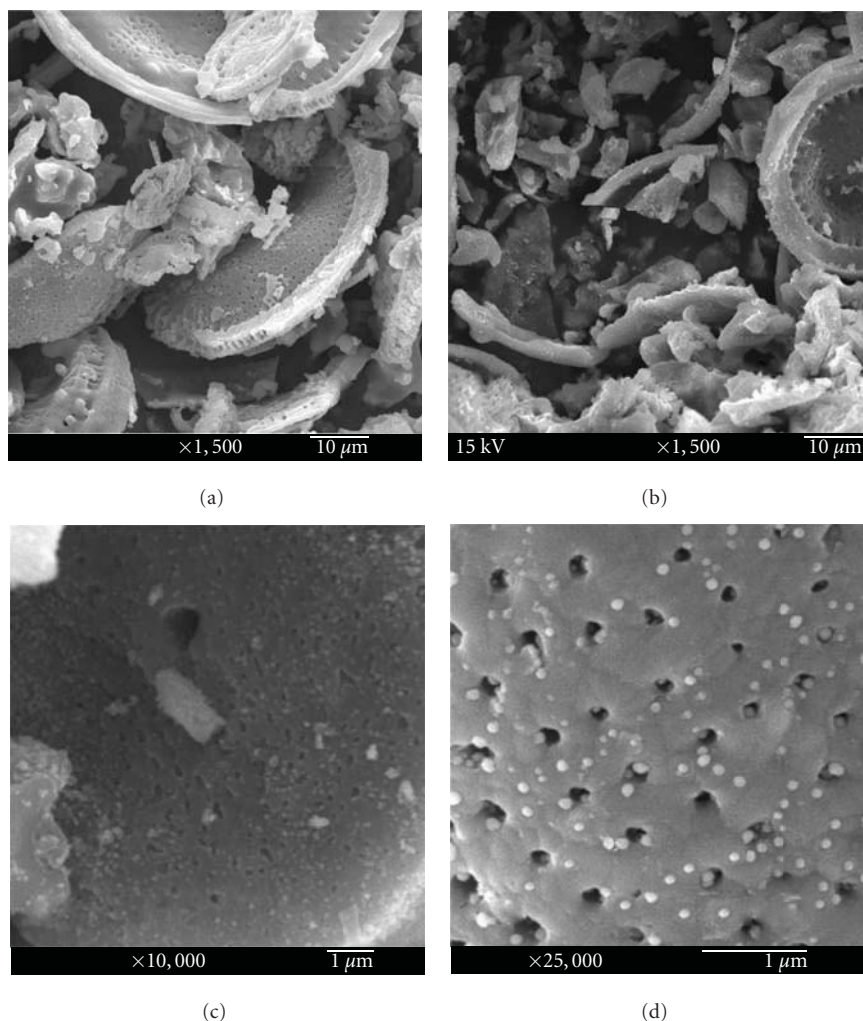


FIGURE 2: SEM of the samples. (a) Natural diatomite, (b) treated diatomite, (c) 15% (2Cu–Ni)/diatomite ($\times 10000$), and (d) 15% (2Cu–Ni)/diatomite ($\times 25000$).

pore (b), which was quite preferable for bimetallic dispersion and catalytic activity improvement. As shown in (c), diatomite was homogeneously covered by bimetallic nanoparticles not only immobilizing on the surface, but also a great deal of them inlaying, the inner wall of the pore (d) which is quite preferred for bimetallic dispersion and stabilization.

Quantitative element analysis of the catalyst was performed by EDS (Figure SM1 which is available online at doi:10.1155/2012/610410). The average results of area analysis were Cu 8.12%, Ni 3.86%, Si 38.73%, O 47.87% with a little amount of Fe, Al, Mn which further confirmed that the bimetallic components were effectively loaded. Oxidative state of the element was determined by XPS (Figure 3). The survey scan spectra indicated bimetallic components of Cu and Ni was dispersed throughout the surface of the support besides a little ferric, manganic and aluminous oxides were also included in this system coming from diatomite which may be good active additives (c). Cu 2p scan (a) and Ni 2p scan (b) displayed that binding energy of Cu and Ni was located at 932.73 (Cu 2p_{3/2}), 852.80 (Ni 2p_{3/2}),

951.70 (Cu 2p_{1/2}), 858.60 (Ni 2p_{1/2}), 918.70 (Cu LMM), and 846.20 (Ni LMM) respectively, which indicated that Cu–Ni composite was almost fully reduced. The XRD patterns of the samples were shown in Figure 4. Curve (a) was the typical patterns of diatomite with some weak diffractions of ferric oxide, alumina, and manganese dioxide. Compared with curve (a), curve (b) displayed new peaks of CuO and NiO accompanied by little diffraction of Cu₂O. Instead of diffraction of CuO and NiO, these newly emerged peaks in curve (c) ($2\theta = 43.62, 51.06, 74.94, \text{ and } 91.04$) were characteristic diffraction of Cu–Ni alloy. Interestingly it was not two close diffraction peaks of Cu and Ni as depicted in [27] but a single peak of Cu–Ni alloy, which may be due to the highly homogeneous distribution of Cu and Ni in Cu–Ni nanoparticles resulting from the contribution of ultrasonic dispersion and support effect.

3.2. Adsorption Behavior of the Support and Catalyst. The specific surface area of the support and catalyst was conducted by the BET method. Natural and treated diatomite

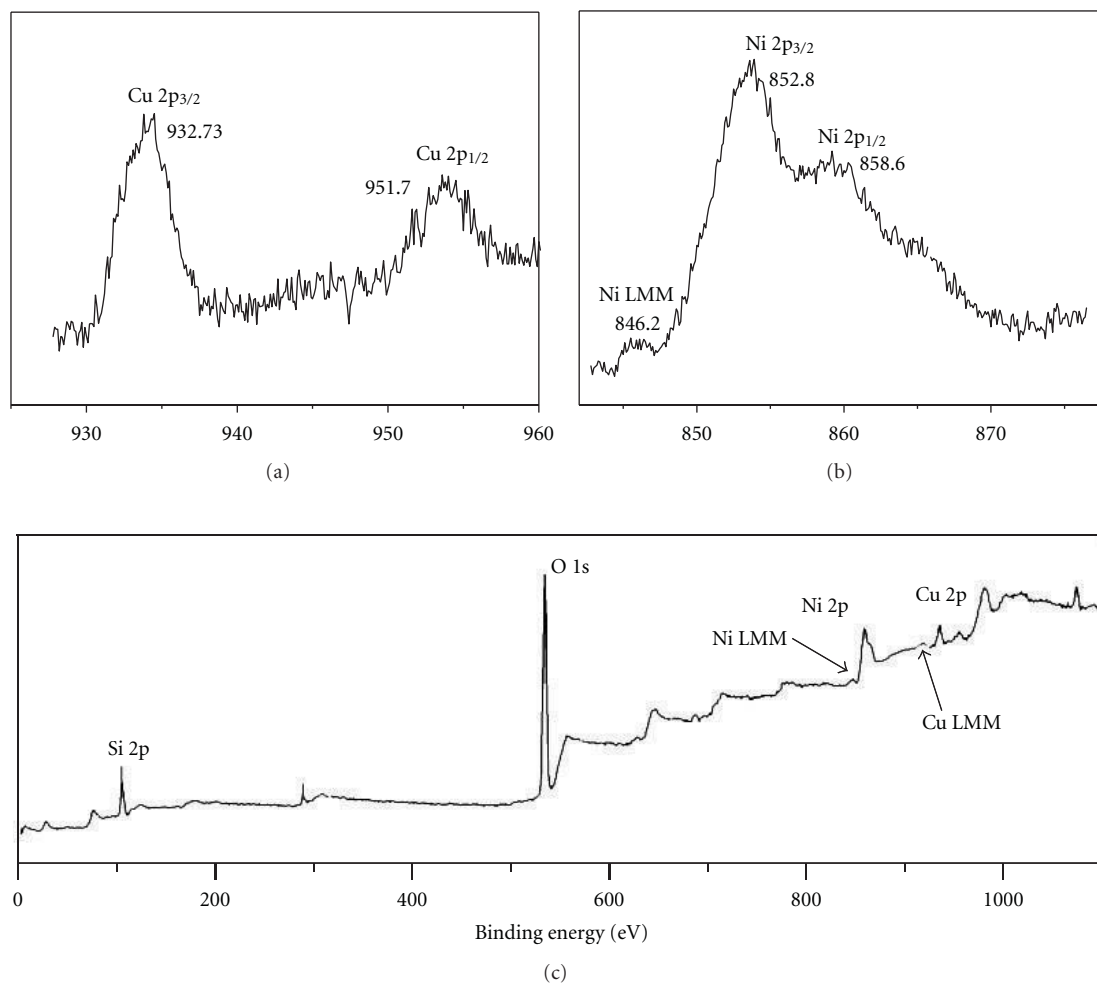


FIGURE 3: XPS of 15% (2Cu-Ni)/diatomite catalyst. (a) Cu 2p scan, (b) Ni 2p scan, and (c) survey scan.

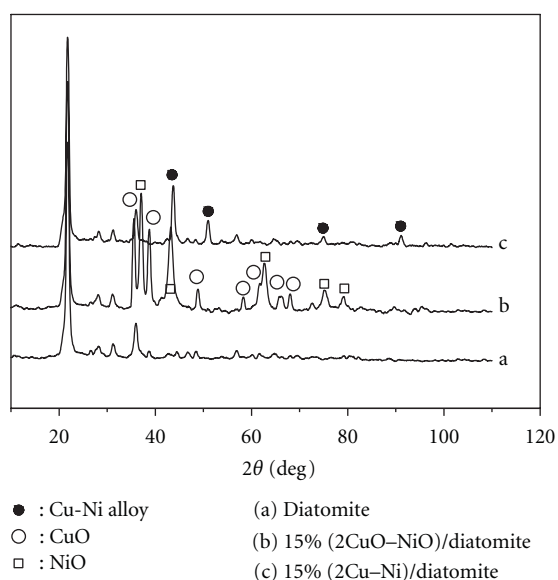
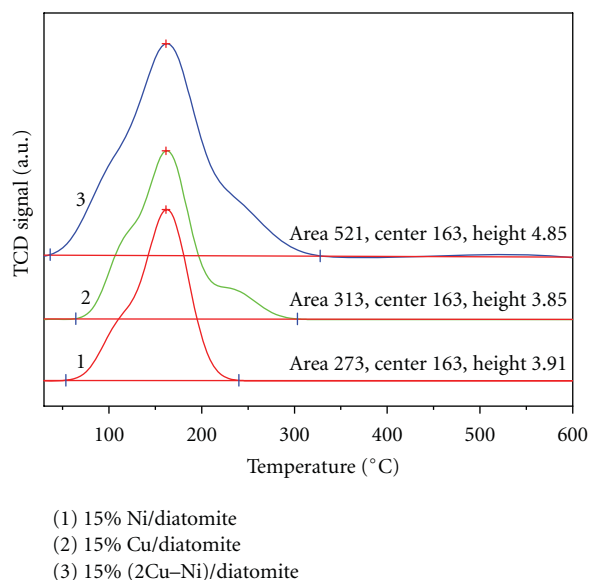


FIGURE 4: XRD patterns of the samples. (a) treated diatomite, (b) 15% (2CuO-NiO)/diatomite, and (c) 15% (2Cu-Ni)/diatomite.

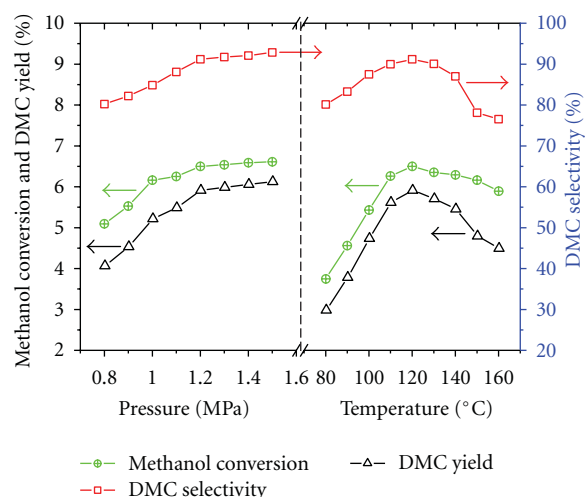
were 58.36 and 77.57 m²/g, respectively. NH₃-TPD profiles of the samples were presented in Figure 5, it can be found that the desorption peak area of bimetallic catalyst was larger than those of monometallic catalyst, and all desorption was divided into three stages that were physical desorption, hydrogen-bonding desorption, acid-centered desorption around 130°C, 180°C, and 270°C, respectively. Physical desorption mainly results from surface sorption of the catalyst in order to reduce its surface free energy. In addition, bimetallic catalyst showed a little stronger physical desorption than monometallic catalyst. Hydrogen-bonding desorption comes from the strong interaction between free Si-OH and NH₃. Strong acid-centered desorption arises from the nude M⁺ center (M = Si, Cu, Ni, Al, etc.), and the number of the acid center increases with increasing of their desorption peak area. Meanwhile, the higher the temperature of the peak is, the stronger the acid center represents. It was worth noting that the acid strength increased with the order of 15% (2Cu-Ni)/diatomite, 15% Cu/diatomite, and 15% Ni/diatomite, which was consistent with the order of their catalytic activity (see Table 1) and the acid-base catalysis mechanism [13, 28].

FIGURE 5: NH₃-TPD profiles of the catalysts.

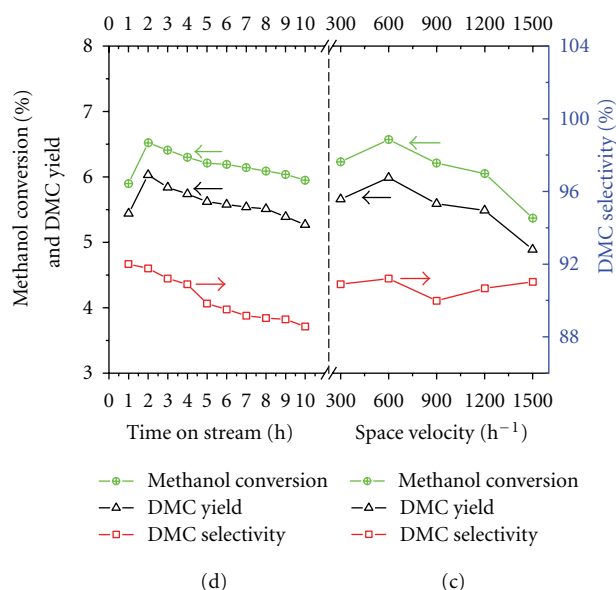
3.3. Study on Performance of the Catalyst. The effect of loading on DMC synthesis was listed in Table 1. The loading ranges from 3 wt% to 25 wt% with 2/1 of Cu/Ni [21], and the optimum loading was 15%. The bimetallic catalysts were superior to monometallic catalysts which further verified the synergetic effect of the Cu–Ni alloy [21].

The effect of pressure, temperature, and space velocity on highly active 15% (2Cu–Ni)/diatomite catalyst was evaluated as the most important factors (Figure 6). The CH₃OH conversion, DMC yield, and selectivity were enhanced noticeably with pressure increase (6a). Nevertheless, it leveled off when pressure climbed over 1.2 MPa, indicating much higher pressure would have less effect on the reaction. Under set conditions of 1.2 MPa and 600 h⁻¹, it gives the highest methanol conversion of 4.50% with DMC selectivity of 88.4% at 120°C (6b). Although increasing temperature was more favorable for activation of CH₃OH and CO₂, the catalytic performance decreased obviously over 120°C likely due to the CO₂ and methanol desorption and the change of catalytic transition state. When the reaction was fixed at 120°C and 1.2 MPa, methanol conversion increased a little with increasing space velocity from 300 to 600 h⁻¹ (6c), after that it collapsed gradually from 600 to 1500 h⁻¹ because the reaction time correspondingly decreased with the increase of space velocity.

Stability test of the catalyst was conducted at 120°C, 1.2 MPa and 600 h⁻¹ (6d). The variation of CH₃OH conversion and DMC selectivity with time was represented by stream on hour (5c). The CH₃OH conversion climbs to the highest value of 4.57% within 2 h likely due to the initiation of active species in the initial reaction stage, finally it decreased slowly to 2.95%. Simultaneously the DMC selectivity fluctuated from 92.0 to 88.6% probably resulting from the active center was poisoned by in situ produced water and surficial oxidation of the catalyst. The byproducts were CO, HCHO, and dimethyl ether (DME) detected by



(a) (b)



(d) (c)

FIGURE 6: (a) Dependence of 15% (2Cu–Ni)/diatomite performance on pressure (120°C, 600 h⁻¹ GHSV). (b) Dependence of 15% (2Cu–Ni)/diatomite performance on temperature (1.2 MPa, 600 h⁻¹ GHSV). (c) Dependence of 15% (2Cu–Ni)/diatomite performance on space velocity (1.2 MPa, 120°C). (d) Stability test of 15% (2Cu–Ni)/diatomite (120°C, 1.2 MPa, 600 h⁻¹ GHSV). 2 g catalyst and $n\text{CH}_3\text{OH}/n\text{CO}_2 = 2/1$ were used for all tests.

GC-MS in this reaction. CO presumably came from the cleavage of C–O bond of the activated CO₂, whilst HCHO and DME may result from the activated CH₃OH.

4. Proposed Reaction Mechanism

In view of the above experimental results, a different reaction mechanism from the literatures [21, 22] was proposed based on the results of GC-MS and in situ FTIR. As shown in

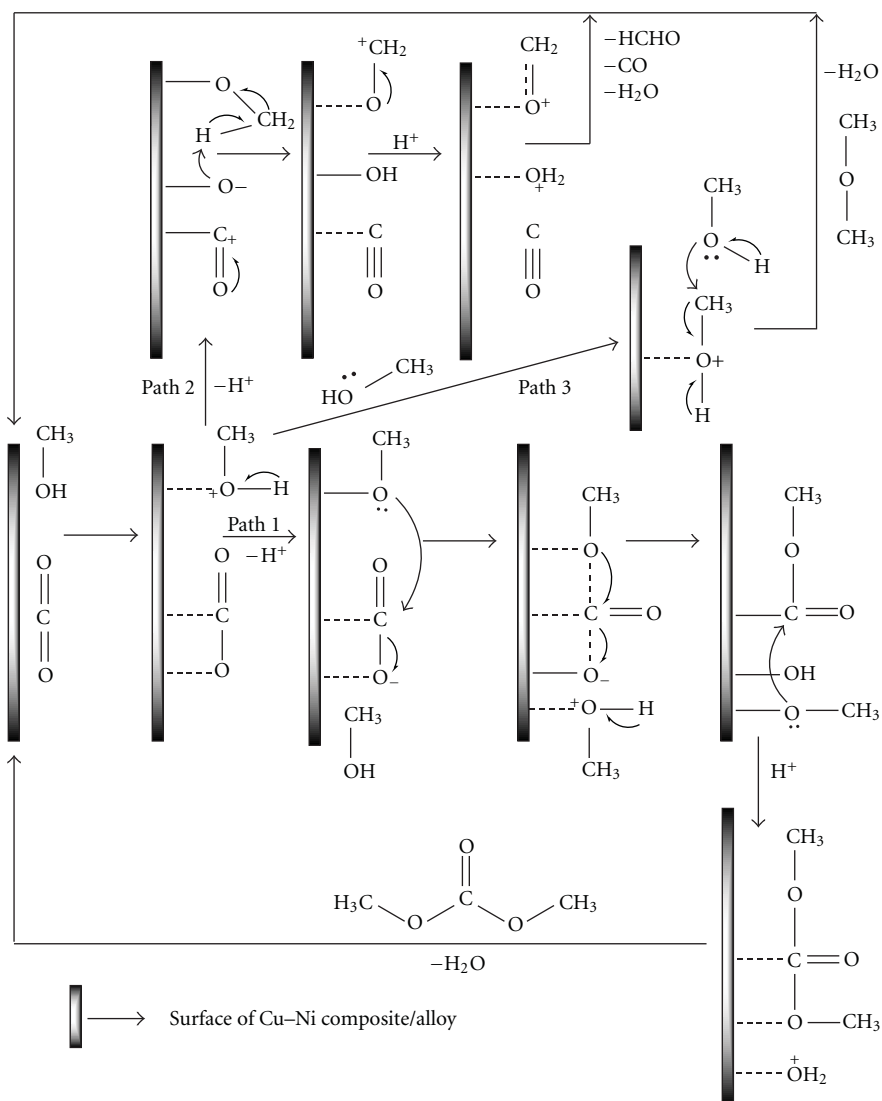


FIGURE 7: The proposed catalytic reaction mechanism for direct DMC synthesis from CH₃OH and CO₂ over Cu-Ni/diatomite.

TABLE 1: Influence of bimetallic loading on the direct synthesis of DMC.

Entry	Loading (wt%) ^a (2CuO + NiO)	Methanol conversion ^b (%)	DMC selectivity (%)	DMC yield (%)
1	3	2.32	89.4	1.86
2	5	2.73	90.2	2.17
3	10	3.96	90.9	2.42
4	15	4.50	91.2	3.93
5	20	4.05	88.7	3.36
6	25	3.67	86.1	2.88
7 ^c	15	2.31	92.0	2.13
8 ^d	15	0.58	91.5	0.53

^aMolar ratio of CuO/NiO is 2/1; ^breaction conditions: 120°C; 1.2 MPa; ^conly Cu was loaded; ^donly Ni was loaded.

Figure 7, a large number of basic (M⁻) and acid (M⁺) centers existed on the surface of Cu-Ni nanocomposite or the interface between Cu-Ni and support, which were the residual bonds resulted from the synergetic interaction of Cu with Ni or Cu-Ni with support. CH₃OH and CO₂

were firstly adsorbed on those M⁺ and M⁻, respectively, simultaneously accompanied by methanol dehydrogenation and CO₂ deoxygenation, which was the rate-determining step. DMC was formed by reaction path 1; CO and HCHO came out by path 2; DME was produced by dehydration

of two methanol molecules through path 3. M^+ and M^- centers were regenerated and recycled by desorption of those produced molecules under heating. Otherwise those active centers were deactivated by O or $-OH$ groups which were responsible for the loss of catalysis activity and the oxidization of Cu–Ni, so the existence of H_2O may be lethal for this reaction. Although the real reaction path was not well understood and verified, this proposed reaction mechanism compared to the literatures [21, 22] will help us to better understand and explain the reaction results, and it offers us a direction to improve the catalytic efficiency of this reaction.

5. Conclusions

In this work, low-cost and porous natural diatomite can be effectively introduced as a catalyst support by simple pretreatment for direct synthesis of DMC from carbon dioxide and methanol. The 2Cu–Ni/diatomite catalysts prove highly active for direct synthesis of DMC, and 15% (2Cu–Ni)/diatomite gives the highest methanol conversion of 4.50 with DMC selectivity of 91.2% together with more than 6-hour lifetime ($120^\circ C$, 1.2 MPa). From the results of experiments, the bimetallic nanoparticles are well dispersed and presumably alloyed under the preparation conditions. The existence of electron-rich and electron-deficient centers resulted from the strong interaction of diatomite with Cu–Ni, and the synergy of Cu–Ni alloy may be responsible for the high activity of this catalyst. This work can facilitate us to better understand the mechanism of this reaction and speed the scientific progress of peers in direct synthesis of DMC.

Acknowledgments

The authors would like to thank the China High-Tech Development 863 Program (2009AA034900, 2009AA03Z340), the Guangdong Province Universities and Colleges Pearl River Scholar Funded Scheme (2010), the Guangdong Province Sci & Tech Bureau (Key Strategic Project Grant no. 2008A080800024, 10151027501000096), and the Guangdong Education Bureau (Key Project. cxzd1004), the Chinese Universities Basic Research Founding for financial support of this work.

References

- [1] M. Aresta and E. Quaranta, "Carbon dioxide: a substitute for phosgene," *CHEMTECH*, vol. 27, no. 3, pp. 32–40, 1997.
- [2] A. A. G. Shaikh and S. Sivaram, "Organic carbonates," *Chemical Reviews*, vol. 96, no. 3, pp. 951–976, 1996.
- [3] P. Tundo, G. Moraglio, and F. Trotta, "Gas-liquid phase-transfer catalysis: a new continuous-flow method in organic synthesis," *Industrials and Engineering Chemistry Research*, vol. 28, no. 7, pp. 881–890, 1989.
- [4] Y. Ono, "Catalysis in the production and reactions of dimethyl carbonate, an environmentally benign building block," *Applied Catalysis A*, vol. 155, no. 2, pp. 133–166, 1997.
- [5] P. G. Jessop, T. Ikariya, and R. Noyori, "Homogeneous catalysis in supercritical fluids," *Chemical Reviews*, vol. 99, no. 2-3, pp. 475–493, 1999.
- [6] M. S. Han, B. G. Lee, B. S. Ahn, K. Y. Park, and S. I. Hong, "Kinetics of dimethyl carbonate synthesis from ethylene carbonate and methanol using alkali-metal compounds as catalysts," *Reaction Kinetics and Catalysis Letters*, vol. 73, no. 1, pp. 33–38, 2001.
- [7] T. Tatsumi, Y. Watanabe, and K. A. Koyano, "Synthesis of dimethyl carbonate from ethylene carbonate and methanol using TS-1 as solid base catalyst," *Chemical Communications*, no. 19, pp. 2281–2282, 1996.
- [8] M. Wang, N. Zhao, W. Wei, and Y. Sun, "Synthesis of dimethyl carbonate from urea and methanol over ZnO ," *Industrial and Engineering Chemistry Research*, vol. 44, no. 19, pp. 7596–7599, 2005.
- [9] J. Puga, M. E. Jones, D. C. Molzahn, and G. E. Hartwell, "Production of dialkyl carbonates using copper catalysts," U.S. Patent 5387708, 1995.
- [10] K. M. Yu, I. Curcic, J. Gabriel, and S. C. Tsang, "Recent advances in CO_2 capture and utilization," *ChemSusChem*, vol. 1, no. 11, pp. 893–899, 2008.
- [11] J. C. Choi, K. Kohno, Y. Ohshima, H. Yasuda, and T. Sakakura, "Tin- or titanium-catalyzed dimethyl carbonate synthesis from carbon dioxide and methanol: large promotion by a small amount of triflate salts," *Catalysis Communications*, vol. 9, no. 7, pp. 1630–1633, 2008.
- [12] Q. Cai, C. Jin, B. Lu, H. Tangbo, and Y. Shan, "Synthesis of dimethyl carbonate from methanol and carbon dioxide using potassium methoxide as catalyst under mild conditions," *Catalysis Letters*, vol. 103, no. 3-4, pp. 225–228, 2005.
- [13] K. Tomishige, T. Sakaihorii, Y. Ikeda, and K. Fujimoto, "A novel method of direct synthesis of dimethyl carbonate from methanol and carbon dioxide catalyzed by zirconia," *Catalysis Letters*, vol. 58, no. 4, pp. 225–229, 1999.
- [14] K. W. La and I. K. Song, "Direct synthesis of dimethyl carbonate from CH_3OH and CO_2 by $H_3PW_{12}O_{40}/CexTi_{1-x}O_2$ catalyst," *Reaction Kinetics and Catalysis Letters*, vol. 89, no. 2, pp. 303–309, 2006.
- [15] Z. F. Zhang, Z. T. Liu, Z. W. Liu, and J. Lu, "DMC formation over $Ce_{0.5}Zr_{0.5}O_2$ prepared by complex-decomposition method," *Catalysis Letters*, vol. 129, no. 3-4, pp. 428–436, 2009.
- [16] X. L. Wu, M. Xiao, Y. Z. Meng, and Y. X. Lu, "Direct synthesis of dimethyl carbonate on H_3PO_4 modified V_2O_5 ," *Journal of Molecular Catalysis A*, vol. 238, no. 1-2, pp. 158–162, 2005.
- [17] S. Zhong, H. Li, J. Wang, and X. Xiao, "Study on Cu–Ni/ ZrO_2 – SiO_2 catalyst for direct synthesis of DMC from CO_2 and CH_3OH ," *Chinese Journal of Catalysis*, vol. 21, no. 2, pp. 117–120, 2000.
- [18] X. L. Wu, Y. Z. Meng, M. Xiao, and Y. X. Lu, "Direct synthesis of dimethyl carbonate (DMC) using Cu–Ni/ V_2O_5 as catalyst," *Journal of Molecular Catalysis A*, vol. 249, pp. 93–97, 2006.
- [19] X. J. Wang, M. Xiao, S. J. Wang, Y. X. Lu, and Y. Z. Meng, "Direct synthesis of dimethyl carbonate (DMC) from methanol and carbon dioxide under pressure and UV irradiation," *Research Journal of Chemistry and Environment*, vol. 12, no. 2, pp. 22–26, 2008.
- [20] X. J. Wang, M. Xiao, S. J. Wang, Y. X. Lu, and Y. Z. Meng, "Direct synthesis of dimethyl carbonate from carbon dioxide and methanol using supported copper (Ni, V, O) catalyst with photo-assistance," *Journal of Molecular Catalysis A*, vol. 278, no. 1-2, pp. 92–96, 2007.
- [21] J. Bian, M. Xiao, S. Wang, X. Wang, Y. Lu, and Y. Meng, "Highly effective synthesis of dimethyl carbonate from methanol and carbon dioxide using a novel copper-nickel/graphite bimetallic nanocomposite catalyst," *Chemical Engineering Journal*, vol. 147, no. 2-3, pp. 287–296, 2009.

- [22] J. Bian, M. Xiao, S. Wang, Y. Lu, and Y. Meng, "Direct synthesis of DMC from CH₃OH and CO₂ over V-doped Cu-Ni/AC catalysts," *Catalysis Communications*, vol. 10, no. 8, pp. 1142–1145, 2009.
- [23] D. J. Zhou, D. Q. Zhou, X. H. Cui, F. M. Wang, M. Y. Huang, and Y. Y. Jiang, "Hydrogenation of aldehydes catalyzed by kieselguhr-supported carboxymethylcellulose-nickel complex," *Polymers for Advanced Technologies*, vol. 15, no. 4, pp. 218–220, 2004.
- [24] C. S. Yao and H. S. Weng, "Liquid-phase oxidation of cyclohexanone to dibasic acids over supported cerium catalysts," *Chemical Engineering Science*, vol. 47, no. 9–11, pp. 2745–2750, 1992.
- [25] S. Bessell, "Support effects in cobalt-based fischer-tropsch catalysis," *Applied Catalysis A*, vol. 96, no. 2, pp. 253–268, 1993.
- [26] K. Ogura, M. Kawano, and D. Adachi, "Dark catalytic reduction of CO₂ over photo-pretreated NiO/ksg catalyst," *Journal of Molecular Catalysis*, vol. 72, no. 2, pp. 173–179, 1992.
- [27] M. D. Cangiano, A. C. Carreras, M. W. Ojeda, and M. D. Ruiz, "A new chemical route to synthesize Cu-Ni alloy nanostructured particles," *Journal of Alloys and Compounds*, vol. 458, no. 1-2, pp. 405–409, 2008.
- [28] K. W. La, J. C. Jung, H. Kim, S. H. Baeck, and I. K. Song, "Effect of acid-base properties of H₃PW₁₂O₄₀/CexTi_{1-x}O₂ catalysts on the direct synthesis of dimethyl carbonate from methanol and carbon dioxide: aTPD study of H₃PW₁₂O₄₀/CexTi_{1-x}O₂ catalysts," *Journal of Molecular Catalysis A*, vol. 269, no. 1-2, pp. 41–45, 2007.

Research Article

ZnO Nanoparticles on Si, Si/Au, and Si/Au/ZnO Substrates by Mist-Atomisation

Z. Khusaimi,^{1,2} M. H. Mamat,³ N. Abdullah,⁴ and M. Rusop^{1,3}

¹ NANO-SciTech Centre (NST), Institute of Science, Universiti Teknologi MARA (UiTM), 40450 Shah Alam, Selangor, Malaysia

² Faculty of Applied Sciences, Universiti Teknologi MARA (UiTM), 40450 Shah Alam, Selangor, Malaysia

³ NANO-Electronic Centre (NET), Faculty of Electrical Engineering, Universiti Teknologi MARA (UiTM), 40450 Shah Alam, Selangor, Selangor 40450 Shah Alam, Malaysia

⁴ Faculty of Science, Universiti Malaya, 55000 Kuala Lumpur, Malaysia

Correspondence should be addressed to Z. Khusaimi, zuraidakhusaimi@gmail.com

Received 11 April 2011; Revised 7 July 2011; Accepted 10 July 2011

Academic Editor: Parvaneh Sangpour

Copyright © 2012 Z. Khusaimi et al. This is an open access article distributed under the Creative Commons Attribution License, which permits unrestricted use, distribution, and reproduction in any medium, provided the original work is properly cited.

ZnO nanoparticles were prepared on Si substrates by a mist-atomisation technique. Precursor of aqueous solution zinc nitrate and HMTA were released on substrates heated at 200, 300, and 400°C confined in chamber box. The surface of Si substrate was varied, that is, gold-seeded Si (Si/Au), ZnO nanorods on Si/Au (Si/Au/ZnO), and just Si. The samples were subsequently analysed by X-ray diffraction, scanning electron microscopy, and photoluminescence (PL) spectroscopy to study their structural, surface morphology, and PL emission properties. Analysis from the XRD patterns of the films showed strong *a*- and *c*-axis lattice and of pure ZnO hexagonal wurtzite type. The crystallite size varied from 6 to 43 nm and was found to generally increase with increasing substrates' temperatures (T_s). SEM micrographs revealed granular-like structure throughout. Shifts pattern of PL emission at ultraviolet and visible range was found to support size changes observed. Both substrate surface type and deposition temperature were found to significantly affect crystalline growth of ZnO nanoparticles. Chemical equations and justification for growth patterns are also suggested.

1. Introduction

Zinc oxide (ZnO) is a very versatile material with a wide variety of usage (due to its properties such as white appearance, nontoxicity, antibacterial, polarity, and high thermal conductivity). ZnO is a thermally stable semiconducting metal oxide with wide energy band gap of 3.37 eV. In the field of electronics, some of its optoelectronic usages are as sensor, laser diode, light emitting diode (LED), and dye-synthesised solar cells. Nanostructured ZnO has been found to form various kinds of growth morphologies, like nanorods, nanowire, nanobelts, nanoflower, and tetrapods [1–3]. Synthesis of ZnO are carried out by many methods like chemical vapour deposition (CVD) [4, 5], pulsed laser deposition (PLD) [6, 7], magnetron sputtering [8], microwave irradiation [9, 10], hydrothermal [11], sol-gel [12], solution method [13] and also spray pyrolysis [14]. Mist-atomisation is a process similarly known as spray

pyrolysis. It is a physicochemical synthesis method used by advanced material researchers to produce thin film metal oxide nanostructures. Not restricted to metal oxides, this method may be used for production of simple oxides, binary, ternary oxides and superconducting oxides [15]. The process involves spraying precursor solution onto heated surface and the constituents react to form the intended products [16]. In this investigation, ZnO nanoparticles have been successfully grown by mist-atomisation deposition technique on Si substrate.

It was stipulated that besides concentration of precursor solution, deposition time and gas flow rate, temperature of the substrate significantly affects the final morphology and thickness of ZnO nanoparticles [15, 17]. A good quality nanostructured thin film is attainable by the formation of mist with small droplets and uniform distribution. In this investigation, by keeping the spraying rate constant, the temperature of substrate was varied at 200, 300, and 400°C

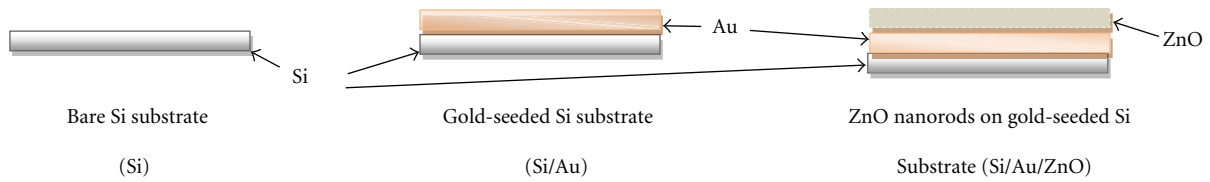


FIGURE 1: Type of surfaces used to deposit ZnO nanostructured thin films by mist-atomisation.

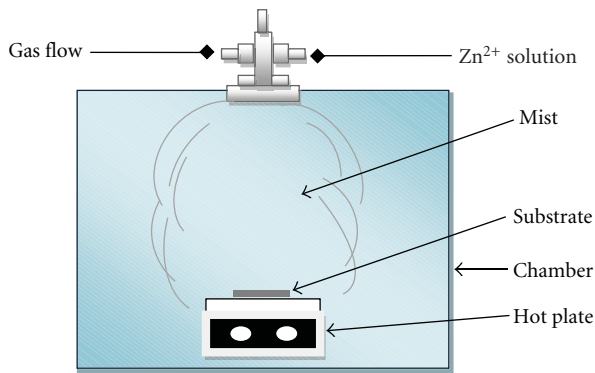


FIGURE 2: Schematic diagram of a mist-atomisation technique.

and deposited on Si substrate. It was also investigated if ZnO formed by mist-atomiser is sensitive to the type of surface of Si substrate, that is, bare polished Si (Si), gold-seeded Si substrate (Si/Au), and ZnO nanorods grown by immersion sol-gel method on gold-seeded Si substrate (Si/Au/ZnO) (Figure 1).

2. Experimental

ZnO nanoparticles were obtained by a mist-atomisation technique in air atmosphere. This cost-effective method is suitable to deposit large area of substrates with metal-oxide nanostructures at low temperature. The setup consisted of three components, that is, a steel pneumatic atomiser, hot-plate deposition surface, and our own designed acrylic chamber, $50 \times 50 \times 50 \text{ cm}^3$ (Figure 2). The distance of the atomiser to hot-plate surface is thus fixed at 39.5 cm. Temperature inside the chamber was measured using IR thermometer Brand Fluke 62 Mini IR and was detected to be approximately 30°C less than temperature of regulated substrate surface. The initial solution is zinc nitrate hexahydrate ($\text{Zn}(\text{NO}_3)_2 \cdot 6\text{H}_2\text{O}$) dissolved in deionised (DI) water and mixed with aqueous solution of hexamethylenetetramine ($\text{C}_6\text{H}_{12}\text{N}_4$) (HMTA) at 0.05 M concentration at 1 : 1 ratio. The precursor solution was released under high pressure through a tiny orifice with aspiration of atomic magnitude and subsequently contained as mists at ambient before it landed on the chosen substrates forming nanostructures of product. The growth was performed with a spray rate of 10 mL/min on three different types of Si substrate surfaces at three different hot-plate temperatures of (T_s) 200, 300, and 400°C with an accuracy of $\pm 5^\circ\text{C}$. The first surface is bare silicon (Si), the second surface is 6 nm of gold layer

on Si substrate (Si/Au), and the third surface is 1 μm ZnO nanorods on Si/Au (Si/Au/ZnO) (Figure 1). The preparation techniques for the substrates have been explained elsewhere [18]. The obtained films were dried and annealed at 600°C for 1 hour and showed good adhesion to the substrate surface.

Structural characterisation was carried out by X-ray diffraction (XRD) using Rigaku RINT 2200/Ultima IV, Cu $K\alpha$ radiation over the range $2\theta = 30\text{--}40^\circ$ at room temperature. The surface morphology was investigated using JEOL JSM-636 OLA scanning electron microscope (SEM). Photoluminescence (PL) measurement was performed on PL-Raman (Horiba Jobin Yvon) at room temperature using a He-Cd lamp with excitation wavelength 325 nm.

3. Result and Discussion

This simple method was carried out at ambient without the need of a vacuum rendering it suitable for large-scale industrial applications [19].

3.1. XRD. The XRD spectra on different substrate temperatures were presented in Figure 3. The results obtained were line-indexed with ZnO powder sample reported in JCPDS card no. 36-1451. All spectra showed strong prominent crystal diffraction planes of (100), (002), and (101) except for weak diffractions shown on Si/Au substrate at $T_s = 400^\circ\text{C}$. The observed diffractions are similar to those found in bulk ZnO.

ZnO prepared on Si (Figure 3(a)) at 400°C exhibited high domination of (002) lattice orientation showing preference of c-axis orientation. This occurrence has been established to be due to lowest surface energy according to Wulff's theorem [20]. The theory stated that the equilibrium of crystal formation was to achieve minimum total surface energy for a given volume. Lowest surface energies are represented by the largest crystal surfaces and interplanar distances.

The XRD spectra of ZnO on Si/Au (Figure 3(b)) exhibited extra lattice peaks belonging to gold (Au) peaks which are also noticeable at 33.096° and 38.215° . At 400°C , the intensity of lattice peaks of ZnO was completely reduced. The eutectic point of Au with Si substrates is 363°C [21]. Therefore, at this higher temperature of 400°C , the two solid of Au and Si coexist and may have caused the anomaly in the XRD pattern. This may also caused violent movements of Zn and O atoms led to improper growth of ZnO. However, the lattice ratio c/a remained the same of 1.601 at 200 and 400°C , and 1.602 at 300°C .

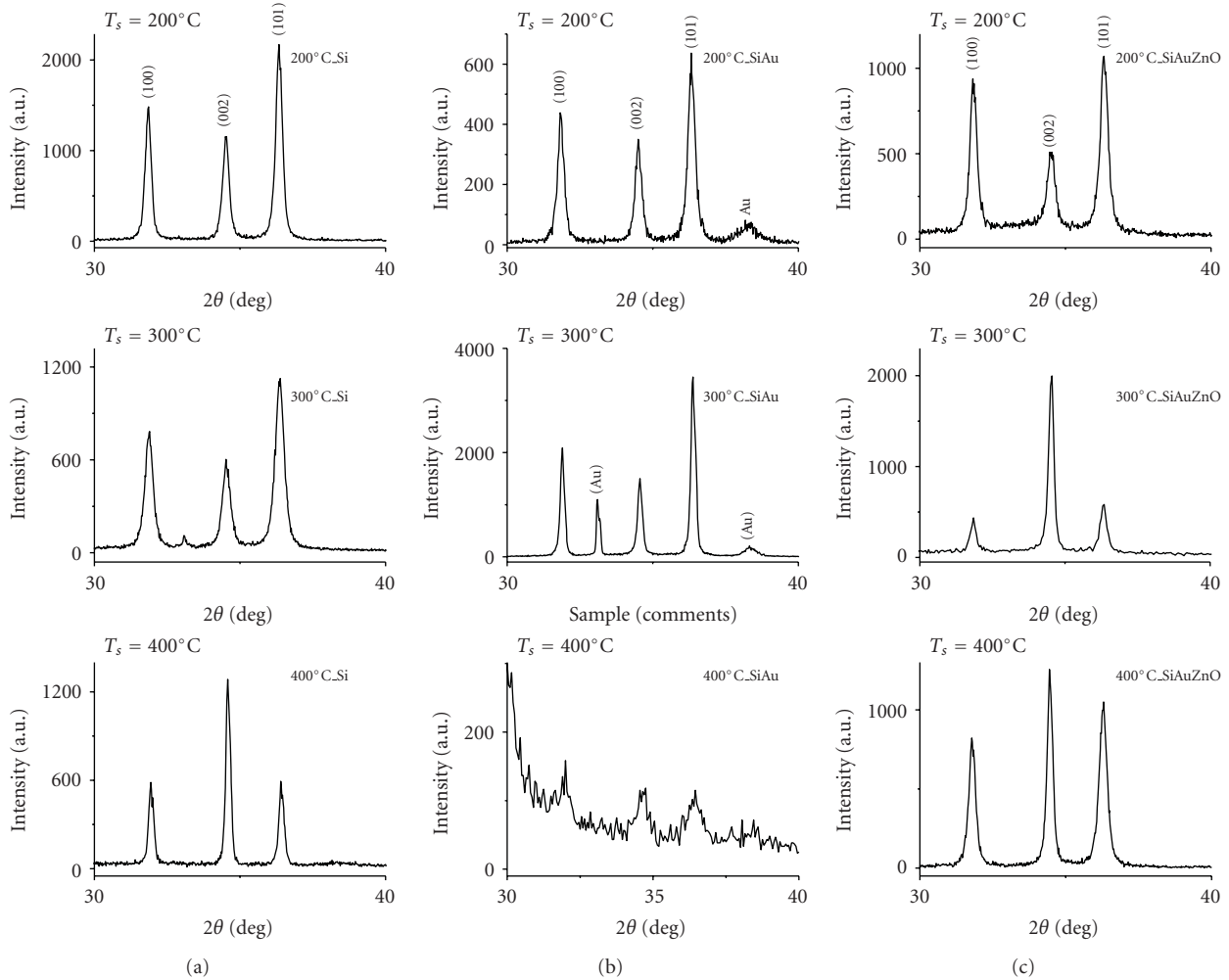


FIGURE 3: XRD data of ZnO nanoparticles deposited by mist-atomisation technique on (a) bare Si (b) gold-seeded Si (Si/Au) and (c) ZnO nanorods on gold-seeded Si substrate (Si/Au/ZnO), at substrate temperatures of 200, 300, and 400°C.

XRD pattern of ZnO grown on Si/Au/ZnO (Figure 3(c)) at $T_s = 300^\circ\text{C}$ revealed prominent (002) lattice which appear to provide the optimum substrate temperature to grow vertically aligned ZnO possibly. The combination of this temperature and types of surface has definitely favoured the movement and placement of Zn and O atoms into proper site.

Lattice constants a , c , lattice ratios c/a , crystallite size, and % strain obtained from the XRD data of all the samples are presented in Table 1. Crystallite sizes were calculated by Williamson-Hall method. The lattice values are found to be very close to hexagonal ZnO powder sample standard values of $a = 0.3249$ nm and $c = 0.5205$ nm [22], indicating that the material prepared is pure ZnO hexagonal wurtzite type structure. Crystallite size and % strain of all the prepared samples obtained from the analysis of XRD data [23], plotted as a function of temperature as shown in Figures 4(a) and 4(b).

Earlier works has shown that lattice parameters are temperature dependent. Expansion of lattice and particle size are in accordance with increase in temperature [24]. In this

work we found that crystallite size of ZnO nanoparticles increased as T_s increased for sample deposited on Si and Si/Au. Increment of particles size with increasing temperature of substrate has also been reported by other literature for semiconducting material by spray-pyrolysis methods [25, 26]. The increase in size may be caused by integration of smaller particles into larger particles as indicated by Ostwald's ripening, which resulted to be due to potential energy difference among large and small particles via solid state diffusion.

However, the crystallite size showed shrinkage at higher T_s of 400°C on Si/Au/ZnO substrate. The predeposited ZnO layer may have acted as an insulation layer resulting in similar effect to the thermal decomposition of the precursor droplets as it approaches the surface of substrates as those of lower T_s .

Upon calculation of % strain between ZnO nanoparticles to the substrate (Figure 4(b)), ZnO on Si/Au substrate matched excellently as it was strain-free and simultaneously produced the smallest crystallite size. The predeposited ZnO layers were made up of ZnO nanorods with (002) lattice orientation. Lattice matching is another factor for superior

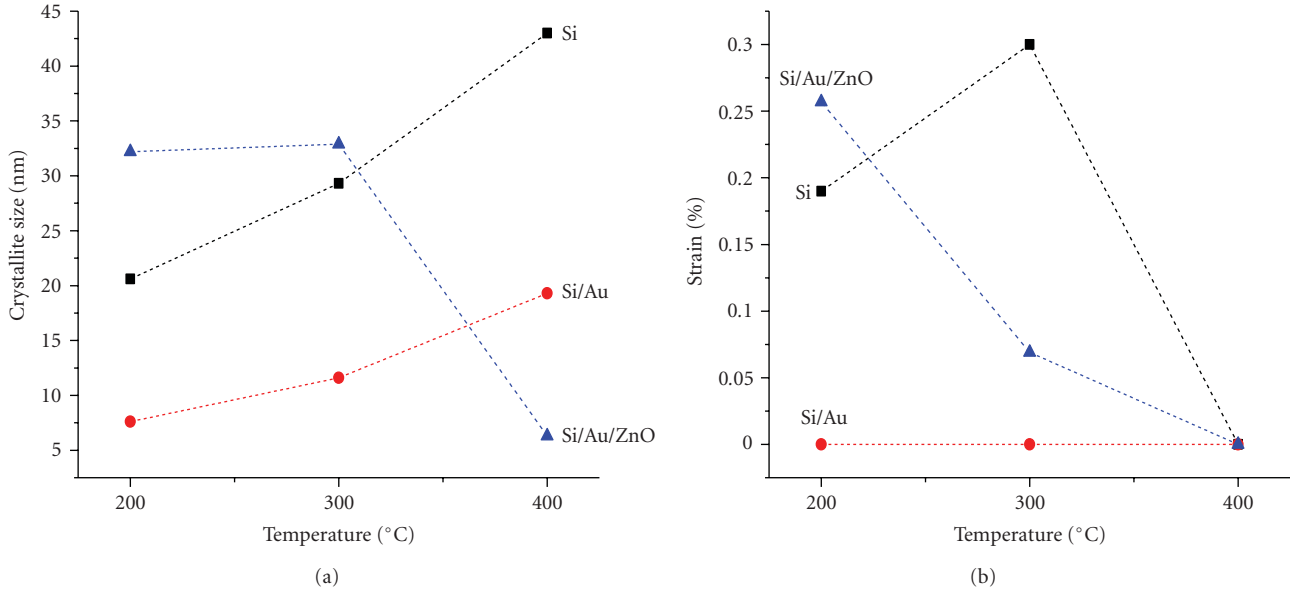


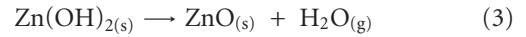
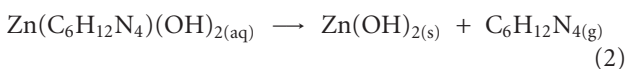
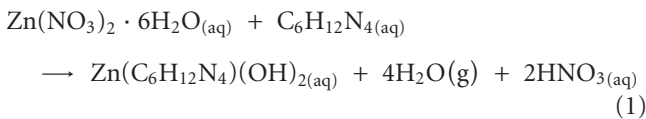
FIGURE 4: (a) Crystallite size, (b) % strain of ZnO on three types of Si surface plotted as a function of substrate temperature.

growth of ZnO on substrates. A study carried out by Li et al. [27] comparing growth of ZnO on Si (111) and (100) has shown that ZnO grown on Si (111) exhibited greater growth density of ZnO nanorods compared to on Si (100). Thus predeposited ZnO film with other lattice orientation should also be considered for further studies.

This result suggests that the assumption of compatibility is not limited to type of material but rather also on the crystal orientation of the material, and thus needs further investigations.

From the result, deposition of Zn^{2+} solution by mist-atomisation technique has proven to be capable of producing nanosized crystals of ZnO. Thermogravimetric analysis (TGA) of the precursor solution showed that it degraded at 160°C [18], thus at the chosen substrate temperature of 200°C and above, the precursor would have been dissociated as it reaches the surface of substrates [17]. (Temperature inside chamber has been described at experimental.) Optimum deposition condition may have been achieved since the solvent was completely removed just before the droplet reaches the substrate [15]. The surfaces of the substrates were of dissimilar temperatures therefore the chemical reaction may have taken place either prior to, throughout, or subsequent to the mists of precursors reach the surface of the substrate.

The chemical reaction that took place is as suggested in the equations below



It is suggested that zinc nitrate hexahydrate combined with HMTA molecule and formed a hydroxide complex (1). HMTA is an amine molecule which helped to chelate the Zn^{2+} ion [18] (2) and adsorbed on the sample and helped to determine growth morphology and irrelevant to the transition process [28]. The complex then dissociated into solid $Zn(OH)_2$ while HMTA vapourised. Upon heating, $Zn(OH)_2$ transform into ZnO and excess H_2O removed (3).

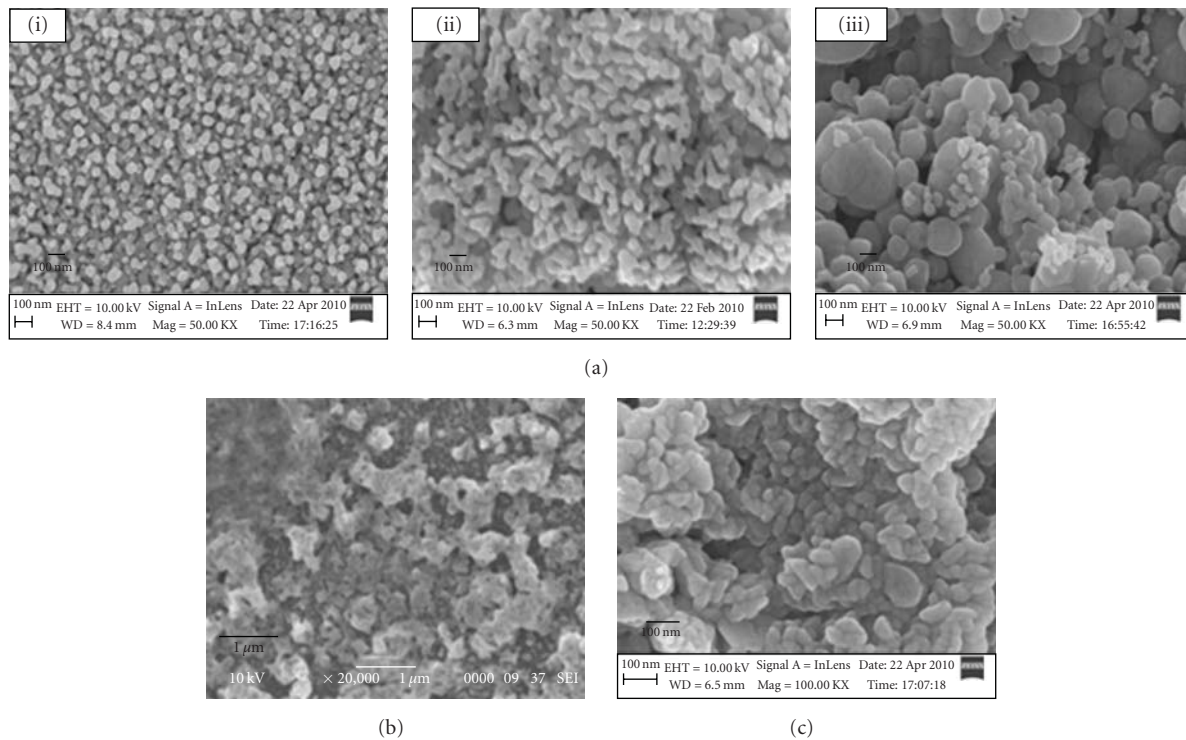
3.2. SEM. The surface morphology of deposited nanostructured ZnO was captured by SEM. The mist-atomiser deposition of ZnO produced nanogranular structure in the range of 50–120 nm in most samples. The granules are rounded grains which interconnect if remain heated.

Figure 5(a) (i)–(iii) show the SEM micrographs of ZnO deposited on Si at 200, 300, and 400°C. Thermal oxidation of Si substrate has been reported to occur at temperature higher than 400°C, for example, from 800°C thus the substrate surface may be safely assumed to remain inert at the selected substrate temperatures [29, 30]. It is clearly seen that with increasing substrates' temperature there is a tendency for the granules to interconnect as higher energy allows the grain boundary to expand and thus blend with other granules and form bigger grains. The interconnecting granules (50–120 nm) are also observed on samples deposited on Si/Au. This is thought to be due to the better efficiency of gold in conducting heat, having thermal conductivity of ~310 W/mK [31] relative to Si which is less than 200 W/mK [32]. For the same reason, ZnO deposited on Si/Au (Figure 5(b)) at 400°C showed bigger clusters of grains at ~200 nm with greater disbonded granular boundaries.

The predeposited ZnO layer may have acted as an insulation layer resulting in similar effect to the thermal

TABLE 1: Characteristics of ZnO nanostructured thin film from XRD analysis, grown on different Si substrate.

Type of surface	Bare Si (Si)		Gold-seeded Si (Si/Au)		ZnO nanorods on gold-seeded Si (Si/Au/ZnO)	
Substrate temperature (°C)	Lattice constant (Å) and c/a ratio	Crystallite size (nm) and % strain	Lattice constant (Å) and c/a ratio	Crystallite size (nm) and % strain	Lattice constant (Å) and c/a ratio	Crystallite size (nm) and % strain
200	$a = 3.244$ $c = 5.199$ $c/a = 1.603$	20.6 0.109	$a = 3.246$ $c = 5.196$ $c/a = 1.601$	7.6 0	$a = 3.246$ $c = 5.103$ $c/a = 1.572$	32.2 0.257
300	$a = 3.242$ $c = 5.196$ $c/a = 1.603$	29.3 0.300	$a = 3.243$ $c = 5.195$ $c/a = 1.602$	11.6 0	$a = 3.246$ $c = 5.193$ $c/a = 1.600$	32.9 0.069
400	$a = 3.245$ $c = 5.202$ $c/a = 1.603$	43.0 0	$a = 3.444$ $c = 5.517$ $c/a = 1.601$	19.3 0	$a = 3.247$ $c = 5.202$ $c/a = 1.602$	6.34 0

FIGURE 5: SEM micrographs ZnO nanoparticles deposited by mist-atomisation technique on (a) Si at substrate temperatures (T_s) of (i) 200, (ii) 300, (iii) 400°C, (b) Si/Au substrate at $T_s = 400^\circ\text{C}$ and (c) Si/Au/ZnO at $T_s = 400^\circ\text{C}$.

decomposition of the precursor droplets as it approaches the surface of substrates as those of lower T_s .

The effect of heat to ZnO nanoparticles on Si/Au/ZnO was different compared to those on Si and Si/Au substrates. Heating at 400°C has not caused the expansion of the grain boundaries for the reason that ZnO has thermal conductivity value of less than 2 W/mK [33], therefore the effect of 400°C was not as intense as it was on Si or Si/Au substrates. Heat transport phenomena upon reduction of particles size, phonon modes, and phonon densities need to be carried out in a separate investigation as it proved to be a very interesting and important technological area [34].

3.3. Photoluminescence Emission. Figure 6(a) illustrated the room-temperature PL spectra (excitation at 325 nm) of the samples deposited on Si at 200, 300, and 400°C, Figure 6(b) on sample deposited on Si/Au and Figure 6(c) on sample deposited on Si/Au/ZnO. Two emission bands could be observed from these samples, that is, (i) near band edge emission (at ultraviolet (UV) range) due to free-exciton recombination and (ii) visible emission, a deep-level-emission (DLE) mostly in yellow-orange region was a consequence of presence of structural defect and impurities on the surface of samples [35–37]. Visible peaks at yellow-orange emission band around 580 nm were generally emitted

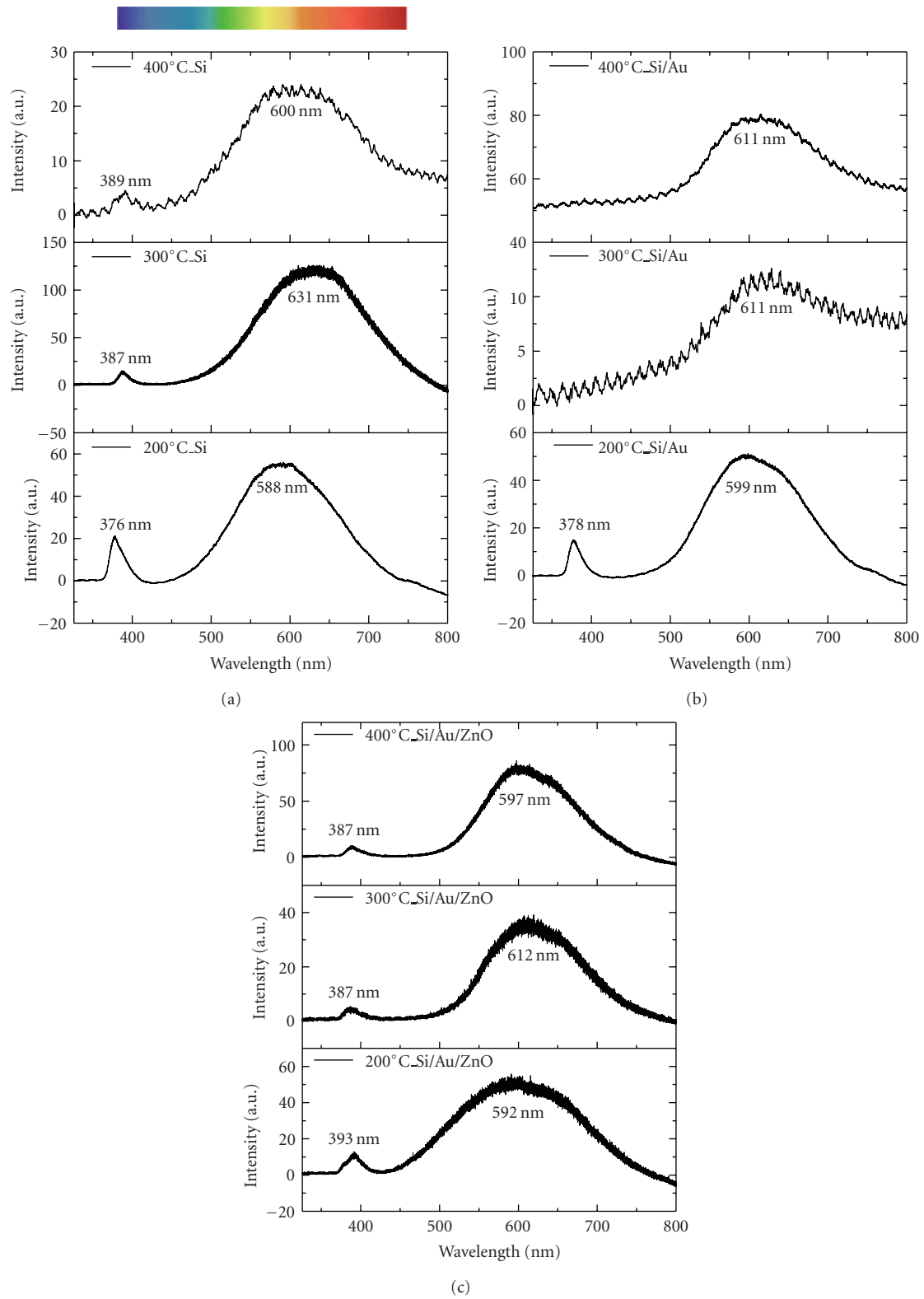


FIGURE 6: PL spectra of ZnO nanocrystalline thin film prepared by mist-atomisation technique on substrate (a) Si, (b) Si/Au, and (c) Si/Au/ZnO at 200, 300, and 400°C.

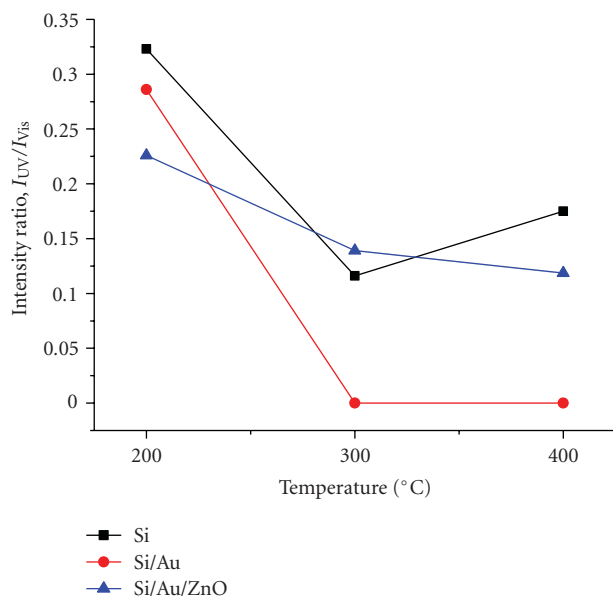


FIGURE 7: Intensity ratio of UV to visible emission (I_{UV}/I_{Vis}) at various substrates' temperature and on various types of Si substrate surfaces.

by all samples. This band is common among solution-based grown ZnO, and has been considered to be due to oxygen interstitial (O_i) related defects [38], that is, excess oxygen and presence of hydroxyl group and is related to the amount of exposed polar surface of Zn- and O-atom [39].

The UV emission of ZnO nanostructures deposited on Si and Si/Au substrate on dissimilar temperatures showed a red-shift, that is, to a lower energy when the substrates' temperature changed from 200 to 400°C. The result was consistent with the XRD, SEM findings, which revealed that the grain size were smallest at 200°C and expanded when the temperature of substrate increased [23, 40, 41]. The UV emission peaks of ZnO deposited on Si/Au/ZnO blue-shifted with increased substrates' temperature, showing coherent findings that as size decreases UV emission moved to higher energy level. An almost negligible UV emission can be seen for sample deposited on Si/Au substrates at 300 and 400°C which some attribute to excess -OH group that is responsible for quenching of the exciton emission [39]. The -OH group may have originated from solvent trapped in empty octahedral site in the hexagonal lattice structure of ZnO.

The ratio of the intensities of UV to visible emission (I_{UV}/I_{Vis}) as a function of substrate's temperature (Figure 7) was also analysed. It can be seen that prominent ratios are found on $T_s = 200^\circ\text{C}$ for all samples while bare Si surface has higher I_{UV}/I_{Vis} ratio relative to Si/Au and Si/Au/ZnO.

4. Conclusion

Mist-atomiser has been successfully developed to prepare ZnO nanoparticles. This technique is economical, simple, and practical for mass-production purposes of ZnO thin

films. Effects of Si substrates' surface type and substrates temperature, on the structural, morphological, and photoluminescence emission of ZnO nanoparticles have been investigated. X-ray diffraction patterns confirmed that all samples showed that polycrystalline nature corresponds to ZnO wurtzite structure. It was found that crystallite size and lattice strain were significantly affected by substrate surface type and temperature. Smallest crystallite size was found on Si/Au/ZnO at $T_s = 400^\circ\text{C}$, gold layer on substrate revealed no lattice strain at all deposition temperatures and at $T_s = 400^\circ\text{C}$ there was negligible strain on all substrates. PL emission study was in agreement with the expansion of crystallite size study. The chemical reaction that took place has been suggested as well as explanation for growth outcome. Both substrate surface type and deposition temperature has been found to significantly affect crystalline structure of ZnO nanoparticles.

Acknowledgments

The author would like to thank Universiti Teknologi MARA (UiTM) and Jabatan Perkhidmatan Awam (JPA) Malaysia for the financial support. The author also thanks Microwave Technology Centre (MTC), Faculty of Electrical Engineering, Faculty of Mechanical engineering and Faculty of Applied Sciences for SEM and XRD facilities.

References

- [1] T. Terasako, M. Yagi, M. Ishizaki, Y. Senda, H. Matsuura, and S. Shirakata, "Growth of zinc oxide films and nanowires by atmospheric-pressure chemical vapor deposition using zinc powder and water as source materials," *Surface and Coatings Technology*, vol. 201, no. 22-23, pp. 8924–8930, 2007.
- [2] M. H. Mamat, Z. Khusaimi, M. Z. Musa, M. Z. Sahdan, and M. Rusop, "Novel synthesis of aligned Zinc oxide nanorods on a glass substrate by sonicated sol-gel immersion," *Materials Letters*, vol. 64, no. 10, pp. 1211–1214, 2010.
- [3] J. G. Lu, P. Chang, and Z. Fan, "Quasi-one-dimensional metal oxide materials—synthesis, properties and applications," *Materials Science and Engineering R*, vol. 52, pp. 49–91, 2006.
- [4] X. Liu, X. Wu, H. Cao, and R. P. H. Chang, "Growth mechanism and properties of ZnO nanorods synthesized by plasma-enhanced chemical vapor deposition," *Journal of Applied Physics*, vol. 95, no. 6, pp. 3141–3147, 2004.
- [5] M. Salavati-Niasari, F. Davar, and M. Mazaheri, "Preparation of ZnO nanoparticles from [bis(acetylacetonato)zinc(II)]-oleylamine complex by thermal decomposition," *Materials Letters*, vol. 62, no. 12-13, pp. 1890–1892, 2008.
- [6] M. Rusop, K. Uma, T. Soga, and T. Jimbo, "Post-growth annealing of zinc oxide thin films pulsed laser deposited under enhanced oxygen pressure on quartz and silicon substrates," *Materials Science and Engineering B*, vol. 127, no. 2-3, pp. 150–153, 2006.
- [7] E. T. Y. Lee, Y. Shimotsu, M. Sakakura, M. Nishi, K. Miura, and K. Hirao, "Photo-initiated growth of zinc oxide (ZnO) nanorods," *Materials Letters*, vol. 62, no. 24, pp. 4044–4046, 2008.

- [8] G. J. Fang, D. Li, and B.-L. Yao, "Influence of post-deposition annealing on the properties of transparent conductive nanocrystalline ZAO thin films prepared by RF magnetron sputtering with highly conductive ceramic target," *Thin Solid Films*, vol. 418, no. 2, pp. 156–162, 2002.
- [9] M.-G. Ma, Y.-J. Zhu, G.-F. Cheng, and Y.-H. Huang, "Microwave synthesis and characterization of ZnO with various morphologies," *Materials Letters*, vol. 62, no. 3, pp. 507–510, 2008.
- [10] Y. Du, C. Hao, and G. Wang, "Preparation of floral-patterned ZnO/MWCNT heterogeneity structure using microwave irradiation heating method," *Materials Letters*, vol. 62, no. 1, pp. 30–32, 2008.
- [11] J. H. Yang, J. H. Zheng, H. J. Zhai, and L. L. Yang, "Low temperature hydrothermal growth and optical properties of ZnO nanorods," *Crystal Research and Technology*, vol. 44, no. 1, pp. 87–91, 2009.
- [12] M. S. Ghamsari and M. Vafaei, "Sol-gel derived zinc oxide buffer layer for use in random laser media," *Materials Letters*, vol. 62, no. 12–13, pp. 1754–1756, 2008.
- [13] Z. Khusaimi, S. Amizam, H. A. Rafeie et al., "Photoluminescence and structural properties of gold-assisted zinc oxide nanorods," *The Malaysian Journal of Science*, vol. 28, pp. 197–201, 2009.
- [14] A. Mosbah, A. Moustaghfir, S. Abed et al., "Comparison of the structural and optical properties of zinc oxide thin films deposited by d.c. and r.f. sputtering and spray pyrolysis," *Surface and Coatings Technology*, vol. 200, pp. 293–296, 2005.
- [15] P. S. Patil, "Versatility of chemical spray pyrolysis technique," *Materials Chemistry and Physics*, vol. 59, no. 3, pp. 185–198, 1999.
- [16] J. B. Mooney and S. B. Radding, "Spray pyrolysis processing," *Annual Review of Materials Science*, vol. 12, pp. 81–101, 1982.
- [17] K. Okuyama and I. W. Lenggoro, "Preparation of nanoparticles via spray route," *Chemical Engineering Science*, vol. 58, pp. 537–547, 2003.
- [18] Z. Khusaimi, S. Amizam, M. H. Mamat et al., "Controlled growth of zinc oxide nanorods by aqueous-solution method," *Synthesis and Reactivity in Inorganic, Metal-Organic and Nano-Metal Chemistry*, vol. 40, no. 3, pp. 190–194, 2010.
- [19] P. Singh, A. Kumar, Deepak, and D. Kaur, "Growth and characterization of ZnO nanocrystalline thin films and nanopowder via low-cost ultrasonic spray pyrolysis," *Journal of Crystal Growth*, vol. 306, no. 2, pp. 303–310, 2007.
- [20] J. Prywer, "Kinetic and geometric determination of the growth morphology of bulk crystals: recent developments," *Progress in Crystal Growth and Characterization of Materials*, vol. 50, pp. 1–38, 2005.
- [21] S.-Y. Pung, K.-L. Choy, and X. Hou, "Tip-growth mode and base-growth mode of Au-catalyzed zinc oxide nanowires using chemical vapor deposition technique," *Journal of Crystal Growth*, vol. 312, no. 14, pp. 2049–2055, 2010.
- [22] B. Joseph, K. G. Gopchandran, P. V. Thomas, P. Koshy, and V. K. Vaidyan, "A study on the chemical spray deposition of zinc oxide thin films and their structural and electrical properties," *Materials Chemistry and Physics*, vol. 58, no. 1, pp. 71–77, 1999.
- [23] M. Ghosh and A. K. Raychaudhuri, "Shape transition in ZnO nanostructures and its effect on blue-green photoluminescence," *Nanotechnology*, vol. 19, no. 44, Article ID 445704, 2008.
- [24] V. Ramaswamy, P. Awati, and A. K. Tyagi, "Lattice thermal expansion of $\text{LaCo}_{1-x}\text{Cu}_x\text{O}_3$," *Journal of Alloys and Compounds*, vol. 364, no. 1–2, pp. 180–185, 2004.
- [25] A. Ashour, "Physical properties of spray pyrolysed CdS thin films," *The Turkish Journal of Physics*, vol. 27, no. 6, pp. 551–558, 2003.
- [26] P. Singh, A. Kumar, Deepak, and D. Kaur, "ZnO nanocrystalline powder synthesized by ultrasonic mist-chemical vapour deposition," *Journal of Crystal Growth*, vol. 306, pp. 303–310, 2008.
- [27] Y. J. Li, R. Duan, P. B. Shi, and G. G. Qin, "Synthesis of ZnO nanoparticles on Si substrates using a ZnS source," *Journal of Crystal Growth*, vol. 260, no. 3–4, pp. 309–315, 2004.
- [28] R. Maity, S. Das, M. K. Mitra, and K. K. Chattopadhyay, "Synthesis and characterization of ZnO nano/microfibers thin films by catalyst free solution route," *Physica E*, vol. 25, no. 4, pp. 605–612, 2005.
- [29] Y. Takakuwa, F. Ishida, and T. Kawawa, "Time evolution of interface roughness during thermal oxidation on $\text{Si}(0\ 0\ 1)$," *Applied Surface Science*, vol. 190, pp. 20–25, 2002.
- [30] A. Omura, H. Sekikawa, and T. Hattori, "Lateral size of atomically flat oxidized region on $\text{Si}(111)$ surface," *Applied Surface Science*, vol. 117–118, pp. 127–130, 1997.
- [31] B. Feng, Z. Li, and X. Zhang, "Prediction of size effect on thermal conductivity of nanoscale metallic films," *Thin Solid Films*, vol. 517, no. 8, pp. 2803–2807, 2009.
- [32] K. Kakimoto, A. Murakawa, and Y. Hashimoto, "An investigation of thermal conductivity of isotope silicon as a function of temperature estimated by molecular dynamics," *Journal of Crystal Growth*, vol. 275, no. 1–2, pp. e427–e432, 2005.
- [33] C. M. Barrado, E. R. Leite, P. R. Bueno, E. Longo, and J. A. Varela, "Thermal conductivity features of ZnO-based varistors using the laser-pulse method," *Materials Science and Engineering A*, vol. 371, no. 1–2, pp. 377–381, 2004.
- [34] Z. L. Wang, "Zinc oxide nanostructures: growth, properties and applications," *Journal of Physics Condensed Matter*, vol. 16, no. 25, pp. R829–R858, 2004.
- [35] L. Schmidt-Mende and J. L. MacManus-Driscoll, "ZnO—nanostructures, defects, and devices," *Materials Today*, vol. 10, no. 5, pp. 40–48, 2007.
- [36] C. Chandrinou, N. Boukos, C. Stogios, and A. Travlos, "PL study of oxygen defect formation in ZnO nanorods," *Microelectronics Journal*, vol. 40, no. 2, pp. 296–298, 2009.
- [37] Y. Sun, N. G. Ndifor-Angwafor, D. J. Riley, and M. N. R. Ashfold, "Synthesis and photoluminescence of ultra-thin ZnO nanowire/nanotube arrays formed by hydrothermal growth," *Chemical Physics Letters*, vol. 431, pp. 352–357, 2006.
- [38] S. S. Kurbanov, G. N. Panin, T. W. Kim, and T. W. Kang, "Strong violet luminescence from ZnO nanocrystals grown by the low-temperature chemical solution deposition," *Journal of Luminescence*, vol. 129, no. 9, pp. 1099–1104, 2009.
- [39] A. B. Djuriić, A. M. C. Ng, and X. Y. Chen, "ZnO nanostructures for optoelectronics: material properties and device applications," *Progress in Quantum Electronics*, vol. 34, no. 4, pp. 191–259, 2010.
- [40] J. Yang, M. Gao, Y. Zhang et al., "Effects of annealing temperature on morphologies and optical properties of ZnO nanostructures," *Superlattices and Microstructures*, vol. 44, no. 2, pp. 137–142, 2008.
- [41] G. N. Karanikolos, P. Alexandridis, G. Itskos, A. Petrou, and T. J. Mountziaris, "Synthesis and size control of luminescent ZnSe nanocrystals by a microemulsion-gas contacting technique," *Langmuir*, vol. 20, no. 3, pp. 550–553, 2004.

Research Article

Fabrication of Photofunctional Nanoporous Membrane and Its Photoinactivation Effect of Vesicular Stomatitis Virus

Kang-Kyun Wang,¹ Bong-Jin Kim,¹ Si-Hwan Ko,² Dong Hoon Choi,³ and Yong-Rok Kim¹

¹ Department of Chemistry, Yonsei University, Shinchon-Dong 134, Seodaemun-Gu, Seoul 120 749, Republic of Korea

² Department of Microbiology, College of Medicine, Yonsei University, Seoul 120 752, Republic of Korea

³ Cardiology Division, Cardiovascular Center, College of Medicine, Yonsei University, Seoul 120 752, Republic of Korea

Correspondence should be addressed to Yong-Rok Kim, yrkim@yonsei.ac.kr

Received 29 May 2011; Accepted 11 July 2011

Academic Editor: Amir Kajbafvala

Copyright © 2012 Kang-Kyun Wang et al. This is an open access article distributed under the Creative Commons Attribution License, which permits unrestricted use, distribution, and reproduction in any medium, provided the original work is properly cited.

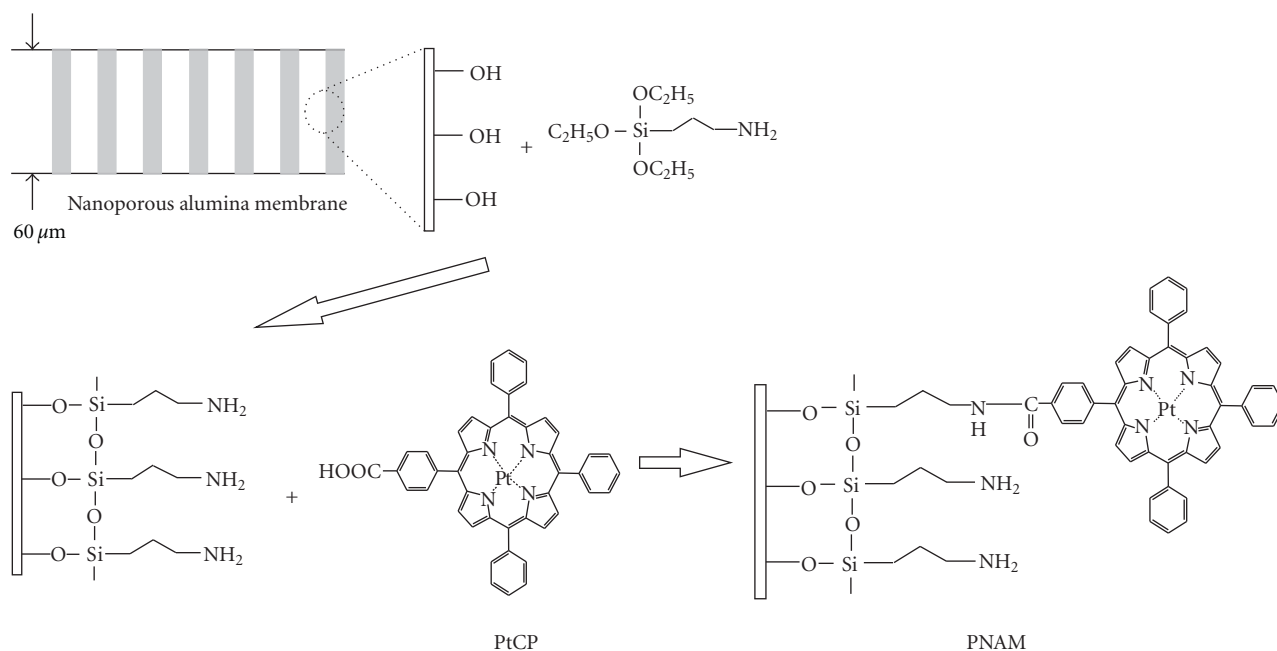
Fabrication and photophysical study of photofunctional nanoporous alumina membrane (PNAM) were performed, and its application of photodynamic antimicrobial chemotherapy (PACT) was investigated. Nanoporous alumina membrane (NAM) was fabricated by two-step aluminium anodic oxidation process. Surface of the fabricated NAM was modified with organo-silane agent to induce covalent bonding between NAM and a photosensitizer (PtCP: [5,10,15-triphenyl-20-(4-methoxycarbonylphenyl)-porphyrin] platinum). PtCP was covalently bonded to the surface of the modified NAM by nucleophilic acyl substitution reaction process. The morphology and the photophysical properties of the fabricated PNAM were confirmed with field emission scanning electron microscope (FE-SEM), steady-state spectroscopies, and nanosecond laser-induced time-resolved spectroscopy. For the efficacy study of PNAM in PACT, an enveloped animal virus, vesicular stomatitis virus (VSV), was utilized as a target organism. Antiviral effect of the PNAM-PACT was measured by the extent of suppression of plaque-forming units (PFU) after the light irradiation. In the cultures inoculated with PACT-treated VSV, the suppression of PFU was prominent, which demonstrates that PNAM is a potential bio clean-up tool.

1. Introduction

Reactive oxygen species (ROS) have been a subject of the extensive studies due to their broad applications such as photodynamic therapy (PDT), photovoltaic device, light harvest coating, and photocatalyst [1, 2]. Recently, the application area of ROS has been expanded into elimination of environmental pollutants such as toxic chemicals, endocrine disruptors, virus, and bacteria [3, 4]. The environmental applications require the high efficiency of ROS generation along with repeatability, the prevention of secondary contamination, and the easy recycling. In order to meet some of these factors, ROS generation of mesoporous materials has been demonstrated with zeolite and MCM-41 functionalized with photosensitizers [5]. By the fixation of photosensitizers onto zeolite or MCM-41, thermal stability and handling advantage could be achieved. However, both porous materials have a powder like property and a few

nanometers of very small pore diameter which disturbs the good contact between the ROS and the target systems [6]. However, the nanoporous membranes can provide the good contacts between the ROS and the target, and the easy handling advantage and recycling together due to their advantages of pore diameter control, unidirectional ordered pore direction, and free-standing nature of membrane.

In this work, we report a fabrication of the photofunctional nanoporous alumina membrane (PNAM) and its photophysical property. The nanoporous alumina membranes were fabricated by two-step aluminum anodic oxidation process [7]. The inner and the outer surfaces of the fabricated NAMs were modified with organo-silane agent [8–11]. The photosensitizer (PtCP: [5,10,15-triphenyl-20-(4-methoxycarbonylphenyl)-porphyrin] platinum) was covalently bonded to the amine-terminated NAM surface by a nucleophilic acyl substitution reaction [12]. The singlet oxygen, an active component of the ROS generated from the



SCHEME 1: Preparation of photofunctional nanoporous alumina membrane.

fabricated PNAM, was directly monitored with laser-induced time-resolved spectroscopic method. To open the possibility for its environmental application, PNAM was applied for the removal of a virus without rendering cytotoxicity to the cells *in vitro*. It resulted in the complete suppression of plaque forming ability of vesicular stomatitis virus (VSV) by PNAM-mediated PACT (photodynamic antimicrobial chemotherapy).

2. Experiment

2.1. Materials. The fabrication procedure of the PNAM is shown in Scheme 1. Preparation details of the photosensitizer (PtCP: [5,10,15-Triphenyl-20-(4-methoxycarbonyl-phenyl)-porphyrin] platinum) and the nanoporous alumina membrane (NAM) were reported in the references [7, 13]. All solvents were purchased from Aldrich and used without further purification. For the surface modification of NAM, NAM was immersed into the APTES ((aminopropyl)triethoxysilane, 0.1 M)/CHCl₃ solution at room temperature for 1 h [8–11]. After washing and drying, the surface-modified NAM was immersed in PtCP (10⁻⁵ M)/toluene at 50°C for 24 h and then washed with pure toluene and distilled water.

2.2. Methods

2.2.1. Spectroscopic Measurements. Surface morphologies of NAMs were observed by a field emission scanning electron microscopy (FESEM, JEOL, 6500F). Surfaces of the modified NAM and the fabricated PNAM were confirmed by ATR-IR spectra with a ATR-IR spectrophotometer (Nicolet, impact 400). Steady-state absorption and luminescence spectra were

obtained by using a UV-Vis spectrophotometer (Hitachi, U-2800) and a spectrofluorimeter (Hitachi, F-4500), respectively. For the membrane sample, the diffuse reflectance spectra were recorded by a UV-Vis spectrophotometer (Jasco, V-550) equipped with an integrating sphere (Jasco, ISV-469). The Nd-YAG-pumped OPO laser (BMI, OP-901, 10 Hz, 5 ns FWHM pulse) was utilized as an excitation source for the detection of time-resolved singlet oxygen phosphorescence. The phosphorescence signal was collected at the perpendicular angle to the excitation beam and detected with a monochromator (Optometrics LLC, mini-chrom04) and NIR-PMT (Hamamatsu, H9170-45). The signal was acquired by 500 MHz digital oscilloscope and transferred to a computer for further analysis [13, 14].

2.2.2. Biological Activity

General. The established cell lines of A549, Vero, and vesicular stomatitis virus (VSV, Indiana serotype) were originally purchased from ATCC (Rockford, Md, USA) and have been maintained at -70°C and 1 atm. For the evaluation of the efficacy with PNAM-mediated PACT on viral inactivation, A549 cells were used throughout the experiments. For viral preparation, VSV was propagated in Vero cells. Both the cell lines were maintained in Eagle's minimal essential medium (MEM) supplemented with 10% fetal bovine serum (both supplied by Gibco RBL, Grand Island, NY, USA), penicillin (100 units/mL), and streptomycin (100 μg/mL). The viral suspension free from the host cell debris was ultracentrifuged at 100,000 g for 2 h at 4°C (Beckman, Calif, USA). After centrifuging, protein content of the VSV pellet was determined by using the Bio-Rad protein assay (Bio-Rad Laboratories, Alfred Nobel Drive, Hercules, Calif, USA). The A549 cell grown in MEM was used as a host cell

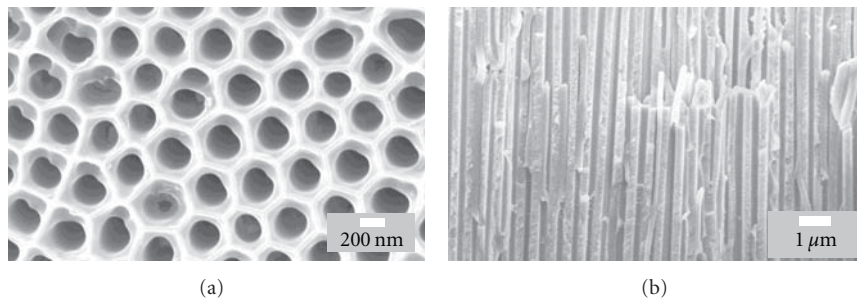


FIGURE 1: FE-SEM images of (a) the top surface view of nanoporous alumina membrane with the pore diameter of 250 nm and (b) its cross-section view.

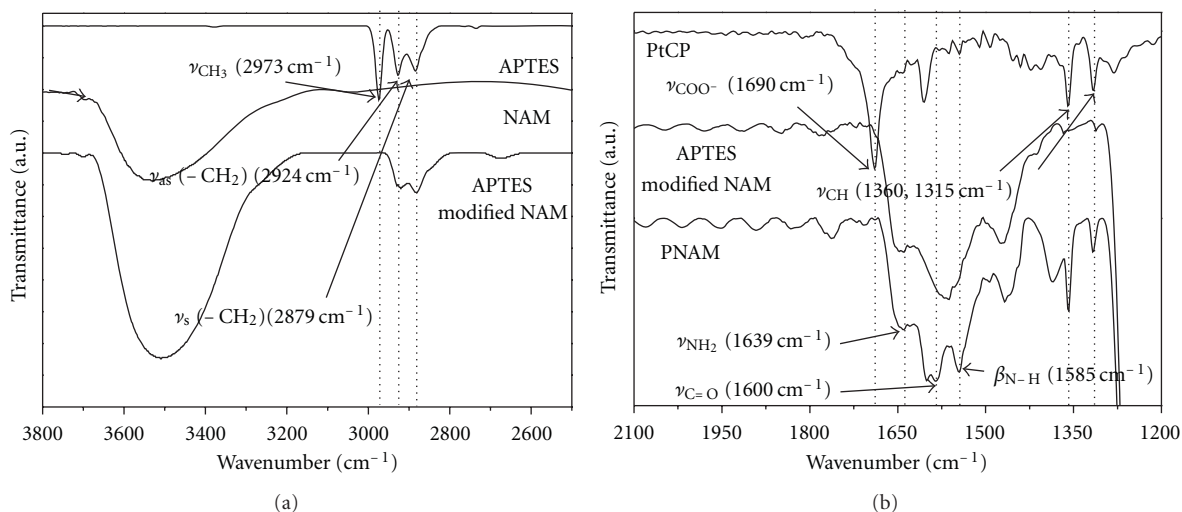


FIGURE 2: ATR-IR spectra of (a) pure NAM, pure APTES, and the surface modified NAM with APTES, (b) pure PtCP, pure PNAM, and the surface modified NAM with APTES.

for various assays. The light source for irradiation was a nanosecond Nd-YAG-pumped OPO laser (BMI, OP-901, 10 Hz, 5 ns FWHM pulse). The total power output for the irradiation was measured with a laser power meter (Ophir opironics Ltd., Nova, Israel). Virus in suspension (1 mL in a 1×1 quartz cell) was treated by PNAM irradiated with 5mWof light for 1 hr. The virus solution treated with photo-irradiated PNAM was kept in dark in order to protect the samples from ambient light exposure. All experiments were performed under the light-controlled condition in a biosafety box.

Plaque-Forming Assay. For a plaque-forming assay, A549 cells were seeded (2×10^5) in 6-well tissue culture plates in the growth media and allowed to form a confluent monolayer. All viruses that were treated with light only, PNAM only, and the irradiated PNAM in 1 mL of the solutions were inoculated into the cells and allowed to attach to the cells by rocking randomly for 1 h at 37°C under 5% CO_2 humidified atmosphere. For a negative control, the cells treated with a phosphate-buffered saline (PBS) were used to assure the viability of the cells. The culture fluid was removed by aspiration and washed twice with MEM. Each well was

overlaid with 2 mL of a mixture of 2% agarose and $2 \times \text{MEM}$ (1 : 1) and then incubated for 48 h at 37°C under 5% CO_2 -humidified atmosphere. Thereafter, the cells were rinsed by PBS and fixed in 2% paraformaldehyde for 15 min. These were then rinsed twice with PBS for staining with crystal violet. The titers of virus were estimated by use of the plaque-forming assay [15]. Statistical evaluation was done by using the Mann-Whitney U test. Results were presented as the means \pm the standard errors of the means (SEMs).

3. Results and Discussion

SEM images of the fabricated pure NAM are shown in Figure 1. The pore diameter of nanochannels is controlled to be 250 nm by the electrolyte solution of 0.3 M H_3PO_4 at the applied voltage of 40 V. Thickness of NAM is made to be $60 \mu\text{m}$ after the oxidation time of 10 hours. NAM is prepared as a free-standing film [7].

The surface modification of NAM with hydrophobic silane, APTES, and PtCP are confirmed with ATR-IR spectra. Figure 2(a) shows ATR-IR spectra of APTES, NAM, and the APTES-bounded NAM. The peaks of APTES in the spectrum are assigned to be the $-\text{CH}_3$ symmetric vibration

mode at 2973 cm^{-1} , the $-\text{CH}_2$ symmetric and asymmetric vibration modes at 2879 and 2924 cm^{-1} , respectively, from the references [8, 16]. The spectrum of NAM shows the $-\text{OH}$ stretching vibration modes at 3400 cm^{-1} [8, 9]. In the spectrum of the APTES bounded NAM, the peaks of the $-\text{CH}_2$ symmetric (2879 cm^{-1}) and asymmetric vibration modes (2924 cm^{-1}) remain same as the peaks of pure APTES. On the other hand, the $-\text{CH}_3$ (2973 cm^{-1}) vibration peak disappears significantly in its intensity. It is due to the removal step of the methyl group ($-\text{CH}_3$) of APTES during the attachment reaction process of APTES and NAM [11, 16, 17]. The increased peak intensity of the $-\text{OH}$ ($3650\sim 3200\text{ cm}^{-1}$) stretching vibration in Figure 2(a) implies that the hydroxyl group of the NAM surface is enhanced throughout the surface modification process. Therefore, the result confirms that the APTES is attached to the NAM surface by the silanisation reaction between the hydroxyl group of NAM and the ethoxy group of APTES. Figure 2(b) shows ATR-IR spectra of the surface modified NAM with APTES, PtCP, and the PtCP bounded surface modified NAM (PNAM). The peaks of PtCP in the spectrum are assigned to be the carbonyl stretching mode of the carboxyl group at 1690 cm^{-1} , the stretching vibration mode of the conjugated $\text{C}=\text{C}$ bond at 1605 cm^{-1} , and the $\text{C}-\text{H}$ stretching vibration mode at $1360, 1315\text{ cm}^{-1}$ from the references [18–20]. The spectrum of the surface modified NAM shows the stretching vibration mode of $-\text{NH}_2$ group at 1639 cm^{-1} [21, 22]. In the spectrum of the PtCP-bounded surface modified NAM, the peaks of the stretching vibration mode of $\text{C}=\text{C}$ (1605 cm^{-1}), and the stretching vibration modes of $\text{C}-\text{H}$ ($1360, 1315\text{ cm}^{-1}$) remain same. On the other hand, the carbonyl (1690 cm^{-1}) stretching mode peak disappears significantly in its intensity. And the $\text{C}=\text{O}$ stretching mode and the $\text{N}-\text{H}$ bending mode of new amide group are appeared at the $1600, 1585\text{ cm}^{-1}$, respectively. It is due to the removal step of the carboxylic acid group ($-\text{COOH}$) of PtCP during the nucleophilic acyl substitution reaction process of PtCP and the surface modified NAM [12]. The appeared peaks of the $\text{C}=\text{O}$ and the $\text{N}-\text{H}$ ($1600, 1585\text{ cm}^{-1}$) stretching vibration imply that the amide group of the modified NAM surface is enhanced throughout the surface modification process. Therefore, IR data in Figure 2 confirms that PtCP is covalently bonded to the modified NAM surface by the nucleophilic acylation reaction between the carboxylic acid group of PtCP and the amine group of APTES [12].

Diffuse reflectance UV-Vis absorption spectrum of PNAM is presented in Figure 3(a) with the comparison of the absorption spectrum of the pure PtCP molecules in toluene. Absorption spectrum of the PtCP-bounded surface-modified NAM (PNAM) was obtained by using diffuse reflectance spectrophotometer to avoid the big scattering of the membrane. Diffuse reflectance spectrum is a type of the absorption spectrum measured by scattering from the surface of sample. This diffuse reflectance spectrum is translated into the absorption spectra by the Kubelka-Munk method [23]. The spectrum of PtCP shows one B band (400 nm) and two Q bands ($510, 538\text{ nm}$) [13]. The diffuse reflectance absorption spectrum of PNAM also includes the B and Q bands at the similar wavelengths but with

the broader shape and the red-shifted peak position. Such difference in the peak width and position is possibly due to the self-coupling of the PtCP molecules attached on the surface and the inhomogeneous broadening nature of PtCP to the surface of PNAM [11, 24, 25]. The fluorescence was not observed for the pure PtCP and PNAM. Whereas the phosphorescence spectrum of PtCP in Figure 3(b), at 510 nm excitation, presents the peaks at 660 nm and 725 nm . In case of PNAM, the phosphorescence spectrum shows a similar red shift due to the same nature for the excited state of the PtCP molecules bonded to NAM as in their ground states [11].

The most critical factor for the proof of the singlet oxygen generation from PNAM is the direct detection of the phosphorescence from the singlet oxygen molecules generated by the photoexcited PNAM. The singlet oxygen phosphorescences of PtCP and the PtCP-bounded PNAM were measured at the detection wavelength of 1270 nm in air-saturated toluene and distilled aqueous solution. The measured phosphorescence signals are presented in Figure 4. The decays are fitted to a single exponential function, resulting in the lifetime of the singlet oxygen that depends on the environmental condition [14]. Singlet oxygen lifetime of the pure PtCP molecules in toluene solution is measured to be $\sim 29\text{ }\mu\text{s}$ (Figure 4(a)) that is a characteristic relaxation time of singlet oxygen in toluene solvent [13]. However, the singlet oxygen lifetime for PNAM with the pore diameter of 250 nm is $7.9\text{ }\mu\text{s}$ in toluene solution (Figure 4(b)). Assuming a typical diffusion coefficient for oxygen to be $2.69 \times 10^{-9}\text{ m}^2\text{s}^{-1}$ of D , the average distance that the singlet oxygen can diffuse in toluene is estimated to be approximately 394 nm during $29\text{ }\mu\text{s}$ of its lifetime from the root-mean-square linear displacement of $(2Dt)^{1/2}$ [26]. The fast lifetime of $7.9\text{ }\mu\text{s}$ measured from PNAM in toluene corresponds to 206 nm with the same diffusion coefficient of PtCP in toluene. Although the solvent conditions are the same as toluene, the lifetimes of the singlet oxygen molecules generated from the pure PtCP and PNAM are much different. The diffusion distance of 206 nm for the $7.9\text{ }\mu\text{s}$ is approximately similar to the pore diameter of 250 nm of the PNAM. The inner pore surface of PNAM is expected to be much covered by the hydroxyl groups that provide the efficient quenching for singlet oxygens. Therefore, it is suggested that $7.9\text{ }\mu\text{s}$ of the singlet oxygen lifetime is due to the collisional quenching of singlet oxygen to the hydroxyl groups on the surface of PNAM. [11]. Interestingly, the singlet oxygen life time from PNAM in aqueous solution is measured to be $2.8\text{ }\mu\text{s}$ (Figure 4(c)). It is the value that well correlates with the reported values of $2\sim 4\text{ }\mu\text{s}$ which are the typical singlet oxygen lifetimes in aqueous solution [27]. When the same diffusion distance estimation is done, the lifetime of $2.8\text{ }\mu\text{s}$ from PNAM in aqueous solution corresponds to 94 nm (here, D equals to $1.57 \times 10^{-9}\text{ m}^2\text{s}^{-1}$ in aqueous solution). Since the estimated diffusion distance of 94 nm is much shorter than the pore diameter of PNAM, most singlet oxygens are expected to be more efficiently quenched by the nearby solvent water molecules.

Vesicular stomatitis virus is a very well-characterized lipid-enveloped virus which, together with its sensitivity for photodynamic treatment, makes it a suitable candidate for the study of photodynamic inactivation [28]. Therefore, in

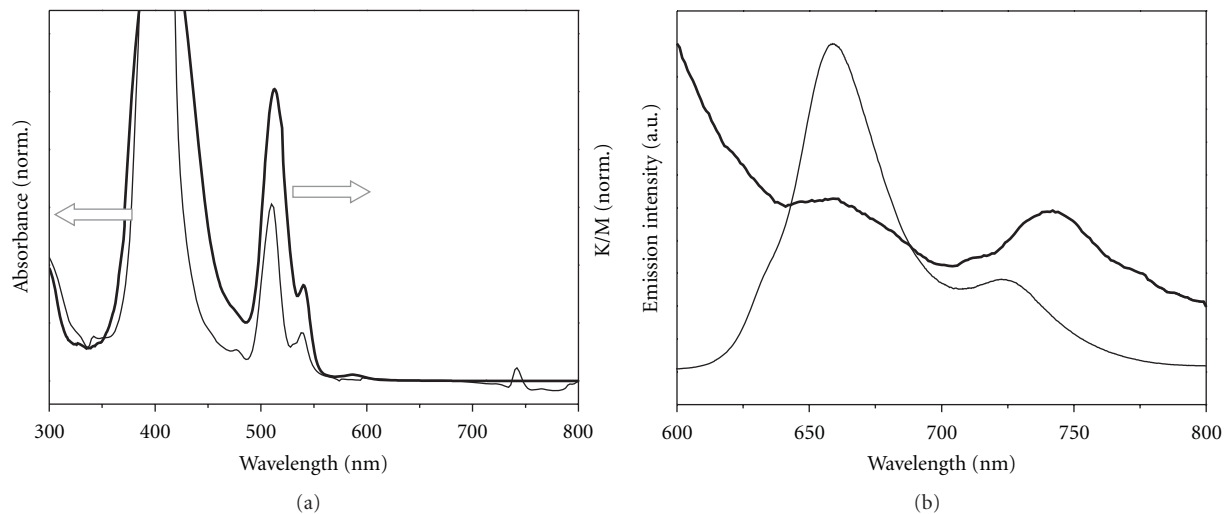


FIGURE 3: (a) Absorption and (b) photoluminescence spectra of the pure PtCP in toluene solution (thin solid line) and PNAM (thick solid line). The absorption spectrum of PNAM is obtained by applying the Kubelka-Munk function to the diffuse reflectance spectrum. The excitation wavelength was 510 nm for the emission spectra.

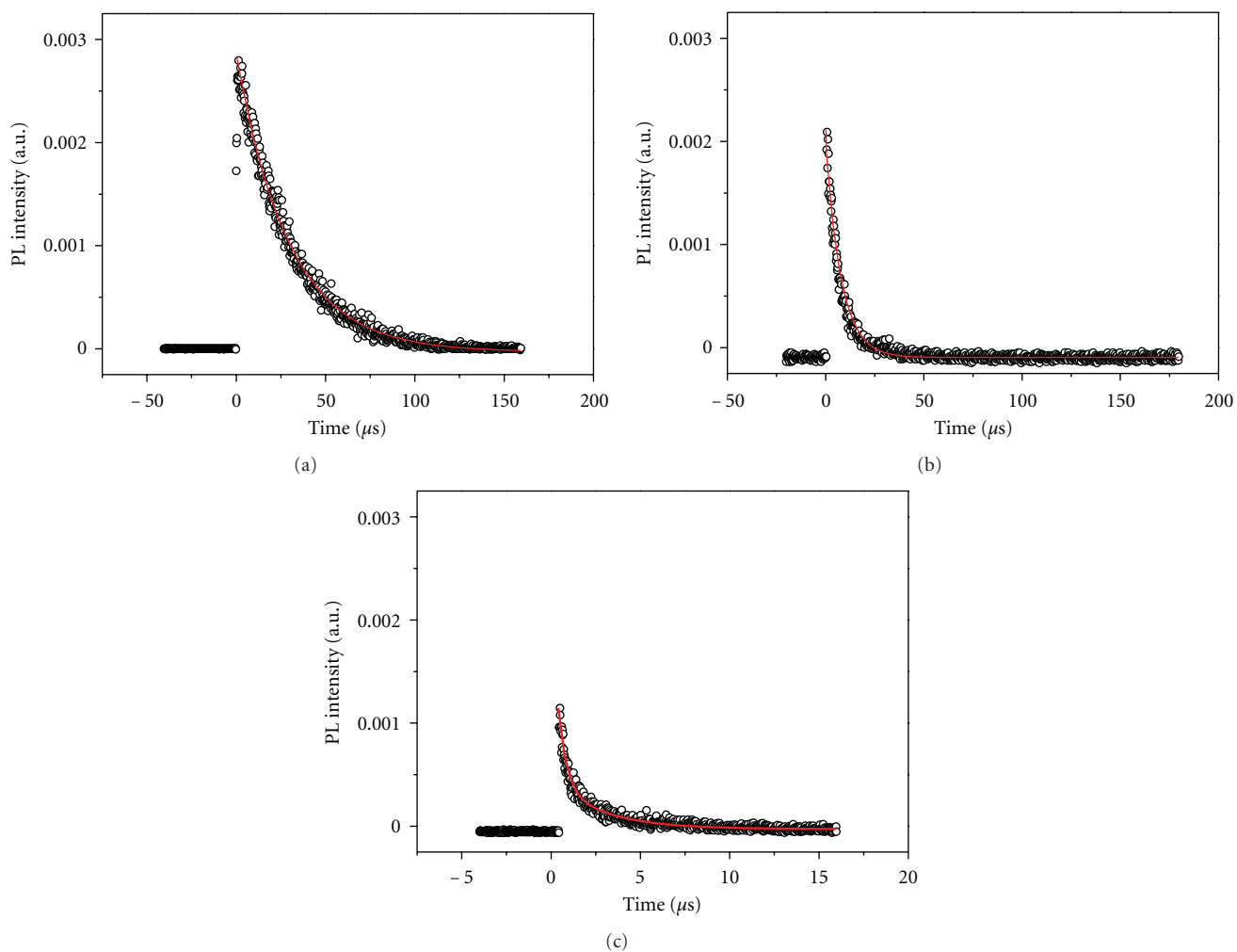


FIGURE 4: Phosphorescence decays of the singlet oxygen from (a) the pure PtCP in toluene, (b) PNAM with pore diameters of 250 nm in toluene, and (c) PNAM with pore diameters of 250 nm in aqueous solution at the detection wavelength of 1270 nm. The solid lines are the fitted lines with a single exponential decay.

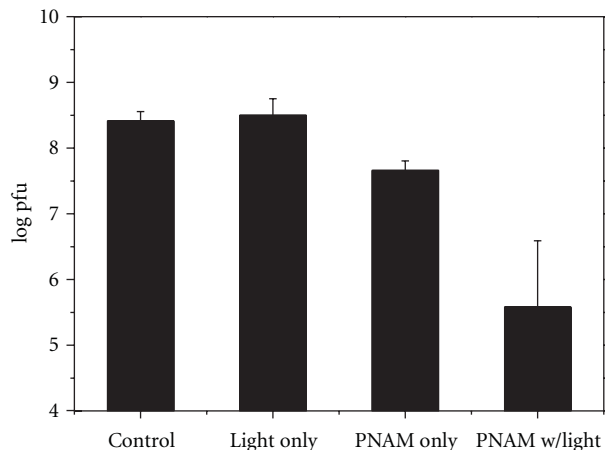


FIGURE 5: Plaques formed in A549 cells by the VSV treated with PNAM and light (5 mW). Extent of the VSV-induced PFU in A549: (control) normal level of PFU in A549 cells caused by VSV, (light only) virus treated with light only without PNAM, (PNAM only) virus treated with PNAM only without light, and (PNAM w/light) virus treated with PNAM and light.

this study, the inactivation of VSV by the photo-irradiated PNAM was investigated to determine the PACT efficiency for the preliminary evaluation of the fabricated PNAM. As shown in Figure 5, the extent of the VSV-induced PFU in A549 cells was not changed by the light only factor. VSV (5×10^8 PFU/mL) caused the normal level of PFU in A549 cells (Figure 5 (control)). The same level of PFU in A549 cells as the control case was reproduced by the virus treated with light only without PNAM. The slightly decreased level of PFU in A549 cells was observed by the virus treated with PNAM without light (5×10^7 PFU/mL). Such a slightly low value of 5×10^7 PFU/mL is possibly expected due to the experimental condition of physical contact during stirring process of solution and also a residual room light effect. However, the virus treated with PNAM with light produced the PFU level of 5×10^5 PFU/mL in A549 cells, which is the significantly lower value than $5 \times 10^8 \sim 5 \times 10^7$ PFU/mL. Therefore, it clearly indicates that the fabricated PNAM in this study is an effective tool for PACT.

4. Conclusions

It has successfully been demonstrated that the singlet oxygen of highly oxidative species is generated from PNAM which is fabricated by the surface modification of NAM with organosilane agents, APTES, and the photosensitizer of PtCP. The singlet oxygen lifetimes depending on the pore diameter of PNAM and the solvent environment were also investigated to understand their dynamics in restricted condition that directly affects the efficiency of PACT. The photo-irradiated PNAM for the application of PACT was performed with the inactivation of VSV. The VSV was significantly inactivated by PNAM-PACT under 5 mW of light condition. Therefore, it suggests that the developed PNAM from this study has a high possibility to be utilized as a photodynamic

antiviral system. Furthermore, based on the experimental results of the controlled singlet oxygen lifetimes by the pore diameter of the membrane, this ROS generating nanoporous membrane can be developed as the spatial distance selective photocatalytic membrane for biological and environmental hazards as well as selective photocatalytic reaction.

Acknowledgments

This study was supported by a grant of the Korea Healthcare Technology R&D Project, Ministry of Health & Family Affairs, Republic of Korea. (grant no. A085136). The authors are grateful to Prof. H. K. Kim for the generous support of PtCP and Dr. S. I. Oh for the help in the preparation of NAM.

References

- [1] Y. Li, Y. Li, H. Liu et al., "Self-assembled monolayers of porphyrin-perylene-tetracarboxylic diimide-[60] fullerene on indium tin oxide electrodes: enhancement of light harvesting in the visible light region," *Nanotechnology*, vol. 16, no. 9, pp. 1899–1904, 2005.
- [2] K. Kalka, H. Merk, and H. Mukhtar, "Photodynamic therapy in dermatology," *Journal of the American Academy of Dermatology*, vol. 42, no. 3, pp. 389–416, 2000.
- [3] R. Bonnetta, M. A. Krystevab, I. G. Lalovb, and S. V. Artarsky, "Water disinfection using photosensitizers immobilized on chitosan," *Water Research*, vol. 40, no. 6, pp. 1269–1275, 2006.
- [4] L. Villén, F. Manjón, D. G. Fresnadillo, and G. Orellana, "Solar water disinfection by photocatalytic singlet oxygen production in heterogeneous medium," *Applied Catalysis B*, vol. 69, no. 1–2, pp. 1–9, 2006.
- [5] C. J. Liu, S. G. Li, W. Q. Pang, and C. M. Che, "Ruthenium porphyrin encapsulated in modified mesoporous molecular sieve MCM-41 for alkene oxidation," *Chemical Communications*, no. 1, pp. 65–66, 1997.
- [6] W. S. Chae, S. W. Lee, S. J. Im et al., "Hierarchically ordered CdS doped nanoporous membrane," *Chemical Communications*, vol. 10, no. 22, pp. 2554–2555, 2004.
- [7] H. Masuda and M. Satoh, "Fabrication of gold nanodot array using anodic porous alumina as an evaporation mask," *Japanese Journal of Applied Physics*, vol. 35, no. 1, part 2, pp. L126–L129, 1996.
- [8] A. M. M. Jani, J. Zhou, M. R. Nussio, D. Losie, J. G. Shapter, and N. H. Voelcker, "Pore spanning lipid bilayers on silanised nanoporous alumina membranes," in *Smart Materials V*, vol. 7267 of *Proceedings of SPIE*, pp. 0T01–0T10, Melbourne, Australia, December 2008.
- [9] V. Szczepanski, I. Vlassioux, and S. Smirnov, "Stability of silane modifiers on alumina nanoporous membranes," *Journal of Membrane Science*, vol. 281, no. 1–2, pp. 587–591, 2006.
- [10] I. Vlassioux, A. Krasnoslobodtsev, S. Smirnov, and M. Germann, "'Direct' detection and separation of DNA using nanoporous alumina filters," *Langmuir*, vol. 20, no. 23, pp. 9913–9915, 2004.
- [11] K. K. Wang, M. S. Min, K. H. Choi et al., "Fabrication and photophysical properties of singlet oxygen generating nanoporous membrane," *Surface & Coatings Technology*, vol. 205, no. 15, pp. 3905–3908, 2011.
- [12] J. McMurry, *Organic Chemistry*, Brooks/Cole, 5th edition, 2000.

- [13] K. K. Wang, K. H. Choi, H. W. Shin et al., "Photophysics of a new photosensitizer with high quantum yield of singlet oxygen generation and its application to stereo-selective synthesis of (+)-deoxoartemisinin," *Chemical Physics Letters*, vol. 482, no. 1–3, pp. 81–86, 2009.
- [14] J. H. Ha, S. Ko, C. H. Lee, W. Y. Lee, and Y. R. Kim, "Effect of core atom modification on photophysical properties and singlet oxygen generation efficiencies: tetraphenylporphyrin analogues core-modified by oxygen and/or sulfur," *Chemical Physics Letters*, vol. 349, no. 3–4, pp. 271–278, 2001.
- [15] Y. J. Park, W. Y. Lee, B. S. Hahn, M. J. Hahn, J. K. Roh, and B. S. Kim, "The effective use of chlorophyll derivatives (CpD) photodynamic therapy of ascites tumors in mice," *Journal of Korean Cancer Association*, vol. 21, pp. 1–6, 1989.
- [16] V. K. S. Hsiao, J. R. Waldeisen, Y. Zheng, P. F. Lloyd, T. J. Bunning, and T. J. Huang, "Aminopropyltriethoxysilane (APTES)-functionalized nanoporous polymeric gratings: fabrication and application in biosensing," *Journal of Materials Chemistry*, vol. 17, no. 46, pp. 4896–4901, 2007.
- [17] K. Ishibashi, K. Tanaka, A. H. Iwata, K. Miyamoto, Y. Kimura, and M. Niwano, "In situ study of DNA attachment and hybridization at silicon surfaces by infrared absorption spectroscopy," *Japanese Journal of Applied Physics*, vol. 47, no. 4, pp. 3204–3208, 2008.
- [18] K. H. Choi, K. K. Wang, S. I. Oh et al., "Singlet oxygen generating nanolayer coatings on NiTi alloy for photodynamic application," *Surface & Coatings Technology*, vol. 205, supplement 1, pp. S62–S67, 2010.
- [19] D. L. Pavia, G. M. Lampman, and G. S. Kriz, *Introduction to Spectroscopy*, Brooks/Cole, 3rd edition, 2001.
- [20] V. R. Rai and S. Agarwal, "Mechanism of self-catalytic atomic layer deposition of silicon dioxide using 3-aminopropyl triethoxysilane, water, and ozone," *Chemistry of Materials*, vol. 23, no. 9, pp. 2312–2316, 2011.
- [21] J. Kim, J. Cho, P. M. Seidler, N. E. Kurland, and V. K. Yadavalli, "Investigations of chemical modifications of amino-terminated organic films on silicon substrates and controlled protein immobilization," *Langmuir*, vol. 26, no. 4, pp. 2599–2608, 2010.
- [22] Y. H. Yu, C. C. M. Ma, S. M. Yuen et al., "Morphology, electrical, and rheological properties of silane-modified silver nanowire/polymer composites," *Macromolecular Materials and Engineering*, vol. 295, no. 11, pp. 1017–1024, 2010.
- [23] P. Kubelka and F. Munk, "Ein Beitrag zur Optik der Farbanstriche," *Zeitschrift für Technische Physik*, vol. 12, pp. 593–601, 1931.
- [24] B. T. Holland, C. Walkup, and A. Stein, "Encapsulation, stabilization, and catalytic properties of flexible metal porphyrin complexes in MCM-41 with minimal electronic perturbation by the environment," *The Journal of Physical Chemistry B*, vol. 102, no. 22, pp. 4301–4309, 1998.
- [25] S. Subbiah and R. Mokaya, "Synthesis of transparent and ordered mesoporous silica monolithic films embedded with monomeric zinc phthalocyanine dye," *Chemical Communications*, vol. 9, no. 7, pp. 860–861, 2003.
- [26] M. Okamoto, "Diffusion processes involved in the exothermic triplet-triplet energy transfer in n-hexane at high pressure: evaluation of diffusion coefficients of benzophenone, triphenylene and naphthalene," *Journal of Photochemistry and Photobiology A*, vol. 162, no. 1, pp. 17–22, 2004.
- [27] K. Lang, J. Mosinger, and D. M. Wagnerova, "Photophysical properties of porphyrinoid sensitizers non-covalently bound to host molecules; models for photodynamic therapy," *Coordination Chemistry Reviews*, vol. 248, no. 3–4, pp. 321–350, 2004.
- [28] J. Parker, P. B. Ahrens, and H. Ankel, "Antiviral effect of cyclopentenone prostaglandins on vesicular stomatitis virus replication," *Antiviral Research*, vol. 26, no. 1, pp. 83–96, 1995.

Research Article

Ag-Cu Bimetallic Nanoparticles Prepared by Microemulsion Method as Catalyst for Epoxidation of Styrene

Hong-Kui Wang,¹ Chao-Yong Yi,¹ Li Tian,² Wen-Juan Wang,¹ Jian Fang,¹ Ji-Hua Zhao,¹ and Wei-Guo Shen³

¹ School of Chemistry and Chemical Engineering, Lanzhou University, Lanzhou 730000, China

² The Chemistry Department, Fudan University, Shanghai 200433, China

³ School of Chemistry and Chemical Engineering, East China University of Science and Technology, Shanghai 200237, China

Correspondence should be addressed to Ji-Hua Zhao, zhaojihua@lzu.edu.cn

Received 8 April 2011; Revised 17 June 2011; Accepted 10 July 2011

Academic Editor: Mohammad Reza Bayati

Copyright © 2012 Hong-Kui Wang et al. This is an open access article distributed under the Creative Commons Attribution License, which permits unrestricted use, distribution, and reproduction in any medium, provided the original work is properly cited.

Ag/Cu bimetallic nanocatalysts supported on reticulate-like γ -alumina were prepared by a microemulsion method using $N_2H_4 \cdot H_2O$ as the reducing agent. The catalysts were activated by calcination followed with hydrogen reduction at 873K, and the properties were confirmed using various characterization techniques. Compared with metal oxides particles, Ag-Cu particles exhibited smaller sizes (<5 nm) after calcination in H_2 at 873K. XPS results indicated that the binding energies changed with the Ag/Cu ratios, suggesting that increasing the copper content gave both metals a greater tendency to lose electrons. Furthermore, Ag-Cu bimetallic nanoparticles supported on γ -alumina showed better catalytic activity on the epoxidation of styrene as compared with the corresponding monometallic silver or copper. The styrene oxide selectivity could reach 76.6% at Ag/Cu molar ratio of 3/1, while the maximum conversion (up to 94.6%) appeared at Ag/Cu molar ratio of 1/1 because of the maximum interaction between silver and copper.

1. Introduction

In recent years, research on silver, copper and gold nanoparticles used as catalysts in CO redox reactions [1–3], NOx reduction [4, 5] and epoxidation of alkenes [6–9] has made great progress. Because of an altered electronic or surface structure of the metal particles, metal nanoparticle catalysts composed of two (or more) different metal elements may result in improved catalyst quality or properties and hence are of great interest from both technological and scientific views [10]. There have been several reports on the synthesis and assembly of bimetal materials such as Pd-Pt [11], Au-Ag [3], Pt-Co [12], and Ni-Mo [13]. Especially, Agrawal et al. [14] made a series of studies on bimetallic or multimetallic nanoparticle catalysts, for example, Au-Ag, Au-Cu, and Au-Ag-Cu. Alumina-based supports are often used in these catalysts because of their mechanical and chemical resistance under reaction conditions. For instance, an alumina supported silver/copper catalyst has a higher ammonia oxidation

activity than catalysts with pure silver or copper particles [15].

Although the Ag-Cu catalyst system has shown excellent catalytic activity in many oxidation reactions, an attempt about using Ag-Cu as catalyst for oxidation of styrene is rarely reported. Oxidation of styrene may be regarded as a very strategic reaction in industrial applications, because styrene oxide (a main product of oxidation of styrene) is one of the most important fine chemical intermediates for producing perfume, drugs, sweeteners, epoxy resins, and so forth [16]. However, it is difficult to find a catalyst that accelerates both conversion and selectivity for this reaction. To solve this problem, Ag-Cu systems are tested herein to see whether this catalyst could meet the requirements.

In order to better understand the working mechanism of such catalysts, it is essential to prepare model systems with a high degree of control over the particle size of the active material. In the past decade, several methods have been used to produce supported catalysts, but it is difficult

to immobilize the nanoparticles on catalyst supports without large aggregates. Water-in-oil microemulsions are transparent, isotropic, and thermodynamically stable nanosized water droplets that are dispersed in a continuous oil phase and stabilized by surfactant molecules at the water/oil interface [17]. This technique has been used for synthesizing various of nanosized particles, such as Cu [18], Au-Ag [17], KCoFePBA [19], and γ -Al₂O₃ nanoparticles [20]. It is suitable for the preparation of particles, because not only the size but also the shape of the particles can be controlled by altering the water-to-surfactant molar ratio (ω) appropriately. The unique advantages of this method, compared to other techniques for controlled nanoparticle preparation, are that the particles can be formed at atmospheric pressure and at room temperature and that large sample volumes can be obtained relatively easily [21].

In this study, we have investigated the deposition of Ag-Cu bimetallic nanoparticles by the coreduction of Ag⁺ and Cu²⁺ with N₂H₄·H₂O as reductant, prepared in w/o microemulsions, on reticulate-like γ -alumina particles which are obtained through the microemulsion technique by our group [22]. After calcination and reduction at 873 K for one hour by H₂, these materials were characterized by several techniques in order to determine their physicochemical compositions. Finally, the performances of catalysts with different molar ratios of Ag/Cu supported on γ -alumina were tested by epoxidation of styrene under mild conditions.

2. Experimental Section

2.1. Chemicals. The nonionic surfactant Triton X-100 [*p*-tert-C₈H₁₇C₆H₄(OC₂H₄)_{9.5}OH] was obtained from Sigma-Aldrich. Cyclohexane (C₆H₁₂, A.R.) used as oil phase and *n*-butanol [CH₃(CH₂)₂CH₂OH, A.R.] used as the cosurfactant were both purchased from Tianjin Chemical Reagent Limited Company. Silver nitrate (AgNO₃, A.R.) was product from Beijing Beihua Fine Chemical Reagent Co., Ltd., Cupric nitrate [Cu(NO₃)₂·3H₂O, 99.5%, A.R.] was received from the Third Branch of Tianjin Chemical Reagent Liu Chang. Aluminum nitrate nonahydrate (Al(NO₃)₃·9H₂O, A.R.) was purchased from Xi'an Chemical Reagent Factory. Ammonia (NH₃·H₂O, 30%, A.R.) was Baiyin LiangYou Chemical Reagent Limited Company products. Styrene (C₈H₈, C.P.) and bromobenzene (C₆H₅Br, A.R.) were bought from Sinopharm Chemical Reagent Limited Company. Hydrazine hydrate (H₂N·NH₂·H₂O, 80.0%, A.R.) was reductant from Tianjin Institute of Fine Chemicals Retrocession. Acetonitrile (CH₃CN, A.R.) used as solvents was received from Tianjin Chemical Reagent Limited Company and tert-butyl hydroperoxide (TBHP)[C₄H₁₀O₂, 70%, C.P.] used as oxidant was bought from Shanghai Sanpu chemical Co., Ltd., Double distilled water was used throughout the experiments.

2.2. Instrumentation. The actual total metal loadings and the Ag/Cu molar ratios of various Ag-Cu/Al₂O₃ samples were determined by the inductively coupled plasma spectrometer on an IRIS ER/S PHEMO instrument. Energy-dispersive X-ray spectroscopy (EDS) (JSM-5600LV, KEVEX) and inductively coupled plasma (ICP) (IRIS ER/S, U.S. PHEMO

company) confirmed the molar ratios of Ag/Cu. Chemical composition information about the samples was obtained by X-ray photoelectron spectroscopy (XPS). The measurement was carried out on a PHI-5702 multifunctional spectrometer using Al K α radiation, and the binding energies were referenced to the C1s line at 284.8 eV from adventitious carbon. All the peaks were fitted using the XPSPEAK version 4.0 peak-fitting program. The specific surface areas of the catalysts and the γ -Al₂O₃ support were calculated by applying the BET method to the N₂ adsorption isotherms, measured at liquid nitrogen temperature on a micromeritics ASAP 2010 apparatus. Rigaku D/MAX-2400 XRD with graphite monochromatized Cu K α radiation ($\lambda = 0.15406$ nm) was used for recording X-ray diffraction (XRD) pattern operating at 40 kV and 40 mA in the 2θ range of 10°–90°. Transmission electron microscopy (TEM) was performed by using a Hitachi H-600 at an accelerating voltage of 100 kV to examine the morphology and dimension of the Ag-Cu nanoparticles as well as nanoalumina. Whether the Ag-Cu nanoparticles supported on the alumina or not was shown clearly via this testing technique. The infrared spectroscopy (IR) spectra were recorded on a NEXUS670 FT-IR spectrometer with samples prepared as KBr pellets. The products of reaction were detected by Gas Chromatography (GC) on a CP-3380 instrument.

2.3. Synthesis. Catalysts of Ag-Cu nanoparticles supported on γ -alumina were synthesized by microemulsion technology (Triton X-100/*n*-butanol/cyclohexane/water system) [22]. Briefly, AgNO₃ and Cu(NO₃)₂ microemulsion with different Ag/Cu atomic ratios as well as the hydrazine hydrate microemulsion were obtained with the same component ratio as the Al(NO₃)₃ microemulsion. Ammonia microemulsion was added dropwise into Al(NO₃)₃ microemulsion with a speed at 4-5 s/d accompanied by stirring. After ammonia microemulsion was dropwised up, 40-minute more reaction time was needed. At the fixed temperature of 293 K, various atomic ratios AgNO₃ and Cu(NO₃)₂ microemulsion were added directly, meanwhile, vigorously stirred for one hour. Thereafter, hydrazine hydrate microemulsion was thrown into the mixture at the same speed 4-5 s/d in order to obtain Ag-Cu bimetallic nanoparticles supported on Aluminum hydroxide. After the total mixture was continuously stirred for 2.5 hours at 293 K, the precipitates were centrifuged one time at 12000 rpm for 40 s and then calcined in air at 893 K for 4 hours. Finally, the solids were reduced at 873 K in H₂ (0.15 mL/min) for one hour, subsequently cooled to room temperature under N₂ flow (0.15 mL/min) to obtain the Ag-Cu/Al₂O₃ catalyst. In all cases, the nominal total metal loading was 2 wt%.

2.4. Catalytic Reaction Tests. The activity of the supported Ag-Cu materials was investigated in the epoxidation of styrene. Before the measurement, the catalyst was prereduced in situ in 99% H₂ at 873 K for 1 h. In a typical oxidation test, 0.5 mmol styrene, 1.5 mmol TBHP, and 5 mg catalyst were added to a 25 mL flask, acetonitrile used as solvents, and the temperature maintained at 355 K. The mixture was kept vigorous stirring for another 6 hours and thereafter was

centrifuged in order to remove the catalyst. The main products were styrene epoxide and phenylaldehyde, as verified by GC using bromobenzene as internal standard.

3. Results and Discussion

3.1. Physical Properties of Catalysts. Table 1 lists the BET surface area, pore volume and average pore size of the catalysts with different Ag/Cu molar ratios. All samples display typical Langmuir type-IV isotherm with a clear adsorption-desorption hysteresis loop (Figure 1). The pore sizes are between 16 and 21 nm; The BET surface areas and the pore volume of the catalysts are in the range of 250~330 cm²/g and 1.05~1.67 cm³/g, respectively. Compared with the results reported by Tian [20], the surface areas and the pore volume are higher than pure reticulate-like γ -Al₂O₃ with the values of 209 m²/g and 0.58 cm³/g, which understandably provides plenty of opportunities for molecular collisions when the bimetallic samples used as a catalyst.

In addition, the EDS results show that the measured molar ratios are slightly larger than the nominal ratios, while the results confirmed by ICP are slightly lower than the nominal ratios. The difference may result from that Cu is more highly dispersed in alumina than Ag [15], which may be observed more directly compare Ag/Cu molar ratio of 1/0 to 0/1 from ICP results so that the area with large black particles contains larger amounts of Ag relative to Cu.

3.2. Morphology and Distribution. We used the microemulsion method to prepare the γ -alumina predecessor, then two metal salts microemulsion were added and chemically reduced using the N₂H₄·H₂O microemulsion as reductant. When the N₂H₄·H₂O microemulsion was slowly added to reduce the two metal ions, the colorless solution slowly turned yellow or golden brown during the reduction process, which indicated the formation of metal colloidal nanoclusters. γ -alumina with different morphologies, such as nanofibers, anomalous spherical particles, and reticulate-like nanostructure [20] used as supports, have been investigated. Overall, it is noticed that reticulate-like nanostructure γ -Alumina has a better distribution for silver and copper because of an ordered pore structure. Figure 2(a) shows the TEM images of Ag/Cu bimetallic particles in reticulate-like γ -Alumina. Because of the formation of silver oxide and copper oxide, the size of bimetallic particles without being reduced by H₂ is between 20 to 60 nm. After being reduced, the metallic oxides turn into metallic state, so the diameter of Ag-Cu is reduced, as shown in Figure 2(b). Unfortunately, because the Ag-Cu nanoparticles are highly dispersed in alumina supports, it is impossible to distinguish the supports and the bimetallic particles from the TEM micrograph.

SEM micrographs (Figures 2(c) and 2(d)) show that the reticulate-like nanostructure is composed of much smaller materials in the presence of bimetallic particles. As catalyst carriers, the reticulate-like nanostructure makes the reactant molecules diffuse easily into the channels and contact conveniently with the internal active components.

In general, it is well known that the smaller particles are normally responsible for high catalytic activities.

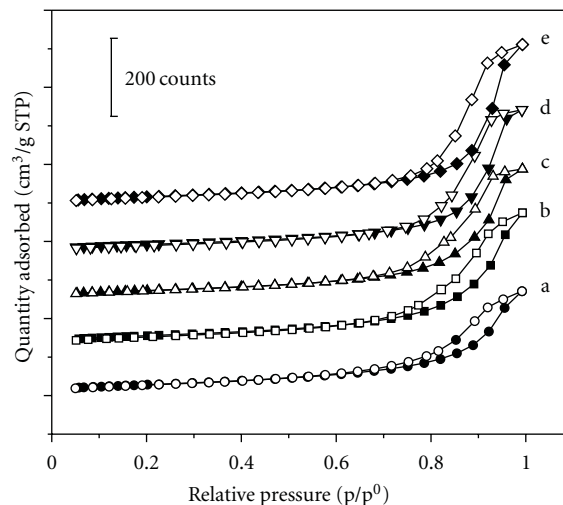


FIGURE 1: N₂ adsorption-desorption isotherms with different Ag/Cu molar ratios. (a) 1/0, (b) 3/1, (c) 1/1, (d) 1/3, (e) 0/1.

3.3. XPS Spectra. We conduct an X-ray photoelectron spectroscopy (XPS) characterization of the catalysts with various Ag/Cu ratios after reduction with H₂, and the results are given in Figure 3 and Table 2. The most intense peak of Ag 3d occurs at about 368.1 eV for the pure Ag/ γ -Al₂O₃ catalyst, and the maximum binding energy of Cu 2p in the pure Cu/ γ -Al₂O₃ is 932.4 eV. Considering the sufficient pretreatment by H₂, we propose that both silver and copper are in their respective metallic state, which are confirmed by the results of IR measurement. With the increase of copper component, for the bimetallic catalyst samples, the positive peak shift (e.g., 932.4 eV → 933.7 eV) compared with pure Cu/ γ -Al₂O₃ suggests that there is an intimate contact between silver and copper, and the interaction from each other seems to give Cu a slightly greater tendency to lose electrons. Similarly, the binding energy of Ag_{3d5/2} for the bimetallic catalyst samples also has the same positive peak shift (e.g., 368.1 eV → 368.8 eV) compared with pure Ag/ γ -Al₂O₃, which means the interaction of two metals also enables Ag to exhibit a greater tendency to lose electrons [23]. At an Ag/Cu molar ratio of 1/1, the interaction between silver and copper comes to the maximum value. In summary, that the binding energy changes with the Ag/Cu molar ratios in bimetallic catalyst samples suggests that the interaction between silver and copper leads to greater tendency to lose electrons for both metals.

3.4. Microstructural Characterization. Figure 4 shows the XRD patterns of the calcined and reduced samples with various Ag/Cu ratios. All the samples contained four peaks positioned at $2\theta = 37.4^\circ, 45.9^\circ, 60.7^\circ,$ and 67.4° , consistent with the report by He et al. [24], and correspond to (311), (400), (333), and (440) lattice planes of γ -Al₂O₃, respectively. Three peaks corresponding to the (110), (111), and (311) reflections of Ag are only visible in b and c. In addition, the peaks corresponding to Ag decrease rapidly until disappear completely with the increase of the copper content. The peaks attributable to Cu or other copper compounds do not appear at all on the copper-containing samples, which is also

TABLE 1: Chemical composition and textural properties of catalysts.

Ag/Cu (molar ratio)		ICP analysis			Pore size (nm)	Pore volume (cm ³ /g) ^b	BET surface area (m ² /g)
Nominal	EDS analysis ^a	Ag wt%	Cu wt%	Ag/Cu molar ratio			
1/0	1/0	1.52	—	1/0	16.08	1.05	261
3/1	3.17	1.34	0.31	2.55	17.17	1.37	319
1/1	1.58	1.13	0.76	0.88	18.39	1.35	293
1/3	0.42	0.65	1.22	0.31	20.51	1.48	288
0/1	0/1	—	1.89	0/1	20.68	1.67	323

^a Determined before reduction by H₂.

^b Total pore volume obtained from $p/p^\circ = 0.99$.

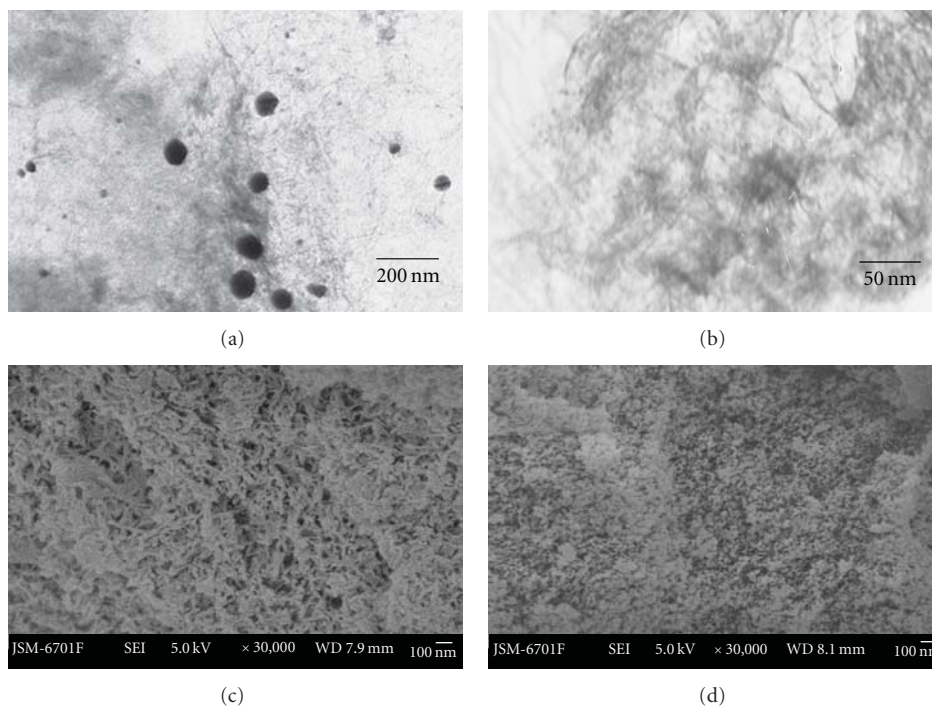


FIGURE 2: (a) TEM image of the catalysts without reducing by H₂, $\omega = 100$ calcined at 893 K. (b) TEM image of the catalysts reduced by H₂ at 873 K, Ag/Cu = 1/1, $\omega = 100$. (c) SEM image of the reticulate-like γ -Alumina, $\omega = 100$, calcined at 893 K. (d) SEM image of the Ag-Cu/ γ -Alumina, $\omega = 100$, Ag/Cu = 1/1, reduction by H₂ at 873 K.

TABLE 2: Binding energies of catalysts determined by XPS.

Molar ratio	Ag _{3d5/2} (eV)	Ag _{3d3/2} (eV)	Cu _{2p3/2} (eV)	Cu _{2p1/2} (eV)
Ag/Cu = 1/0	368.1	374.1	—	—
Ag/Cu = 3/1	368.6	374.2	932.5	955.7
Ag/Cu = 1/1	368.8	374.4	933.7	957.1
Ag/Cu = 1/3	368.2	374.2	933.0	953.8
Ag/Cu = 0/1	—	—	932.4	953.2

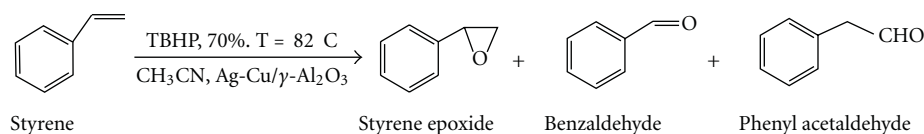
noticed by another group [15]. We hypothesize that a wider diffraction peaks of Cu leads to overlapping of the diffraction peaks of alumina.

The average crystalline size of γ -Al₂O₃ and Ag-Cu mixed colloids calculated by Scherrer equation [25] is to be all less than 5 nm (Table 3). The change of Ag/Cu molar ratios has little effect on both of the crystalline size and the crystalline

phase. It is clear that the average crystalline size of the Ag-Cu mixed colloids is much smaller than the pore size of γ -Al₂O₃, which implies that the crystalline size is determined by the thermodynamics associated with the special nanostructure of the particles, rather than by the pore size of the support [26].

3.5. FT-IR Spectroscopy. Figure 5 shows FT-IR spectra of alumina and different molar ratio of Ag/Cu supported on alumina. The IR absorption peaks at 3471 cm⁻¹ and 1635~1350 cm⁻¹ for all samples are due to H-OH vibrations of H₂O, whilst the bands at 584 cm⁻¹ and 778 cm⁻¹ are attributed to Al-O vibration of γ -Al₂O₃ [27], consistent with the result of XRD. No peaks of other compounds appear in all samples, which are generally regarded as the proof of totally reduction of Ag/Cu by H₂.

3.6. Oxidation of Styrene. Styrene epoxidation catalyzed by Ag-Cu/ γ -Al₂O₃ complex at various molar ratios has been

SCHEME 1: Reaction of styrene oxidation by Ag-Cu/ γ -Al₂O₃ catalysts.TABLE 3: The crystalline size of Ag and Al₂O₃. Angle 2θ , corrected half width (β), corresponding to (111) peak of Ag and (440) peak of γ -Al₂O₃ and particles diameter “ d ” after Scherrer equation for Ag-Cu colloids supported on γ -Al₂O₃.

Ag/Cu	For Ag colloids			For Al ₂ O ₃ colloids		
	2θ (°)	β (°)	“ d ” (nm)	2θ (°)	β (°)	“ d ” (nm)
Al ₂ O ₃	n.c.	n.c.	n.c.	66.005	0.056	2.92
1/0	37.690	0.029	4.98	65.846	0.059	2.77
3/1	37.382	0.029	4.99	67.846	0.042	3.93
1/1	37.382	0.029	4.99	67.846	0.063	2.62
1/3	n.c.	n.c.	n.c.	65.905	0.063	2.59
0/1	n.c.	n.c.	n.c.	66.136	0.046	3.56

TABLE 4: Styrene epoxidation at different ratio of Ag/Cu supported on γ -Al₂O₃.

Entry	Ag/Cu molar ratio	Conversion (%) ^b	Selectivity (%) ^b		
			Epoxide	Benzaldehyde	Phenyl acetaldehyde
I	No catalyst	37.4	None	>99.9	c
II	γ -Al ₂ O ₃	42.1	49.6	46.6	3.8
1	Ag : Cu = 1 : 0/ γ -Al ₂ O ₃	89.7	65.6	34.4	c
2	Ag : Cu = 3 : 1/ γ -Al ₂ O ₃	93.5	76.6	23.4	c
3	Ag : Cu = 1 : 1/ γ -Al ₂ O ₃	94.6	66.9	33.1	c
4	Ag : Cu = 1 : 3/ γ -Al ₂ O ₃	87.5	62.0	38.0	c
5	Ag : Cu = 0 : 1/ γ -Al ₂ O ₃	83.7	20.4	79.6	c

^a Reaction conditions: Ag-Cu/ γ -Al₂O₃ catalyst 5 mg, CH₃CN 2 mL, styrene 0.5 mmol, TBHP 1.5 mmol, 82 °C, 6 h.

^b Determined by GC; use bromobenzene as internal standard, the correction factor is 1.27.

^c Product not detected.

studied using tert-butyl hydroperoxide (TBHP) as oxidant (based on reaction Scheme 1). The mixed organic phase after reaction is sampled for off-line GC analysis, and it is confirmed that benzaldehyde and styrene oxide are the main products in this catalytic system. Using bromobenzene as internal standard, the correction factor is 1.27, and the results of the styrene oxidation are summarized in Table 4. As can be seen from the results, the conversion of styrene has been improved with addition of either Ag or Cu. In contrast, in the simultaneous presence of copper and silver, that is, Ag-Cu bimetallic catalysts, much higher catalytic activity was shown than that of the corresponding monometallic silver or copper supported on γ -Al₂O₃ catalysts. It is proposed that the addition of copper can help to improve the conversion of styrene, whereas the role of silver is to adjust the selectivity of styrene epoxide. Therefore, the selectivity of styrene epoxide can be controlled by adjusting the Ag/Cu molar ratio. The maximum selectivity of styrene epoxide (up to 76.6%) appears at Ag/Cu molar ratio of 3/1, as the conversion of styrene is up to 93.5%. Additionally, owing to the maximum value of the interaction between silver and copper at Ag/Cu molar ratio of 1/1, the maximum conversion (94.6%) appears. A possible mechanism may be that

peroxidic oxygen adsorbs on Ag, while styrene molecules are adsorbed on the crystal surface of Cu; initial complex formation between bimetallic catalyst and tert-butyl hydroperoxide renders the peroxidic oxygen more electrophilic and hence more labile to attack by an olefinic double bond [6]; meanwhile, XPS results demonstrate that the silver and copper components are in intimate contact with each other so that the O₂⁻ adsorbed on the silver surface can migrate to the copper surface and react with the adsorbed styrene easily. However, on the basis of the ratio of 1/1, further larger copper content causes lower conversion, styrene oxide selectivity for Cu is more metallic activity than Ag, and a number of copper oxides might be formed during the reaction process for the excess oxidant. Then, the presence of copper oxides perhaps prevent the further reaction [28], and wherefore Cu shows the lowest conversion, and the conversion of 1/3(Ag/Cu) catalyst is lower than that of Ag/Cu at the ratio of 1/0. In addition, the styrene oxide selectivity decreases with addition of copper component from Ag/Cu molar ratio of 3/1 to 1/3, which may be attributed to the unstable styrene oxide product in the presence of massive copper. In such conditions, the oxidation of metallic Cu by styrene oxide perhaps becomes a favored reaction.

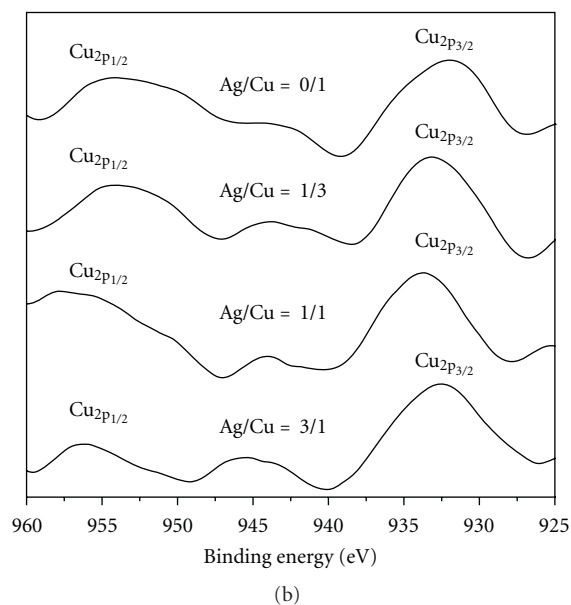
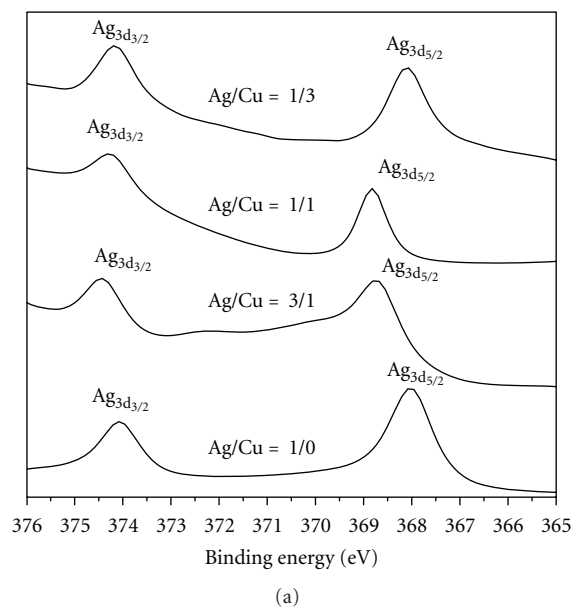


FIGURE 3: XPS spectra of Ag-Cu/ γ -alumina with different Ag/Cu molar ratios.

4. Conclusions

In summary, we have developed a microemulsion method for loading Ag-Cu bimetallic nanoparticles confined in γ -alumina at room temperature, and the physicochemical properties have been investigated. Detailed studies by XRD, TEM, and SEM methodology reveal that the new Ag-Cu bimetallic nanoparticles supported on the reticulate-like γ -alumina distribute evenly and have smaller size. It is interinteresting to note that there is an interaction between silver and copper that makes both metals have a greater tendency to lose electrons. Furthermore, high activity in the oxidation of styrene is observed using the synthesized materials as catalysts, which may be due to the

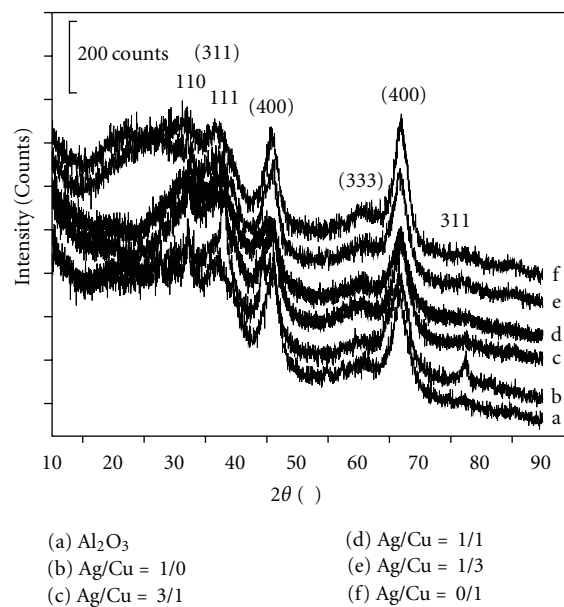


FIGURE 4: Wide-angle XRD patterns of γ - Al_2O_3 and Ag-Cu bimetallic nanoparticles supported on γ - Al_2O_3 at various molar ratios. [Metal salts]/[$\text{N}_2\text{H}_5\text{OH}$] = 1/10; ω = 100; reaction time = 2.5 h; All samples were reduced by H_2 at 873 K and γ - Al_2O_3 was calcined at 893 K.

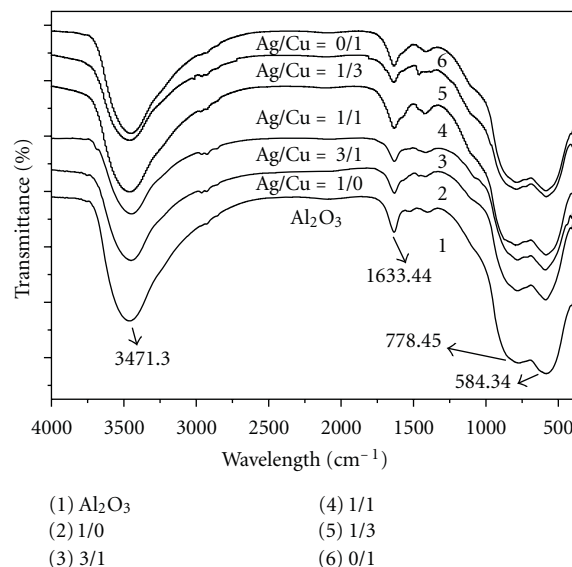


FIGURE 5: FTIR spectra of alumina and different molar ratio of Ag/Cu supported on alumina.

interaction between silver and copper: Ag plays a key role in adsorption of O_2^- and mainly catalyzes styrene epoxidation to styrene epoxide. Instead, Cu provides more active sites for adsorbing styrene, whilst O_2^- adsorbed on the silver surface can migrate to the copper surface and react with the adsorbed styrene easily. So, the selectivity of styrene oxide has a close relationship with the amount of Ag and can be controlled by adjusting molar ratio of Ag/Cu. In addition, the minimum consumption of noble metals makes the catalysts

cost effective. Bimetallic catalysts prepared herein may also be promising candidates for applications in many other reactions such as in CO oxidation.

Acknowledgments

The authors kindly thank Jianxi Liu, State Key Laboratory of Solid Lubrication, Lanzhou Institute of Chemical Physics, Chinese Academy of Sciences, for assistance with the XPS measurements. Financial support was provided by the National Natural Science Foundation of China (Projects nos. 20603014, 20673059, and 20973061), the Chinese Ministry of Education (Key project 105074), the Committee of Science and Technology of Shanghai (Projects nos. 0652nm010 and 08JC1408100), and the Fundamental Research Funds for the Central Universities (Project lzujbky-2011-116).

References

- [1] C.-W. Yen, M.-L. Lin, S.-A. Wang, S.-A. Chen, J.-M. Chen, and C.-Y. Mou, "CO oxidation catalyzed by Au-Ag bimetallic nanoparticles supported in mesoporous silica," *Journal of Physical Chemistry C*, vol. 113, no. 41, pp. 17831–17839, 2009.
- [2] M. Enever, S. Linic, K. Uffalussy, J. M. Vobs, and M. A. Barteau, "Synthesis, structure, and reactions of stable oxametallacycles from styrene oxide on Ag(111)," *Journal of Physical Chemistry B*, vol. 109, no. 6, pp. 2227–2233, 2005.
- [3] J.-H. Liu, A.-Q. Wang, Y.-S. Chi, H.-P. Lin, and C.-Y. Mou, "Enhancing stability and oxidation activity of cytochrome c by immobilization in the nanochannels of mesoporous aluminosilicates," *Journal of Physical Chemistry B*, vol. 109, no. 25, pp. 40–43, 2005.
- [4] K. Arve, K. Svennerberg, F. Klingstedt et al., "Structure-activity relationship in HC-SCR of NO_x by TEM, O₂-chemisorption, and EDXS study of Ag/Al₂O₃," *Journal of Physical Chemistry B*, vol. 110, no. 1, pp. 420–427, 2006.
- [5] Z.-M. Wang, M. Yamaguchi, I. Goto, and M. Kumagai, "Characterization of Al₂O₃ de-NO(x) catalysts by probing surface acidity and basicity of the supporting substrate," *Physical Chemistry Chemical Physics*, vol. 2, no. 13, pp. 3007–3015, 2000.
- [6] E. Zhan, Y. Li, J. Liu, X. Huang, and W. Shen, "Corrigendum to "A VO_x/meso-TiO₂ catalyst for methanol oxidation to dimethoxymethane" [Catal. Commun. 10 (2009) 2051–2055]," *Catalysis Communications*, vol. 11, no. 3, p. 225, 2009.
- [7] J. T. Roberts and R. J. Madix, "Epoxidation of olefins on silver: conversion of norbornene to norbornene oxide by atomic oxygen on Ag(110)," *Journal of the American Chemical Society*, vol. 110, no. 25, pp. 8540–8541, 1988.
- [8] J. J. Cowell, A. K. Santra, and R. M. Lambert, "Ultrasensitive epoxidation of butadiene on Cu111 and the effects of Cs promotion," *Journal of the American Chemical Society*, vol. 122, no. 10, pp. 2381–2382, 2000.
- [9] J. J. Cowell, A. K. Santra, R. Lindsay, R. M. Lambert, A. Baraldi, and A. Goldoni, "Bonding and reactivity of styrene on Cu(110): heterogeneous alkene epoxidation without the use of silver," *Surface Science*, vol. 437, no. 1, pp. 1–8, 1999.
- [10] J. H. Sinfelt, "Supported "bimetallic cluster" catalysts," *Journal of Catalysis*, vol. 29, no. 2, pp. 308–315, 1973.
- [11] N. Toshima, M. Harada, T. Yonezawa, K. Kushihashi, and K. Asakura, "Structural analysis of polymer-protected Pd/Pt bimetallic clusters as dispersed catalysts by using extended X-ray absorption fine structure spectroscopy," *Journal of Physical Chemistry*, vol. 95, no. 19, pp. 7448–7453, 1991.
- [12] X. Wang, N. Li, L. D. Pfefferle, and G. L. Haller, "Pt-Co bimetallic catalyst supported on single-walled carbon nanotubes: effect of alloy formation and oxygen containing groups," *Journal of Physical Chemistry C*, vol. 114, no. 40, pp. 16996–17002, 2010.
- [13] L. Zhao, K. Fang, D. Jiang, D. Li, and Y. Sun, "Sol-gel derived Ni-Mo bimetallic carbide catalysts and their performance for CO hydrogenation," *Catalysis Today*, vol. 158, no. 3-4, pp. 490–495, 2010.
- [14] V. V. Agrawal, P. Mahalakshmi, G. U. Kulkarni, and C. N. R. Rao, "Nanocrystalline films of Au-Ag, Au-Cu, and Au-Ag-Cu alloys formed at the organic-aqueous interface," *Langmuir*, vol. 22, no. 4, pp. 1846–1851, 2006.
- [15] L. Gang, B. G. Anderson, J. Van Grondelle et al., "Alumina-supported Cu-Ag catalysts for ammonia oxidation to nitrogen at low temperature," *Journal of Catalysis*, vol. 206, no. 1, pp. 60–70, 2002.
- [16] X. Yang, S. Gao, and Z. Xi, "Reaction-controlled phase transfer catalysis for styrene epoxidation to styrene oxide with aqueous hydrogen peroxide," *Organic Process Research & Development*, vol. 9, no. 3, pp. 294–296, 2005.
- [17] D.-H. Chen and C.-J. Chen, "Formation and characterization of Au-Ag bimetallic nanoparticles in water-in-oil microemulsions," *Journal of Materials Chemistry*, vol. 12, pp. 1557–1562, 2002.
- [18] L. Qi, J. Ma, and J. Shen, "Synthesis of copper nanoparticles in nonionic water-in-oil microemulsions," *Journal of Colloid and Interface Science*, vol. 186, no. 2, pp. 498–500, 1997.
- [19] H. Liu, X. Du, P. Gao, J. Zhao, J. Fang, and W. Shen, "Distinct magnetic properties of one novel type of nanoscale cobalt-iron Prussian blue analogues synthesized in microemulsion," *Journal of Magnetism and Magnetic Materials*, vol. 322, no. 5, pp. 572–577, 2010.
- [20] L. Tian, *Study on the preparation of γ -alumina nanomaterials by microemulsion and microemulsion hydrothermal synthesis*, M.S. thesis, Lanzhou University, Lanzhou, China, 2008.
- [21] H. H. Ingelsten, J.-C. Béziat, K. Bergkvist et al., "Deposition of platinum nanoparticles, synthesized in water-in-oil microemulsions, on alumina supports," *Langmuir*, vol. 18, no. 5, pp. 1811–1818, 2002.
- [22] J. Zhao, L. Tian, J. Fang, and W. Shen, "China patent 200810093754.0," 2008.
- [23] A.-Q. Wang, J.-H. Liu, S.D. Lin, T.-S. Lin, and C.-Y. Mou, "A novel efficient Au-Ag alloy catalyst system: preparation, activity, and characterization," *Journal of Catalysis*, vol. 233, no. 1, pp. 186–197, 2005.
- [24] Z. He, A. Zhang, S. Song et al., " γ -Al₂O₃ modified with praseodymium: an application in the heterogeneous catalytic ozonation of succinic acid in aqueous solution," *Industrial and Engineering Chemistry Research*, vol. 49, no. 24, pp. 12345–12351, 2010.
- [25] B. E. Warren, *X-Ray Diffraction*, Addison-Wesley, Reading, Mass, USA, 1969.
- [26] X. Liu, A. Wang, X. Wang, C.-Y. Mou, and T. Zhang, "Au-Cu Alloy nanoparticles confined in SBA-15 as a highly efficient catalyst for CO oxidation," *Chemical Communications*, no. 17, pp. 3187–3189, 2008.
- [27] S. Ramesh, E. Sominska, B. Cina, R. Chaim, and A. Gedanken, "Nanocrystalline γ -alumina synthesized by sono-hydrolysis of

alkoxide precursor in the presence of organic acids: structure and morphological properties." *Journal of the American Ceramic Society*, vol. 83, no. 1, pp. 89–94, 2000.

- [28] J. R. Monnier and G. W. Hartley, "Phase transition in Langmuir films of octadecylmalonic acid," *Journal of Catalysis*, vol. 203, no. 2, pp. 529–531, 2001.

Research Article

A Decrease in NiO-MgO Phase Through Its Solid Solution Equilibrium with Tetragonal $(\text{La}_{1-z}\text{Sr}_z)_2\text{Ni}_{1-y}\text{Mg}_y\text{O}_{4-\delta}$: Effect on Catalytic Partial Oxidation of Methane

Xiong Yin,¹ Liang Hong,^{1,2} and Zhengliang Gong¹

¹ Department of Chemical and Biomolecular Engineering, National University of Singapore, BLK E5 02-02,

4 Engineering Drive 4, Singapore 117576

² Institute of Materials Research and Engineering, 3 Research Link, Singapore 117602

Correspondence should be addressed to Liang Hong, chehongl@nus.edu.sg

Received 2 March 2011; Accepted 11 June 2011

Academic Editor: Hahmid Reza Zargar

Copyright © 2012 Xiong Yin et al. This is an open access article distributed under the Creative Commons Attribution License, which permits unrestricted use, distribution, and reproduction in any medium, provided the original work is properly cited.

Calcination of an oxide mixture consisting of 0.4 La_2O_3 , 0.2 SrCO_3 , $(1-x)\text{NiO}$, and $x\text{MgO}$ at 800°C results in an equilibrium between tetragonal $(\text{La}_{1-z}\text{Sr}_z)_2\text{Ni}_{1-y}\text{Mg}_y\text{O}_{4-\delta}$ phase and NiO-MgO phase. Forming rock-salt NiO-MgO facilitates the NiO to join the tetragonal phase. The size of the NiO-MgO phase in the resulting composite is reduced with the increase in MgO (the x value). The composite thus obtained is used to catalyze partial oxidation of methane, and the maximum methane conversion of ca. 93% is achieved when $x = 0.2$. A further rise in x value results in a monotonic decrease in the methane conversion. X-ray diffraction, electron microscopy, and chemisorption all confirm a decrease in both size and amount of the supported Ni^0 clusters with the increase in MgO dosage. The reduction in size promotes the dispersion of Ni^0 sites and gives rise to both high activity and strong coking resistance.

1. Introduction

Reforming of natural gas (mainly CH_4) into syngas (a mixture of H_2 and CO) is an important industrial process. Syngas is the feedstock of hydrogen, synthetic liquid fuel with ultra-low sulfur, and other value-added chemicals [1–5]. In addition, it can also be used to power solid oxide fuel cells (SOFC). The techniques of transforming methane to syngas include steam reforming, CO_2 reforming and partial oxidation. Steam reforming ($\text{CH}_4 + \text{H}_2\text{O} \rightarrow \text{CO} + 3\text{H}_2$, $\Delta H_{298\text{K}}^0 = +206 \text{ kJ/mol}$) and CO_2 reforming ($\text{CH}_4 + \text{CO}_2 \rightarrow 2\text{CO} + 2\text{H}_2$, $\Delta H_{298\text{K}}^0 = +247 \text{ kJ/mol}$) are highly energy intensive reactions. The steam reforming of methane (SRM) has still been the primary commercial process of syngas production despite its high capital cost [6–10]. On the contrary, the partial oxidation of methane (POM), being mild exothermic in nature ($\text{CH}_4 + (1/2)\text{O}_2 \rightarrow \text{CO} + 2\text{H}_2$; $\Delta H_{298\text{K}}^0 = -36 \text{ kJ/mol}$), is attractive for the production of syngas. Nevertheless, a lack of POM catalyst with both acceptable cost to industry and long-term stable catalytic

performance is the major barrier to the commercialization of the POM process [11–13].

Supported Ni catalysts are very attractive for industrial application because of their low cost and high POM catalytic activity. Nevertheless, most of the Ni-based catalysts are vulnerable to carbon deposition over the metallic Ni particles. Thus, ameliorating chemical resistance of the supported-Ni catalysts against coking has become an area of intensive research since the publication of Prettre et al. [14]. In consequence, different approaches have been developed to date to tackle this problem. Amid them, amalgamation of alkali elements [15], alkaline earth elements [16, 17], or rare earth elements [18] with different types of supports has received positive impacts. Doping Ni surface with other metals to form a surface alloy was also found effective [19–21]. More recently, Ni-containing perovskite oxides were identified to be a unique type of catalytic system for POM. This finding is related to the in situ generation of very tiny metallic Ni nuclei under the POM reaction condition [22–28]. The other noticeable progress was the development

of a protective chemical environment for the Ni catalytic site in nanoscale. Ruckenstein and Hu found that MgO support can stabilize the nickel catalytic sites in the POM reaction due to the formation of a NiO in MgO solid solution [16]. Alternatively, Takenaka et al. [29] disclosed the water-in-oil microemulsion method for the preparation of nanosized nickel metal particles (5 nm) encapsulated by a 10 nm-thick silica shell. This thin shell was confirmed to enhance the POM catalytic stability of the Ni particles enclosed. More recently, Iriondo et al. also proposed that interactions between Ni⁰ and MgO promoted the yield of H₂ in the product of steam reforming of glycerol [30].

To achieve nano-Ni metal particles that are embedded on the surface of an appropriate support, we have developed a K₂NiF₄-supported Ni⁰ catalyst that displays promising POM catalytic activity and stability. This outcome originates from preserving a small amount of NiO during the preparation of the precursor of catalyst, a double perovskite-type oxide (La_{0.5}Sr_{0.5})₂FeNiO_{6-δ} [31]. In this study, the concept is furthered through utilizing the solid state reaction equilibrium between the two solid solutions: the rock salt NiO-MgO and the tetragonal (La_{1-z}Sr_z)₂Ni_{1-y}Mg_yO_{4-δ} (LSNM). The latter one is the major phase in the oxide composite. This design came from the observation of the calcination of an oxide mixture of 0.4 La₂O₃, 0.2 SrCO₃, (1 - x)NiO and xMgO with the stoichiometry as indicated. The presence of a small amount of MgO changes the path of this solid state reaction. Namely, the reaction no longer produces orthorhombic and then perovskite structures with the increase in calcination temperature. Instead, the reaction produces a mixture comprising the tetragonal (La_{1-z}Sr_z)₂Ni_{1-y}Mg_yO_{4-δ} phase, the NiO-MgO solid solution phase, and residues of the other two oxides. With the increase in the stoichiometry of MgO from x = 0.1 to x = 0.5 in the feed, it is found that more NiO-MgO phase will be assimilated into the tetragonal phase at the same calcinations temperature. Hence, this phase transition allows realizing a low-volume fraction but highly dispersed NiO-MgO phase with dilute NiO in it at equilibrium. As a result, this leads to small sizes of Ni(0) clusters that are imbedded in the MgO phase after the mixture is subjected to the reducing atmosphere of POM. Through this synthetic route for Ni(0) clusters, the effect of MgO stoichiometry on the performance of the catalyst in POM was investigated from the fundamental perspective in this work.

2. Experimental

2.1. Preparation of Catalyst Precursors. An oxide mixture of 0.4 La₂O₃, 0.2 SrCO₃, (1 - x)NiO, and xMgO (x = 0, 0.1, 0.2, 0.3, 0.4, 0.5) were prepared by the Pechini method [31]. Stoichiometric amounts of metal (La, Sr, Mg, and Ni) nitrates were dissolved in deionized (DI) water, followed by the addition of citric acid and glycine. The mole ratio of total metal (La, Sr, Mg, and Ni) nitrates : citric acid : glycine was 2 : 1 : 1. The solution was then thickened at 80°C until a gel was formed. The gel was subjected to calcination at 400°C for 2 h, after which a fine powder was

produced. The powder was further calcined at 800°C for 1 h under ambient atmosphere to produce the catalyst precursor.

2.2. Partial Oxidation of Methane. POM was carried out in a fixed-bed microreactor under an atmospheric pressure. The catalyst precursor (100 mg) was loaded in a tubular quartz reactor (I.D. = 8 mm). With the purpose of running POM at isothermal condition, CH₄ and air was mixed with an excess of He to form the feed stream with the volume ratio of CH₄:O₂:N₂:He = 2:1:4:38. Although a low concentration of CH₄ in the feed stream was used, a very high hourly space velocity (GHSV) of 45,780 cm³/(g-h) at STP, which is equivalent to 2,035 cm³/g-h of pure methane, was set to operate the POM. The reaction temperature was set at 850°C in this work, since it is known as the upper middle temperature for POM. The compositions of the reactant and product streams were analyzed by gas chromatography (Perkin Elmer ARNEL, Clarus 500) equipped with TCD detector. The methane conversion (X_{CH₄}), CO selectivity (S_{CO}), and H₂ selectivity (S_{H₂}) were calculated by the following formulae:

$$\begin{aligned} X_{\text{CH}_4} &= \frac{\{\text{CH}_{4,\text{in}}\} - [\text{CH}_{4,\text{out}}]}{[\text{CH}_{4,\text{in}}]} \times 100\% \\ S_{\text{CO}} &= \frac{[\text{CO}_{\text{out}}]}{[\text{CH}_{4,\text{in}}] - [\text{CH}_{4,\text{out}}]} \times 100\% \\ S_{\text{H}_2} &= \frac{0.5 \times [\text{H}_{2,\text{out}}]}{[\text{CH}_{4,\text{in}}] - [\text{CH}_{4,\text{out}}]} \times 100\%. \end{aligned} \quad (1)$$

2.3. Characterization of Catalysts. Crystalline structures of the catalyst precursor formed after being calcined at 800°C and used subsequently in a POM run at 850°C were determined by X-ray diffraction (XRD, SHIMADZU XRD-6000, and Cu Kα radiation) using a scanning rate of 2°/min. The micromorphologies of the catalyst precursors were scrutinized on a field emission scanning electron microscope (FESEM, JEOL JSM-6700F). The images of the nanoscaled Ni clusters were obtained from a transmission electron microscope (TEM, JEOL JEM-2100F). Investigation of the surface state of oxygen species was conducted on an X-ray photoelectron spectrometer (Kratos AXIS HSi System XPS) equipped with Al Kα X-ray source (1486.6 eV) and the take-off angle of 90° with pass energy of 40 eV. C1s (284.6 eV) was used as the internal reference for this characterization.

The adsorption/desorption isotherm of N₂, the temperature-programmed reduction with H₂ (H₂-TPR) and the temperature-programmed desorption with He (O₂-TPD) were performed on a physicochemical adsorber (Quantachrome Autosorb-1 instrument). The specific surface area of a sample was determined by applying the multipoint BET method. The pore volume and average pore diameter of catalyst precursors were obtained from the N₂ desorption isotherm using the BJH method. The H₂-TPR was performed using a sample of 50 mg and a gas (5% H₂ in N₂) flow rate of 80 mL min⁻¹. The O₂-TPD was performed using a sample of 200 mg and a He flow rate of 80 mL min⁻¹. The heating rate

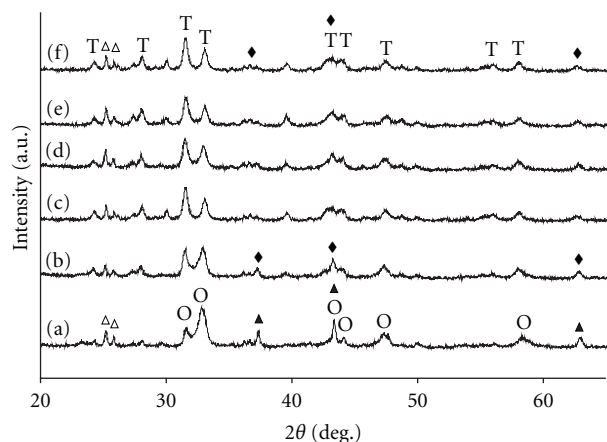


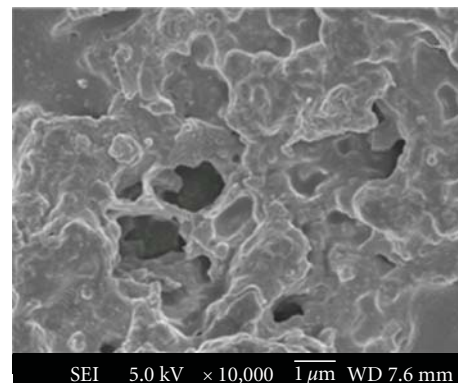
FIGURE 1: X-ray diffraction (XRD) patterns of the catalyst precursors made of $0.4 \text{ La}_2\text{O}_3-0.2 \text{ SrO}-(1-x)\text{NiO}-x\text{MgO}$ (T tetragonal $(\text{La}_{1-z}\text{Sr}_z)_2\text{Ni}_{1-y}\text{Mg}_y\text{O}_{4-\delta}$, O orthorhombic $(\text{La}_{1-z}\text{Sr}_z)_2\text{NiO}_{4-\delta}$, Δ La_2O_3 , \triangle SrCO_3 , \blacklozenge NiO/MgO solution, \blacktriangle NiO): (a) $x = 0$, (b) $x = 0.1$, (c) $x = 0.2$, (d) $x = 0.3$, (e) $x = 0.4$, (f) $x = 0.5$.

for both TPR and TPD was set as $15^\circ\text{C}/\text{min}$ below 850°C and $1^\circ\text{C}/\text{min}$ above 850°C .

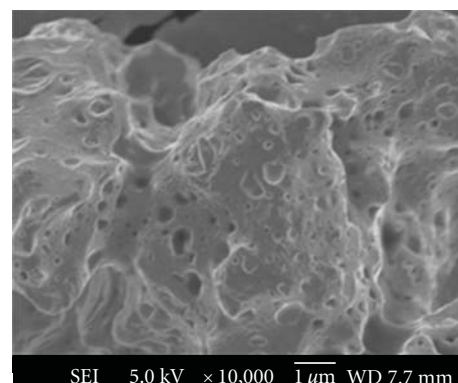
3. Results and Discussion

3.1. Impacts of MgO on the Solid State Reaction Equilibrium.

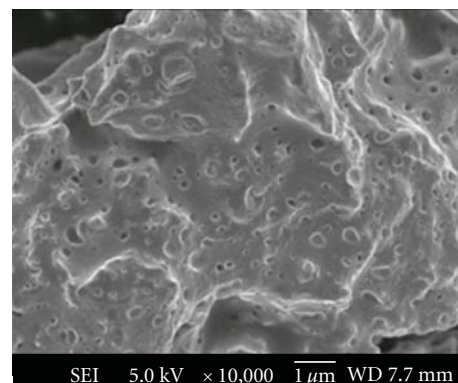
When a mixture of the metal oxides generated from metallo-organic gel (Section 2.1) is subjected to calcination, solid state reaction among the oxides takes place. The reaction extent and the composition of product depend on both the identities of the oxides and the calcination temperature. When the tricomponent mixture of $0.4 \text{ La}_2\text{O}_3$, 0.2 SrCO_3 , and NiO is subjected to calcination, an orthorhombic structure $(\text{La}_{1-z}\text{Sr}_z)_2\text{NiO}_{4-\delta}$ (LSN) is generated at 800°C , and then, a pure perovskite solid solution is resulted at 900°C [32]. However, introduction of a small amount of MgO into the above trioxide mixture, for instance, $0.4 \text{ La}_2\text{O}_3$, 0.2 SrCO_3 , 0.9 NiO , and 0.1 MgO , a tetragonal phase $(\text{La}_{1-z}\text{Sr}_z)_2\text{Ni}_{1-y}\text{Mg}_y\text{O}_{4-\delta}$ (LSNM) becomes predominant (Figure 1) in the resultant composite after calcination at 800°C . A rise of the NiO/MgO stoichiometry ratio in the 4-oxide feed to 8:2, the tetragonal phase becomes solely present. Besides the tetragonal phase, the La_2O_3 , SrCO_3 , and NiO-MgO solid solutions are also found in the XRD diagram. Moreover, with the increase in MgO in the feed, the NiO-MgO phase in the composite decreases. This trend can be discerned from the reduction in intensity of the peaks at 37.5° and 63° as the other peaks of the NiO-MgO phase overlap with those of the tetragonal phase. Accompanying this change, more tetragonal phase was formed in accordance with the rise of its main XRD peak areas (e.g., $2\theta = 31.5^\circ$ and 33°). The other role of MgO is to impede the generation of perovskite structure even when the calcination temperature was raised beyond 900°C . Moreover, accompanying the increase of MgO in the feed, the composite resulted from the solid state reaction at 800°C becomes slightly more porous (Figure 2). However, the BET surface area analysis shows just



(a)



(b)



(c)

FIGURE 2: The FESEM images of the catalyst precursors made of $0.4 \text{ La}_2\text{O}_3-0.2 \text{ SrO}-(1-x)\text{NiO}-x\text{MgO}$: (a) $x = 0$ (b) $x = 0.1$ and (c) $x = 0.5$.

little difference in the pore volumes and pore diameters amid the six samples, while the MgO content promotes the BET surface area of the samples to a finite extent (Table 1).

In light of the H_2 -TPR analysis of the six samples of the composite, according to their XRD identifications, only the orthorhombic LSN and NiO or tetragonal LSNM and the NiO-MgO phases can be reduced under the condition of analysis. Each sample shows three characteristic peaks on its TPR diagram (Figure 3). The peak at the temperature around 400°C (peak I) is ascribed to the reduction of Ni^{3+}

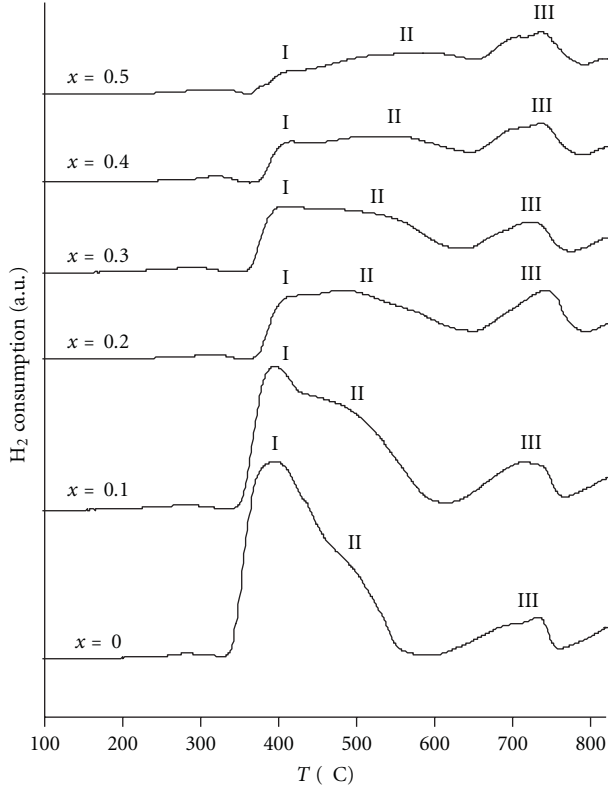


FIGURE 3: H_2 -TPR curves of the catalyst precursors made of $0.4 La_2O_3-0.2 SrO-(1-x)NiO-xMgO$.

TABLE 1: Surface area, pore volume, and pore diameter of the solid reaction products from the oxide mixtures: $0.4 La_2O_3-0.2 SrO-(1-x)NiO-xMgO$.

Parameters*	$x = 0$	$x = 0.1$	$x = 0.2$	$x = 0.3$	$x = 0.4$	$x = 0.5$
S_{BET} (m^2/g)	8	9	10	12	14	17
V_p (cm^3/g)	0.07	0.09	0.09	0.09	0.13	0.09
D_{ave} (nm)	35	37	38	32	37	22

*The multipoint BET surface area (S_{BET}), BJH desorption pore volume (V_p), and the average pore diameter (D_{ave}) of the prepared catalyst precursors.

ions in the orthorhombic ($x = 0$) or in tetragonal phase to Ni^{2+} [27, 33]. It is important to note that this peak becomes weaker with the increase in Mg^{2+} doping extent. Peak II arising in the temperature range from $500^\circ C$ to $600^\circ C$ is due to the reduction of NiO, which is alone when $x = 0$ but mixed with MgO when $x > 0$, to form metallic Ni^0 . Peak III at the temperature higher than $700^\circ C$ is related to the reduction of a part of Ni^{2+}/Ni^{3+} ions in above LSN and LSNM solid solutions into metallic Ni^0 [34]. Thus, the last TPR peaks have basically similar peak areas except the first TPR diagram. The first diagram exhibits the strongest first reduction peak and the smallest last peak amid the six. It implies that a significant part of Ni^{3+} ions in the orthorhombic phase has been directly reduced to Ni^0 in the lower temperature range as proposed above. The decrease in peak I with increasing of the x value is an indication

of the drop of reducibility of Ni^{3+} ions with more MgO being assimilated in the tetragonal phase. It is noteworthy that peak II also becomes weaker and shifts toward high temperature side also with the increasing of MgO. This variation is in agreement with the XRD results as exhibited in Figure 1, which shows that the NiO-MgO solid solution diminishes with increasing of the MgO component. The rise of reduction temperature implies the NiO is better protected by MgO because of more MgO present in the solid solution. It is a clear message for the change of chemical environment of Ni^0 metal clusters generated through the reduction in the NiO domains. In this context, the higher the TPR temperature will be the smaller and the better protected Ni^0 clusters will be produced, and hence, the less reactive they are. As a result, an optimal tradeoff between reactivity and stability of Ni^0 clusters exists, which will be found when the resulting catalysts are assessed in POM. Furthermore, TRP peak III also signifies the degradation of the orthorhombic phase or a part of the tetragonal phase to La-Sr-O oxide, in which the Ni^0 clusters produced were to be imbedded in situ. This point will be further elaborated in the following evaluation of POM. Furthermore, we also examined the six samples downloaded from TPR measurement by TEM. Three samples (with $x = 0, 0.1$ and 0.5) were selected to check the generation of Ni^0 phase (Figure 4). Indeed, it can be seen that the Ni^0 clusters formed in the La-Sr-O oxide and in the MgO oxide decrease in number and size with the increase in MgO content. Typically, the heavy presence of Ni^0 particles in the first sample verifies the strongest first TPR peak this sample exhibits, which has been ascribed to the reduction of Ni^{3+} to Ni^0 , since its third TPR peak is the weakest among the six samples.

3.2. The Oxygen Desorption of the Catalyst Precursors . TPD diagrams of the six samples all exhibit two oxygen desorption peaks (Figure 5). As to the first peak, which appears in the temperature range from $360^\circ C$ to $440^\circ C$, its apex moves toward a higher temperature with the increase in MgO in the 4-oxide feed, $0.4 La_2O_3-0.2 SrO-(1-x)NiO-xMgO$. This desorption peak has been ascribed to the oxygen molecules adsorbed at surface oxygen vacancies (α oxygen) [35–37]. Likewise, an apparent increase in the peak area is also observed with the increase in the x value, meaning that more molecular oxygen desorbs. The above discussion has concluded that the B-site composition, $Ni_{1-y}Mg_y$, in the tetragonal LSNM has a higher y stoichiometric coefficient with the increase in the x value in the feed. This divalent-ion doping is to cause a higher concentration of oxygen vacancies in the LSNM phase, that is, δ . As a result, the concentration of molecular oxygen adsorbed at the surface vacancies including nonstoichiometric oxygen increases, or the oxygen storage capability mounts. Correspondingly, with the increasing of the y value, the adsorbed molecular oxygen requires higher temperature to leave the adsorbent. Regarding the desorption peak arising in temperature range from $600^\circ C$ to $800^\circ C$, it is attributed to the desorption of lattice oxygen (O^{2-} , β oxygen) [36–38]. This desorption occurs accompanying the reduction of a certain number

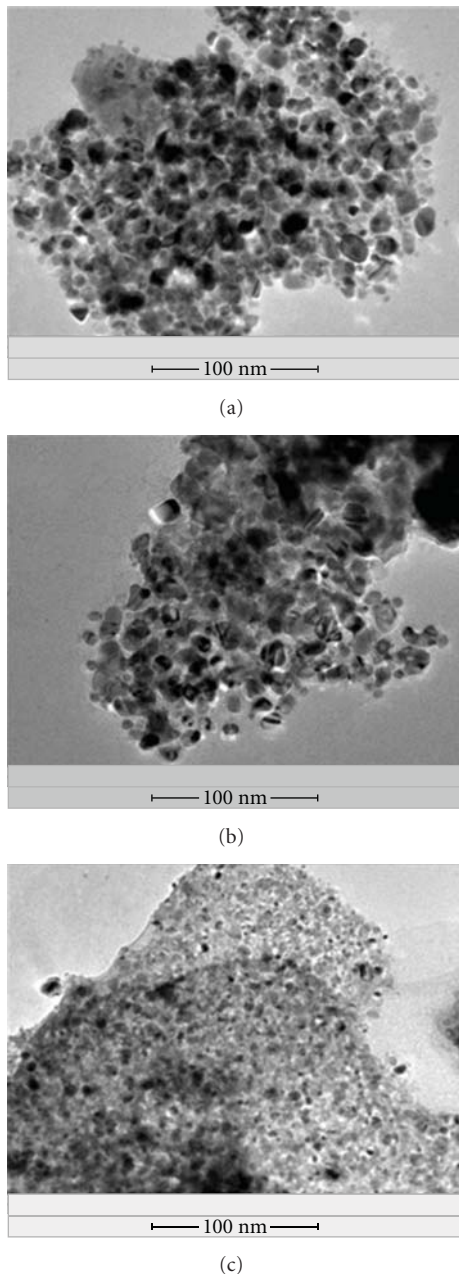


FIGURE 4: TEM images of the H_2 -reduced catalyst precursors made of $0.4 La_2O_3-0.2 SrO-(1-x) NiO-xMgO$: (a) $x = 0$, (b) $x = 0.1$, (c) $x = 0.5$, in which the dark micro-domains are embedded Ni^0 clusters.

of Ni^{3+} ions to Ni^{2+} ions in order to balance the positive charge generated. It is worthy of note that the MgO content (the x value) in the solid reaction mixture affects the extent of desorption and desorption temperature as well. When $x = 0$, this TPD peak was substantially weak, but it turns to much stronger and shifted to a higher temperature with the increase in the x value to 0.1. After that, the peak area increases gradually with the increase in the content of MgO. It is expected that substitution of Mg^{2+} for Ni^{3+} in the B-site of LSM would enhance the ionic bonding

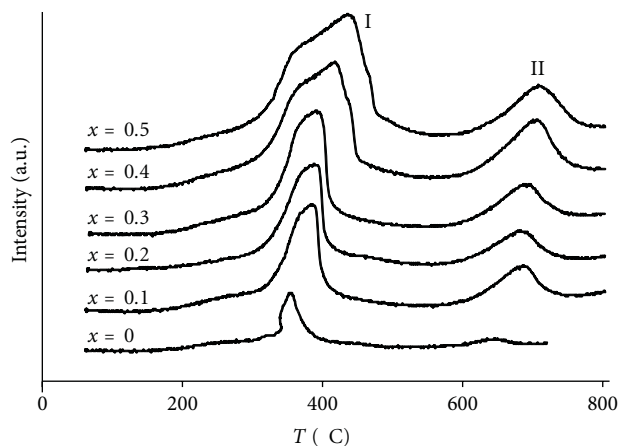


FIGURE 5: O_2 -TPD curves of the catalyst precursors made of $0.4 La_2O_3-0.2 SrO-(1-x) NiO-xMgO$.

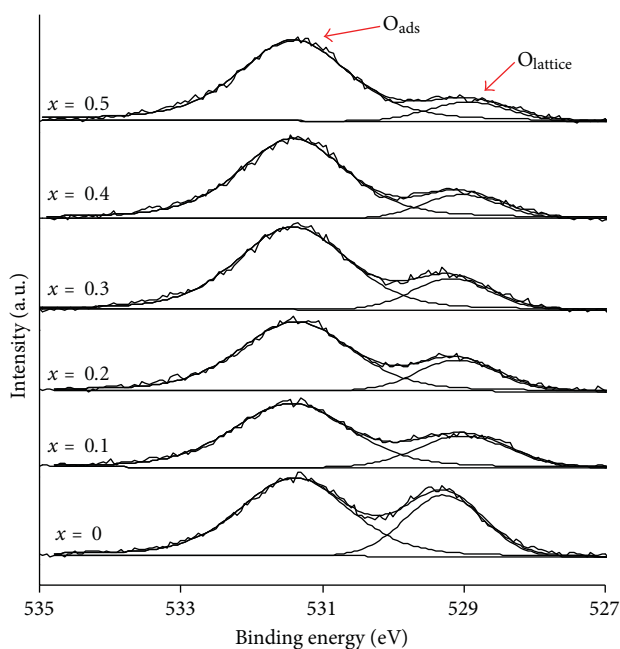


FIGURE 6: $O1s$ XPS of the catalyst precursors made of $0.4 La_2O_3-0.2 SrO-(1-x) NiO-xMgO$.

nature, which can be proved by the increase of the charge on the lattice O^{2-} ions by $O1s$ XPS, and hence promote the mobility of lattice oxygen. At the same time, with the increase in the concentration of lattice oxygen vacancy, the desorption temperature increases, implying the restriction to the desorption of lattice oxygen. From the TPD result, the restriction factor can be overcome at a relatively higher temperature.

The chemical environments of oxygen species in the composite were also investigated by XPS. All the six samples exhibit two peaks at 529.5 eV and 531.5 eV in the $O1s$ spectrum (Figure 6). The former peak has been ascribed to the lattice O^{2-} ($O_{lattice}$) while the latter one to the surface adsorbed oxygen species (O_{ads}) such as $-OH$ [39]. The

TABLE 2: XPS ratios of $O_{\text{lattice}}/O_{\text{ads}}$ species in the different catalysts made of the oxide mixtures $0.4 \text{ La}_2\text{O}_3-0.2 \text{ SrO}-(1-x)\text{NiO}-x\text{MgO}$.

Different stoichiometry coefficient x	XPS ratios of $O_{\text{lattice}}/O_{\text{ads}}$ species
$x = 0$	0.55
$x = 0.1$	0.36
$x = 0.2$	0.27
$x = 0.3$	0.23
$x = 0.4$	0.18
$x = 0.5$	0.15

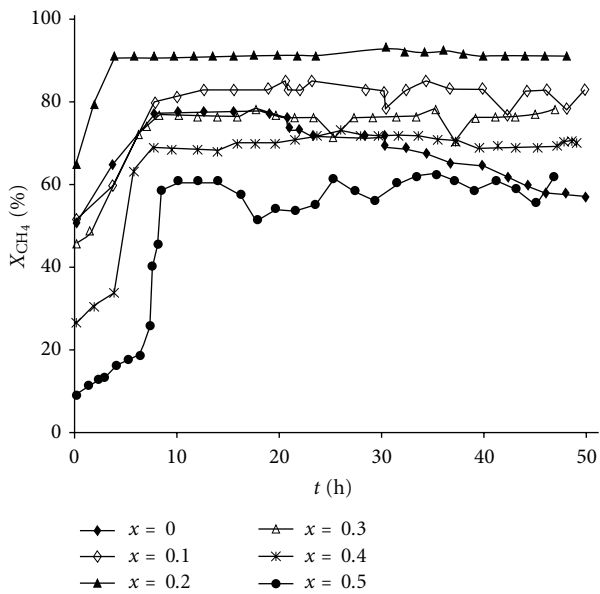
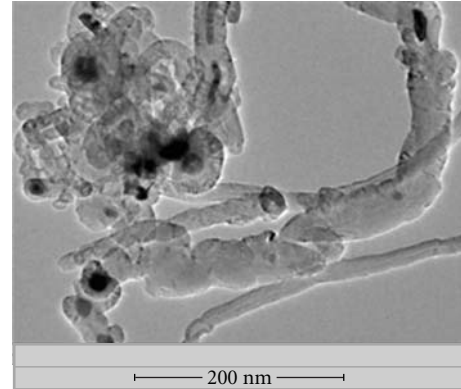


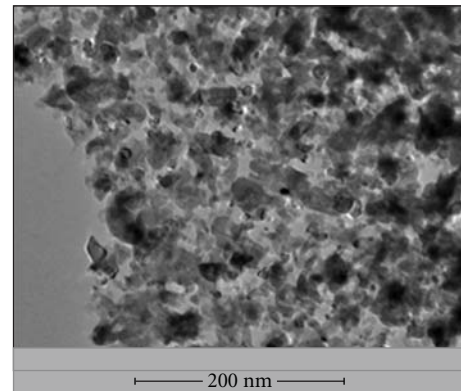
FIGURE 7: POM evaluation of the catalysts generated in situ from the precursors made of $0.4 \text{ La}_2\text{O}_3-0.2 \text{ SrO}-(1-x)\text{NiO}-x\text{MgO}$ at 850°C over a duration of 50 h.

peak area ratio ($O_{\text{lattice}}/O_{\text{ads}}$) represents the atomic ratio of lattice oxygen to oxygen vacancies at surface. The numerical values of the ratio are summarized in Table 2. Clearly, the ratio decreases as the increase in the MgO dosage. It is, therefore, suggested that the concentration of the adsorbed oxygen species be promoted by the oxygen vacancies in the tetragonal LSNM. In addition, we also notice that the binding energy of the lattice O^{2-} slightly reduces with the increase in the Mg^{2+} doping (the x value). It could be interpreted as the promotion of ionic character of the lattice oxygen due to the induction effect of Mg^{2+} ions, which makes the lattice oxygen more mobile because of the decrease in the covalent component.

3.3. Effects of Active Ni^0 Cluster Sizes and Their Exposure on POM. In the context of the above discussion, the Ni^0 clusters generated from the reduction (the TPR experiment) locate in two types of microenvironments: in the La-Sr-O oxide and MgO degraded from the tetragonal phase and in MgO derived from the NiO-MgO solid solution. Additionally,



(a)



(b)

FIGURE 8: TEM examination of the two representative used catalysts after 50 h POM at 850°C (with reference to Figure 7): (a) $x = 0$, (b) $x = 0.2$.

accompanying the increase in MgO, the Ni^0 clusters become smaller in these two locations. Under the POM condition, the nickel ions in each sample loaded are to undergo the reduction similarly by methane to form Ni^0 clusters, namely, in situ generation of the catalytic sites.

After the six samples (or precursors) were loaded respectively in a fixed-bed microreactor, it took about 8 hours to fully convert them to the desired catalysts (i.e., activation) under the reaction condition (Figure 7). Then, the evaluation of their POM reactivity was carried out over a reaction course of 50 h at 850°C . We selected a low- CH_4 feed stream but a high GHSV to evaluate the catalyst. This arrangement could be more sensitive to reflect any loss of catalytic activity than the use of a higher concentration but low space velocity, since methane has a shorter residential time in our setting. The catalyst with nil MgO could retain a CH_4 conversion rate of 78% for around 12 h before declining. At the end of the reaction, the conversion dropped to 58%, and this loss of activity is attributed to the formation of a large extent of carbon filaments on the metallic Ni^0 surface (Figure 8(a)). Besides susceptibility to coking, this catalyst has the highest Ni content, but the Ni^0 sites were apparently not fully used. Such a performance can be traced to the large Ni^0 particles present in the catalyst as shown in Figure 4(a),

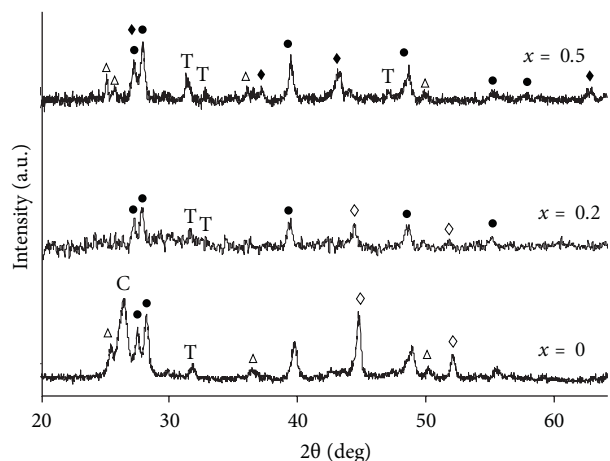


FIGURE 9: XRD patterns of the three used catalysts after POM for 50 h at 850°C (with reference to Figure 7): T the tetragonal phase, \bullet La-Sr-O, \triangle SrCO₃, \blacklozenge NiO/MgO solution, \diamond Ni⁰, and C carbon.

namely, presenting a poor Ni⁰ dispersibility. In contrast to this, the incorporation of a small amount of MgO ($x = 0.1$ and 0.2) into this catalyst system brought about tangible improvement on the catalytic activity. The catalyst with $x = 0.2$ displayed the best performance indicated by conversion and stability. None of carbon filaments were found on the catalyst downloaded from the reactor (Figure 8(b)). A scrutinizing of the TEM images can find that carbon filament grows from Ni⁰ particles of about 20 nm Figure 8(a), while the Ni⁰ particles in Figure 8(b) are smaller, and many of them are surrounded or partially surrounded by a layer, supposedly to be the mixture of La-Sr-O and MgO as proposed above. Alternatively, the catalysts with higher MgO doping extents ($x > 0.2$) resulted in monotonic reduction in the conversion rate. It has been aware of the roles of MgO from the above elaboration: facilitating entering of NiO into the tetragonal phase, suppressing reducibility of the tetragonal phase, and reducing the amount of NiO/MgO solid solution as well as the NiO content in it. Hence, the reactivity declining is not unexpected because of the reduction in both the number and exposure of Ni⁰ clusters, which has been unveiled in Figure 4(c). In addition, XRD patterns of the three catalysts ($x = 0, 0.2$ and 0.5) after POM of 50 h were collected (Figure 9) for further examination. The Ni⁰ cluster peak arising in the three diffraction patterns became weaker with the increase in x value. It is, thereby, confirmed that the catalyst with MgO doping level at $x = 0.2$ balanced the need of both activity and coke resistance. In the meantime, only the XRD pattern ($x = 0$) displayed strong carbon peak, indicating its heavy coking extent, which is plausible to the preceding TEM observation. In addition, the figure also shows that the catalyst with the highest MgO doping ($x = 0.5$) could retain to the highest extent the tetragonal phase. This evidence supports the decreasing of the reducibility of the tetragonal phase with the increasing of MgO doping observed from the TPR analysis.

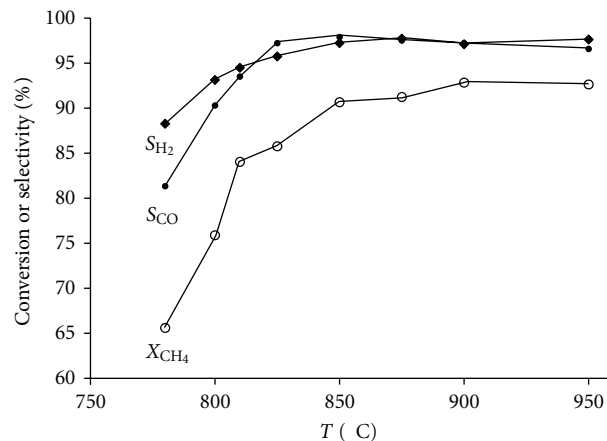


FIGURE 10: Evaluation of temperature effect on the methane conversion and selectivity to H₂ and CO in the POM sustained by the catalyst with $x = 0.2$.

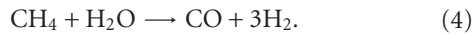
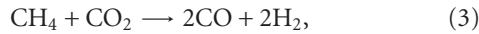
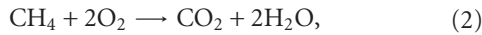
TABLE 3: Coke deposited on the catalysts generated from the oxide mixtures: $0.4 \text{ La}_2\text{O}_3 - 0.2 \text{ SrO} - (1-x) \text{ NiO} - x \text{ MgO}$ after POM at 850°C over 50 h.

Different stoichiometry coefficient x	Coke on catalyst (wt%)
$x = 0$	20.7
$x = 0.1$	4.5
$x = 0.2$	1.6
$x = 0.3$	1.3
$x = 0.4$	0.8
$x = 0.5$	0.3

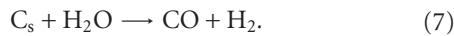
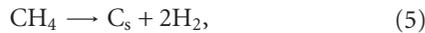
After clarifying the influence due to the presence of MgO in the catalyst precursor on the POM catalytic activity, we then looked at the effect of reaction temperature by using the catalyst precursor with $x = 0.2$ as the model system. The precursor was first subjected to activation for 10 h at 900°C in the microreactor before checking the composition of outlet stream. At each testing temperature, a three-hour dwelling period was set before collecting the experimental data. The catalyst was very stable at each testing temperature, whose performance data are summarized in Figure 10. The methane conversion (X_{CH_4}) levelling off at 900°C claimed the maximum reading of ca. 93% while both CO selectivity (S_{CO}) and H₂ selectivity (S_{H_2}) reached ca. 97% at a lower temperature of ca. 840°C. This phenomenon suggests that the catalyst have more powerful methane combustion and carbon removal trend than methane cracking at temperatures below 900°C. The details will be elaborated in the following section.

3.4. Promoting Catalytic Removal of Coke Deposit. Increasing the MgO component in the precursor enhances the tetragonal phase stability against reducing action of methane and syngas. The benefit of retaining the tetragonal phase lies in reserving oxygen vacancies (Figure 5) to assist the catalytic combustion of methane and removal of deposited surface carbon (Table 3). Noncatalytic methane combustion

happens at temperature as high as 1300°C, while an effective catalyst could lower the methane combustion temperature to as low as 400°C [40, 41]. It has been generally agreed that the POM mechanism involves two consecutive reactions, that is, methane combustion (2) followed by H₂O/CO₂ reforming ((3) and (4)).



The methane conversion is determined by the methane consumption rate through the reactions (2), (3), and (4). Under the present experimental condition (CH₄:O₂ = 2:1 and $T > 700^\circ\text{C}$), reaction (2) could rapidly reach its equilibrium and contribute to the methane conversion by up to nearly 25%. Therefore, reactions (3) and (4) contribute the main part of methane conversion. The reactions (3) and (4) proceed through the pyrolysis mechanism, in which the methane is first cracked on the metallic Ni⁰ particles as shown by step (5) to form coke [42]. The carbon species generated are subsequently removed via the reactions ((6) and (7)) with water and CO₂ produced from the combustion (2) [31, 43].



The C_s removal rate (R_{re}) is the summation of C_s removal rates of reactions (6) and (7). When the C_s removal rate (R_{re}) is greater than the pyrolysis rate or the carbon deposition rate (R_{cr}) (5), no filamentous carbon will be formed over the nickel catalyst surface. The catalyst with nil MgO doping permits prevalent pyrolysis owing to the presence of aggregated Ni⁰ particles (Figure 4(a)); hence, the coking was inevitable as proved by micrograph (Figure 11). On the contrary, with the increase in MgO doping extent, the number and sizes of Ni⁰ catalytic sites were reduced and some of them were shielded by La-Sr-O and MgO as pointed out above. This obviously led to reduction of the methane pyrolysis rate (the R_{cr} value). On the other hand, the tetragonal phase preserved during POM can contribute to the C_s removal (R_{re}) via supplying lattice oxygen. The methane conversion due to steam reforming (4) and dry reforming (3) is determined by whether R_{cr} or R_{re} is larger. In the low MgO doping extent range ($x < 0.2$), $R_{cr} > R_{re}$, the methane conversion increases as the doping of MgO rises, on the contrary, in the high MgO doping range ($x \geq 0.3$), $R_{cr} < R_{re}$, the methane conversion decreases as the doping of MgO rises. Consequently, the catalyst with MgO doping $x = 0.2$ realized a marginally greater R_{re} than R_{cr} , which prevents coking but also maintains the highest methane conversion and maximum CO and H₂ selectivity.

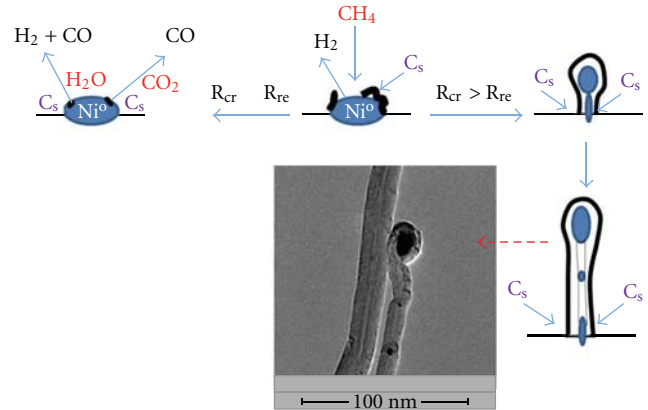


FIGURE 11: Schematic representation of the filamentous carbon fiber formation process during POM reaction.

4. Conclusions

This work started with the attempt of utilizing the solid state reaction equilibrium between the rock salt NiO-MgO solid solution and the tetragonal (La₂Sr_{1-z})₂Ni_yMg_{1-y}O_{3-δ} (LSNM) phase to reduce the size of NiO-MgO phase. This size reduction aimed to improve the coke resistance of the Ni⁰ catalyst in the partial oxidation of methane (POM) without compromising the activity of catalyst. A uniform oxide mixture 0.4 La₂O₃-0.2 SrCO₃-(1-x)NiO-xMgO, where $0 \leq x \leq 0.5$, was subjected to calcination at 800°C to establish the above solid solution equilibrium. The equilibrium shifts to the tetragonal phase side with the increasing of the stoichiometric coefficient x . The XRD characterization of the resulting oxide composites proved this shift of equilibrium. Furthermore, the chemical environments of nickel ions were scrutinized using temperature-programmed reduction (TPR). It showed that the LSMN becomes less reducible with increasing of the Mg²⁺ doping extent, similarly the rise of MgO content in the NiO-MgO phase lowers down the reducibility of it. The lattice oxygen vacancy concentration in LSMN was examined by means of temperature-programmed desorption and X-ray photoelectron spectroscopy. The above composites, when employed to catalyze the partial oxidation of methane, released two types of Ni⁰ sites as indicated by TPR: those embedded in the matrix of the reduced tetragonal phase and those embedded in MgO. The latter one was proven to be the main catalytic site as it existed as nanoparticles and more exposed relative to the former type. As a result, the methane conversion rate attained its climax with using the composite possessing stoichiometric coefficient $x = 0.2$ as the precursor of catalyst. On the contrary, the precursor with $x = 0$ turned out to be low reactive and heavily coke deposited on Ni particles. Increasing x level in this range boosted the dispersity of Ni clusters, which were also embedded in MgO matrix. However, the higher MgO contents ($x > 0.2$) led to decreasing of methane conversion rate. This outcome is attributed to a short of the Ni catalytic sites due to the reduction of the NiO-MgO phase with the increase in MgO dose used. The location of Ni clusters (in MgO) and the

decrease in reducibility of the tetragonal phase contribute to coke resistance of the catalyst. From viewpoint of POM mechanism, the reduction in Ni⁰ clusters lowers down the pyrolysis rate of methane on the clusters but raises the reforming rate of the coke generated.

Acknowledgment

The work has been performed with the financial support by NRF/CRP “Molecular engineering of membrane research and technology for energy development: hydrogen, natural gas, and syngas” (R-279-000-261-281).

References

- [1] L. Chen, Y. Lu, Q. Hong, J. Lin, and F. M. Dautzenberg, “Catalytic partial oxidation of methane to syngas over Ca-decorated-Al₂O₃-supported Ni and NiB catalysts,” *Applied Catalysis A*, vol. 292, no. 1-2, pp. 295–304, 2005.
- [2] H. Y. Wang and E. Ruckenstein, “CO₂ reforming of CH₄ over Co/MgO solid solution catalysts—effect of calcination temperature and Co loading,” *Applied Catalysis A: General*, vol. 209, pp. 207–215, 2001.
- [3] Y. H. Hu and E. Ruckenstein, “Binary MgO-based solid solution catalysts for methane conversion to syngas,” *Catalysis Reviews—Science and Engineering*, vol. 44, no. 3, pp. 423–453, 2002.
- [4] J. Requieres, M. A. Cabrero, V. L. Barrio et al., “Partial oxidation of methane to syngas over Ni/MgO and Ni/La₂O₃ catalysts,” *Applied Catalysis A*, vol. 289, no. 2, pp. 214–223, 2005.
- [5] J. R. Rostrup-Nielsen, “New aspects of syngas production and use,” *Catalysis Today*, vol. 63, no. 2–4, pp. 159–164, 2000.
- [6] J. Requieres, V. L. Barrio, J. F. Cambra et al., “Effect of redox additives over Ni/Al₂O₃ catalysts on syngas production via methane catalytic partial oxidation,” *Fuel*, vol. 87, no. 15-16, pp. 3223–3231, 2008.
- [7] T. Rostrup-Nielsen, “Manufacture of hydrogen,” *Catalysis Today*, vol. 106, no. 1–4, pp. 293–296, 2005.
- [8] S. Freni, G. Calogero, and S. Cavallaro, “Hydrogen production from methane through catalytic partial oxidation reactions,” *Journal of Power Sources*, vol. 87, no. 1, pp. 28–38, 2000.
- [9] Y. Mukainakano, K. Yoshida, S. Kado, K. Okumura, K. Kunimori, and K. Tomishige, “Catalytic performance and characterization of Pt-Ni bimetallic catalysts for oxidative steam reforming of methane,” *Chemical Engineering Science*, vol. 63, no. 20, pp. 4891–4901, 2008.
- [10] B. C. Enger, R. Lødeng, and A. Holmen, “A review of catalytic partial oxidation of methane to synthesis gas with emphasis on reaction mechanisms over transition metal catalysts,” *Applied Catalysis A*, vol. 346, no. 1-2, pp. 1–27, 2008.
- [11] V. R. Choudhary, K. C. Mondal, and T. V. Choudhary, “Partial oxidation of methane to syngas with or without simultaneous steam or CO₂ reforming over a high-temperature stable-NiCoMgCeO_x supported on zirconia-hafnia catalyst,” *Applied Catalysis A*, vol. 306, pp. 45–50, 2006.
- [12] Q. Miao, G. Xiong, S. Sheng, W. Cui, L. Xu, and X. Guo, “Partial oxidation of methane to syngas over nickel-based catalysts modified by alkali metal oxide and rare earth metal oxide,” *Applied Catalysis A*, vol. 154, no. 1-2, pp. 17–27, 1997.
- [13] J. H. Jun, T. J. Lee, T. H. Lim, S. W. Nam, S. A. Hong, and K. J. Yoon, “Nickel-calcium phosphate/hydroxyapatite catalysts for partial oxidation of methane to syngas: characterization and activation,” *Journal of Catalysis*, vol. 221, no. 1, pp. 178–190, 2004.
- [14] M. Prettre, C. Eichner, and M. Perrin, “The catalytic oxidation of methane to carbon monoxide and hydrogen,” *Transactions of the Faraday Society*, vol. 42, pp. 335–340, 1946.
- [15] S. Liu, G. Xiong, W. Yang, and S. Sheng, “The effect of Li and La on NiO/Al₂O₃ catalyst for CH₄/O₂ to syngas reaction,” *Reaction Kinetics and Catalysis Letters*, vol. 68, no. 2, pp. 243–247, 1999.
- [16] E. Ruckenstein and Y. H. Hu, “Methane partial oxidation over NiO/MgO solid solution catalysts,” *Applied Catalysis A*, vol. 183, no. 1, pp. 85–92, 1999.
- [17] S. L. González-Cortés, J. Orozco, D. Moronta, B. Fontal, and F. E. Imbert, “Methane conversion over Sr₂+/La₂O₃ catalyst modified with nickel and copper,” *Reaction Kinetics and Catalysis Letters*, vol. 69, no. 1, pp. 145–152, 2000.
- [18] L. Cao, Y. Chen, and W. Li, “Effect of La₂O₃ added to NiO/Al₂O₃ catalyst on partial oxidation of methane to syngas,” *Studies in Surface Science and Catalysis*, vol. 107, pp. 467–471, 1997.
- [19] V. R. Choudhary, K. C. Mondal, and A. S. Mamman, “High-temperature stable and highly active/selective supported NiCoMgCeO_x catalyst suitable for autothermal reforming of methane to syngas,” *Journal of Catalysis*, vol. 233, no. 1, pp. 36–40, 2005.
- [20] V. R. Choudhary, K. C. Mondal, and T. V. Choudhary, “Oxy-methane reforming over high temperature stable NiCoMgCeO_x and NiCoMgO_x supported on zirconia-hafnia catalysts: accelerated sulfur deactivation and regeneration,” *Catalysis Communications*, vol. 8, no. 3, pp. 561–564, 2007.
- [21] M. G. González, N. N. Nichio, B. Moraweck, and G. Martin, “Role of chromium in the stability of Ni/Al₂O₃ catalysts for natural gas reforming,” *Materials Letters*, vol. 45, no. 1, pp. 15–18, 2000.
- [22] R. Shiozaki, A. G. Andersen, T. Hayakawa et al., “Partial oxidation of methane over a Ni/BaTiO₃ catalyst prepared by solid phase crystallization,” *Journal of the Chemical Society—Faraday Transactions*, vol. 93, no. 17, pp. 3235–3242, 1997.
- [23] V. R. Choudhary, B. S. Uphade, and A. A. Belhekar, “Oxidative conversion of methane to syngas over LaNiO₃ perovskite with or without simultaneous steam and CO₂ reforming reactions: influence of partial substitution of La and Ni,” *Journal of Catalysis*, vol. 163, no. 2, pp. 312–318, 1996.
- [24] S. M. de Lima and J. M. Assaf, “Ni-Fe catalysts based on perovskite-type oxides for dry reforming of methane to syngas,” *Catalysis Letters*, vol. 108, no. 1-2, pp. 63–70, 2006.
- [25] R. Shiozaki, A. G. Andersen, T. Hayakawa et al., “Sustainable Ni/BaTiO₃ Catalysts for Partial Oxidation of Methane to Synthesis Gas,” *Studies in Surface Science and Catalysis*, vol. 111, pp. 701–710, 1997.
- [26] R. N. Basu, F. Tietz, E. Wessel, H. P. Buchkremer, and D. Stöver, “Microstructure and electrical conductivity of LaNi_{0.6}Fe_{0.4}O₃ prepared by combustion synthesis routes,” *Materials Research Bulletin*, vol. 39, no. 9, pp. 1335–1345, 2004.
- [27] H. Provendier, C. Petit, C. Estournès, S. Libs, and A. Kienemann, “Stabilisation of active nickel catalysts in partial oxidation of methane to synthesis gas by iron addition,” *Applied Catalysis A*, vol. 180, no. 1-2, pp. 163–173, 1999.
- [28] E. V. Tsipis, E. A. Kiselev, V. A. Kolotygin, J. C. Waerenborgh, V. A. Cherepanov, and V. V. Kharton, “Mixed conductivity, Mössbauer spectra and thermal expansion of (La,Sr)(Fe,Ni)O_{3-δ} perovskites,” *Solid State Ionics*, vol. 179, no. 38, pp. 2170–2180, 2008.

- [29] S. Takenaka, H. Umebayashi, E. Tanabe, H. Matsune, and M. Kishida, "Specific performance of silica-coated Ni catalysts for the partial oxidation of methane to synthesis gas," *Journal of Catalysis*, vol. 245, no. 2, pp. 392–400, 2007.
- [30] A. Iriondo, M. B. Güemez, V. L. Barrio et al., "Glycerol conversion into H₂ by steam reforming over Ni and PtNi catalysts supported on MgO modified γ -Al₂O₃," *Studies in Surface Science and Catalysis*, vol. 175, pp. 449–452, 2010.
- [31] X. Yin and L. Hong, "Partial oxidation of methane to syngas over the catalyst derived from double perovskite (La_{0.5}Sr_{0.5})₂FeNiO_{6- δ} ," *Applied Catalysis A*, vol. 371, no. 1-2, pp. 153–160, 2009.
- [32] H. J. Wei, Y. Cao, W. J. Ji, and C. T. Au, "Lattice oxygen of La_{1-x}Sr_xMO₃ (M = Mn, Ni) and LaMnO_{3- α} F _{β} perovskite oxides for the partial oxidation of methane to synthesis gas," *Catalysis Communications*, vol. 9, no. 15, pp. 2509–2514, 2008.
- [33] G. S. Gallego, F. Mondragón, J. Barrault, J. M. Tatibouët, and C. Batiot-Dupeyrat, "CO₂ reforming of CH₄ over La-Ni based perovskite precursors," *Applied Catalysis A*, vol. 311, no. 1-2, pp. 164–171, 2006.
- [34] S. N. Pavlova, N. N. Sazonova, V. A. Sadykov et al., "Selective catalytic oxidation of methane to syngas over supported mixed oxides containing Ni and Pt," *Kinetics and Catalysis*, vol. 45, no. 4, pp. 589–597, 2004.
- [35] J. Zhu, X. Yang, X. Xu, and K. Wei, "Effect of strontium substitution on the activity of La_{2-x}Sr_xNiO₄ (x = 0.0–1.2) in NO decomposition," *Science in China, Series B*, vol. 50, no. 1, pp. 41–46, 2007.
- [36] N. Li, A. Boréave, J. P. Deloume, and F. Gaillard, "Catalytic combustion of toluene over a Sr and Fe substituted LaCoO₃ perovskite," *Solid State Ionics*, vol. 179, no. 27–32, pp. 1396–1400, 2008.
- [37] A. Yan, B. Liu, Y. Dong, Z. Tian, D. Wang, and M. Cheng, "A temperature programmed desorption investigation on the interaction of Ba_{0.5}Sr_{0.5}Co_{0.8}Fe_{0.2}O_{3- δ} perovskite oxides with CO₂ in the absence and presence of H₂O and O₂," *Applied Catalysis B*, vol. 80, no. 1-2, pp. 24–31, 2008.
- [38] S. Royer, D. Duprez, and S. Kaliaguine, "Oxygen mobility in LaCoO₃ perovskites," *Catalysis Today*, vol. 112, no. 1–4, pp. 99–102, 2006.
- [39] M. R. Goldwasser, M. E. Rivas, E. Pietri et al., "Perovskites as catalysts precursors: synthesis and characterization," *Journal of Molecular Catalysis A*, vol. 228, no. 1-2, pp. 325–331, 2005.
- [40] J. G. McCarty, "Durable catalysts for cleaner air," *Nature*, vol. 403, no. 6765, pp. 35–36, 2000.
- [41] A. J. Zarur and J. V. Ying, "Reverse microemulsion synthesis of nanostructured complex oxides for catalytic combustion," *Nature*, vol. 403, no. 6765, pp. 65–67, 2000.
- [42] E. P. Murray, T. Tsai, and S. A. Barnett, "A direct-methane fuel cell with a ceria-based anode," *Nature*, vol. 400, no. 6745, pp. 649–651, 1999.
- [43] X. Yin, L. Hong, and Z. L. Liu, "Asymmetric tubular oxygen-permeable ceramic membrane reactor for partial oxidation of methane," *Journal of Physical Chemistry C*, vol. 111, no. 26, pp. 9194–9202, 2007.

Research Article

Catalytic Activity of ZrO₂ Nanotube Arrays Prepared by Anodization Method

Xixin Wang, Jianling Zhao, Xiaorui Hou, Qi He, and Chengchun Tang

School of Material Science and Engineering, Hebei University of Technology, Tianjin 300130, China

Correspondence should be addressed to Jianling Zhao, zhaojl02@mails.tsinghua.edu.cn

Received 24 March 2011; Revised 13 May 2011; Accepted 5 June 2011

Academic Editor: Mohammad Reza Bayati

Copyright © 2012 Xixin Wang et al. This is an open access article distributed under the Creative Commons Attribution License, which permits unrestricted use, distribution, and reproduction in any medium, provided the original work is properly cited.

ZrO₂ nanotube arrays were prepared by anodization method in aqueous electrolyte containing (NH₄)₂SO₄ and NH₄F. The morphology and structure of nanotube arrays were characterized through scanning electron microscope, X-ray diffraction, and infrared spectra analysis. The zirconia nanotube arrays were used as catalyst in esterification reaction. The effects of calcination temperature and electrolyte concentration on catalytic esterification activity have been investigated in detail. Experiments indicate that nanotube arrays have highest catalytic activity when the concentration of (NH₄)₂SO₄ is 1 mol/L, the concentration of NH₄F is 1 wt%, and the calcination temperature is 400°C. Esterification reaction yield of as much as 97% could be obtained under optimal conditions.

1. Introduction

ZrO₂, due to its excellent physical and chemical properties, is widely used in catalysis field. For example, it can be used as catalyst or catalyst carrier in Fischer-Tropsch synthesis, polymerization, isomerization, alkylation and esterification reaction, and so forth [1–4]. In addition, it can also be used in environment and energy aspects including synthesis of biodiesel and catalytic purification of harmful gas [5–9].

The structure and morphology of ZrO₂ have significant effect on its catalytic activity. ZrO₂ nanoparticles can improve catalytic activity due to their large specific surface area [10–12]. However, nanoparticles are difficult to be separated from the reaction medium, and loss quantity is large during the recycle process. Thus, the improvement of ZrO₂ nanocatalysts needs further exploration.

ZrO₂ nanotube arrays have been prepared by anodization method in recent years [13–16]. The nanotube arrays with large specific surface area and tubular structure can be used as nanoreactors. In addition, nanotube arrays are easy to be removed from the reaction system due to their big size. Therefore, ZrO₂ nanotube arrays may have a wide application prospect in the field of catalyst. However, few studies have been done on the application of ZrO₂ nanotube arrays

in catalysis field. In this paper, ZrO₂ nanotube arrays prepared by anodization method in the electrolyte containing SO₄²⁻ are directly used as catalyst in the esterification reaction. The effects of calcination temperature and electrolyte concentration on catalytic esterification activity have been investigated in detail.

2. Experimental

2.1. Preparation of Zirconia Nanotube Arrays Catalyst. Zirconia nanotube arrays were prepared by anodization method in aqueous electrolyte containing 1 M (NH₄)₂SO₄ and 1 wt% NH₄F. Zirconium foil was pretreated according to the method given [17]. Zirconium foil was anode and platinum electrode was cathode, and the distance between two electrodes was 2 cm. The initial voltage was 3 V, and then the voltage was increased at the rate of 3 V/30 min. At the beginning of anodization, a film of dense oxides would fabricate at the surface of zirconium foil which has retarding effect on the oxidation reaction. Increasing the voltages step by step would decrease thickness of the film and enhance the reaction's uniformity. After anodization for 2.5 h, nanotube arrays were peeled off from zirconium foil, dried at 100°C, and calcined for 60 min to obtain the zirconia nanotube arrays catalyst.

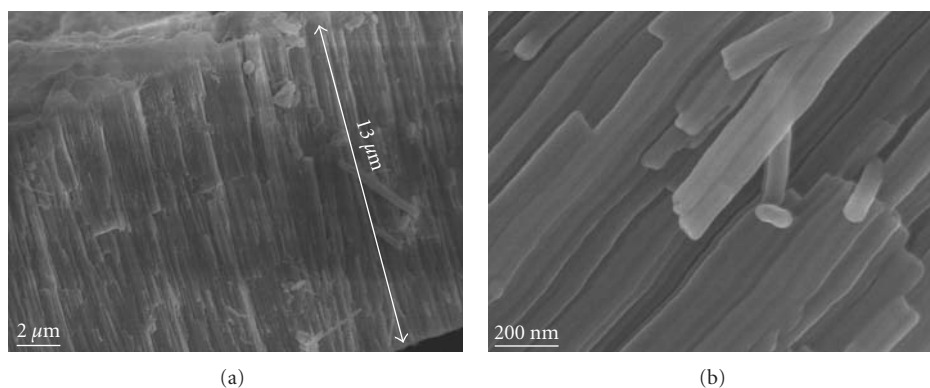


FIGURE 1: The morphology of zirconia nanotube arrays.

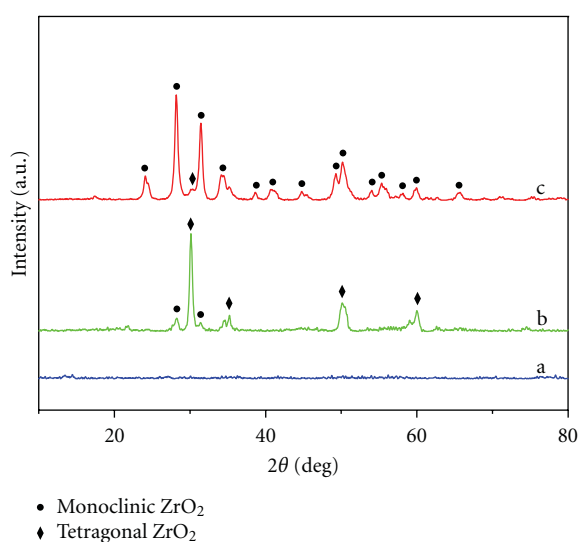


FIGURE 2: The XRD patterns of zirconia nanotube arrays calcined at: (a) 200°C, (b) 400°C, (c) 600°C.

2.2. Characterization of the Catalyst. The morphologies of nanotube samples were observed through Philips XL 30 TMP scanning electron microscope (SEM, 20 kV accelerating voltage). Crystal phase analysis of the samples was conducted through Philips X'pert MPD X-ray powder diffraction analyzer (XRD, copper target, 50 kV, 40 mA, the length of scanning step was 0.04° , and the scope of scanning was 10° – 80° (2θ)). The samples calcined at different temperatures were characterized by Fourier transform infrared spectrometer (FTIR, WQF-410, China) with a scanning scope of $400\sim 4000\text{ cm}^{-1}$.

2.3. Catalytic Activity Experiment. Esterification reactions were carried out in a reflux system. Absolute alcohol and propionic acid (mole ratio = 2:1) were added into a three-neck flask. The catalyst accounting for 2 wt% of the total amount of reaction solution was added. The reaction solution was refluxed at 85°C for 60 min. After the reaction, the product was cooled, and the esterification yield was

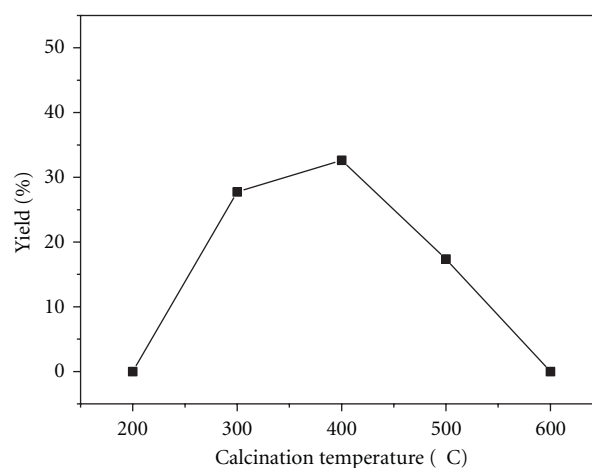


FIGURE 3: Influences of calcination temperatures on catalytic activity.

determined through gas chromatography analysis (GC1100, P-general, China).

3. Results and Discussion

Figure 1 shows the morphology of zirconia nanotube arrays prepared by anodizing zirconium foil in aqueous electrolyte containing 1 M $(\text{NH}_4)_2\text{SO}_4$ and 1 wt% NH_4F for 2.5 h. As shown in Figure 1, average diameter of the nanotube is up to 70 nm, and the average length is up to $13\ \mu\text{m}$. The nanotubes' structure has no obvious changes when the annealed temperature is lower than 600°C , and it would be destroyed to some extent at higher temperatures [18].

Figure 2 shows the XRD patterns of zirconia nanotube arrays calcined at different temperatures. The nanotube samples are amorphous at 200°C (Figure 2(a)). Two mixed crystal structures of tetragonal phase (accounting for 84%, pdf Card no. 80-784) and monoclinic phase (accounting for 16%) emerged at 400°C (Figure 2(b)). When calcined at 600°C , the nanotube samples are mainly composed of monoclinic phase (accounting for 90%, pdf Card no. 37-1484) and a little tetragonal phase (accounting for 10%, Figure 2(c)).

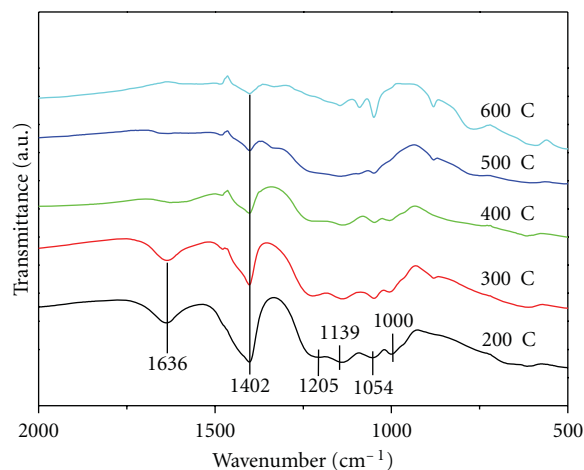


FIGURE 4: Infrared spectra of zirconia nanotube arrays catalyst calcined at different temperatures.

As is calculated from Scherrer formula, the average grain size is 18–26 nm after calcined.

Zirconia nanotube arrays calcined at different temperatures were used as catalyst, and the esterification reactions were carried out under the same conditions as given in Section 2.3. Figure 3 shows the influence of calcination temperatures on the catalytic activity of zirconia nanotube arrays. The catalytic activity first increases and then decreases with the increase of calcination temperature, reaching the maximum value at 400°C.

The FTIR spectra of zirconia nanotube arrays calcined at different temperatures are shown in Figure 4. The infrared absorption band at 1636 cm^{-1} appeared below 400°C is assigned to NH_4^+ . The reason might be that zirconia nanotube arrays were prepared in electrolyte containing $(\text{NH}_4)_2\text{SO}_4$ and NH_4F . During the preparation process, quite a number of NH_4^+ were adsorbed by the sample. Ammonium salt would decompose gradually with the increase of temperature. It would decompose completely, and the infrared absorption band at 1636 cm^{-1} disappeared when the temperature is higher than 400°C. The infrared absorption bands at 1205 cm^{-1} , 1139 cm^{-1} , 1054 cm^{-1} and 1000 cm^{-1} , are assigned to chelate complex between sulfate ion and zirconium ion. The increase of calcination temperature would lead to the desorption of SO_4^{2-} and the decrease of adsorption strength [19].

The infrared absorption band at 1402 cm^{-1} is assigned to surface hydroxyl group and adsorbed water. Along with the increase of the temperature, adsorbed water would desorb, and part of surface hydroxyl group would cross-link and dehydrate and result in decrease of the absorption band intensity at 1402 cm^{-1} .

According to the infrared spectra analysis, calcination temperature affects the catalytic activity through the formation of solid acid structure. Along with the increase of temperature, electrolyte adsorbed by the nanotubes would decompose, and ZrO_2 would react with SO_4^{2-} to form solid acid structure on the surface of nanotube arrays. Thus, the

catalyst activity can be improved obviously. When the calcination temperature is too high, the structure of solid acid would decompose, and the catalyst activity would decrease. In addition, XRD and IR analysis shows that different calcination temperatures would result in the different crystal structures and surface properties, which would influence the combination of SO_4^{2-} and zirconia and lead to the changes of catalytic activities.

Electrolyte concentration has a great influence on catalytic activity. Figure 5(a) shows the influence of the $(\text{NH}_4)_2\text{SO}_4$ concentration on the catalytic activity. With the increase of $(\text{NH}_4)_2\text{SO}_4$ concentration, the esterification yield increases gradually. When the concentration of $(\text{NH}_4)_2\text{SO}_4$ is over 1.0 M, the yield changes much slowly. The reason might be that the higher the concentration is, the more SO_4^{2-} is adsorbed by nanotubes, and the more active centers form at the catalyst. When the concentration is over 1.0 M, the SO_4^{2-} adsorbed by nanotubes is close to saturation. Therefore, further increase of the $(\text{NH}_4)_2\text{SO}_4$ concentration has no more distinct effect on the improvement of catalytic activity.

Figure 5(b) shows the influence of the NH_4F concentration on catalytic activity. With the increase of NH_4F concentration, the esterification yield increases first and then decreases. When the NH_4F concentration is 1.0 wt%, the yield is highest. The partial dissolution of nanotube arrays in electrolyte solution containing F^- results in rougher surface and bigger specific surface area. Thus, the catalytic activity increases accordingly. But excessive dissolution would destroy the structure of nanotube arrays and lead to the decrease of catalytic activity.

According to the results discussed above, zirconia nanotube arrays were prepared by anodization method in aqueous electrolyte containing 1 M $(\text{NH}_4)_2\text{SO}_4$ and 1 wt% NH_4F , followed by calcination at 400°C for 60 min. Taking the nanotubes as catalyst, esterification reaction between dodecanol and propionic acid was conducted at 130°C to produce dodecyl propanoate. The yield is 95.4% when reaction time is 120 min (Figure 6(a)). For the reaction between dodecanol

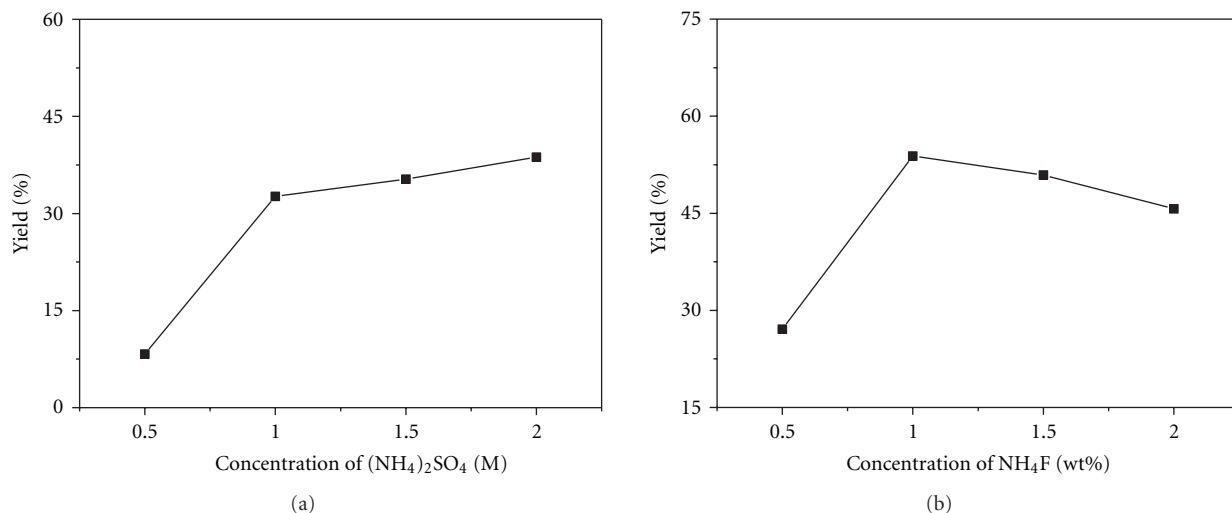


FIGURE 5: Influences of electrolyte concentration on catalytic activity: (a) $(\text{NH}_4)_2\text{SO}_4$, (b) NH_4F .

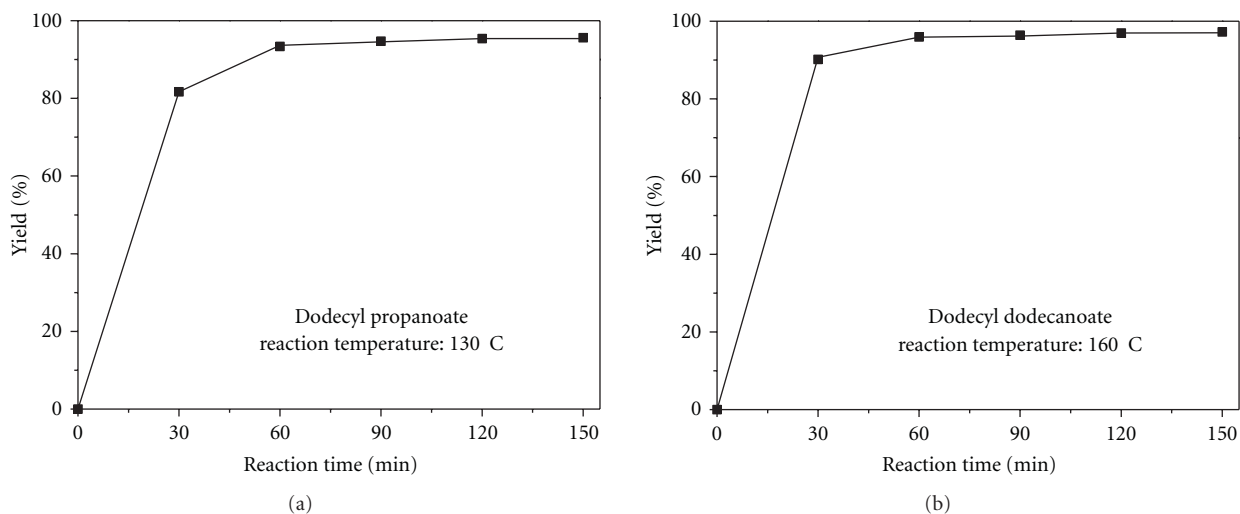


FIGURE 6: Catalytic activity of ZrO_2 nanotube arrays.

and lauric acid at 160°C , the yield of dodecyl laurate is 95.9 % when reaction time is 60 min. When reaction time was extended to 150 min, the yield is as high as 97.3% (Figure 6(b)).

4. Conclusion

ZrO_2 nanotube arrays were prepared by anodization method in aqueous electrolyte containing $(\text{NH}_4)_2\text{SO}_4$ and NH_4F . ZrO_2 nanotube arrays after calcination exhibit good catalytic activity in esterification reaction. Calcination temperature and electrolyte concentration have a great influence on catalytic activity. The ZrO_2 nanotube catalyst which was prepared in aqueous electrolyte containing 1 M $(\text{NH}_4)_2\text{SO}_4$ and 1 wt% NH_4F exhibits highest catalytic activity after calcined at 400°C . The yield of esterification reaction between

dodecanol and lauric acid could reach more than 97%, and the yield of esterification reaction between dodecanol and propionic acid could reach more than 95%.

Acknowledgments

This work was supported by National Natural Science Foundation of China (no. 50972036) and Support Program for Hundred Excellent Innovation Talents from the Universities and Colleges of Hebei Province.

References

- [1] N. Yamamoto, S. Sato, R. Takahashi, and K. Inui, "Synthesis of 3-buten-1-ol from 1,4-butanediol over ZrO_2 catalyst," *Journal of Molecular Catalysis A*, vol. 243, no. 1, pp. 52–59, 2006.

- [2] A. I. Ahmed, S. A. El-Hakam, S. E. Samra, A. A. EL-Khouly, and A. S. Khder, "Structural characterization of sulfated zirconia and their catalytic activity in dehydration of ethanol," *Colloids and Surfaces A*, vol. 317, no. 1–3, pp. 62–70, 2008.
- [3] M. H. Youn, J. G. Seo, S. Park et al., "Hydrogen production by auto-thermal reforming of ethanol over Ni-Ti-Zr metal oxide catalysts," *Renewable Energy*, vol. 34, no. 3, pp. 731–735, 2009.
- [4] S. Chokkaram and B. H. Davis, "Dehydration of 2-octanol over zirconia catalysts: influence of crystal structure, sulfate addition and pretreatment," *Journal of Molecular Catalysis A*, vol. 118, no. 1, pp. 89–99, 1997.
- [5] Y.-M. Park, D.-W. Lee, D.-K. Kim, J.-S. Lee, and K.-Y. Lee, "The heterogeneous catalyst system for the continuous conversion of free fatty acids in used vegetable oils for the production of biodiesel," *Catalysis Today*, vol. 131, no. 1–4, pp. 238–243, 2008.
- [6] A. A. Kiss, A. C. Dimian, and G. Rothenberg, "Solid acid catalysts for biodiesel production—towards sustainable energy," *Advanced Synthesis and Catalysis*, vol. 348, no. 1-2, pp. 75–81, 2006.
- [7] S. Furuta, H. Matsushashi, and K. Arata, "Catalytic action of sulfated tin oxide for etherification and esterification in comparison with sulfated zirconia," *Applied Catalysis A*, vol. 269, no. 1-2, pp. 187–191, 2004.
- [8] E. I. Ross-Medgaarden, W. V. Knowles, T. Kim et al., "New insights into the nature of the acidic catalytic active sites present in ZrO₂-supported tungsten oxide catalysts," *Journal of Catalysis*, vol. 256, no. 1, pp. 108–125, 2008.
- [9] N. Takahashi, A. Suda, I. Hachisuka, M. Sugiura, H. Sobukawa, and H. Shinjoh, "Sulfur durability of NO_x storage and reduction catalyst with supports of TiO₂, ZrO₂ and ZrO₂-TiO₂ mixed oxides," *Applied Catalysis B*, vol. 72, no. 1-2, pp. 187–195, 2007.
- [10] N. Lucas, A. Bordoloi, A. P. Amrute et al., "A comparative study on liquid phase alkylation of 2-methylnaphthalene with long chain olefins using different solid acid catalysts," *Applied Catalysis A*, vol. 352, no. 1-2, pp. 74–80, 2009.
- [11] C. Su, J. Li, D. He, Z. Cheng, and Q. Zhu, "Synthesis of isobutene from synthesis gas over nanosize zirconia catalysts," *Applied Catalysis A*, vol. 202, no. 1, pp. 81–89, 2000.
- [12] X. M. Liu, G. Q. Lu, and Z. F. Yan, "Nanocrystalline zirconia as catalyst support in methanol synthesis," *Applied Catalysis A*, vol. 279, no. 1-2, pp. 241–245, 2005.
- [13] H. Tsuchiya, J. M. MacAk, L. Taveira, and P. Schmuki, "Fabrication and characterization of smooth high aspect ratio zirconia nanotubes," *Chemical Physics Letters*, vol. 410, no. 4–6, pp. 188–191, 2005.
- [14] S. Ismail, Z. A. Ahmad, A. Berenov, and Z. Lockman, "Effect of applied voltage and fluoride ion content on the formation of zirconia nanotube arrays by anodic oxidation of zirconium," *Corrosion Science*, vol. 53, no. 4, pp. 1156–1164, 2011.
- [15] J. Zhao, X. Wang, R. Xu, F. Meng, L. Guo, and Y. Li, "Fabrication of high aspect ratio zirconia nanotube arrays by anodization of zirconium foils," *Materials Letters*, vol. 62, no. 29, pp. 4428–4430, 2008.
- [16] W. J. Lee and W. H. Smyrl, "Oxide nanotube arrays fabricated by anodizing processes for advanced material application," *Current Applied Physics*, vol. 8, no. 6, pp. 818–821, 2008.
- [17] L. N. Wang and J. L. Luo, "Enhancing the bioactivity of zirconium with the coating of anodized ZrO₂ nanotubular arrays prepared in phosphate containing electrolyte," *Electrochemistry Communications*, vol. 12, no. 11, pp. 1559–1562, 2010.
- [18] L. Guo, J. Zhao, X. Wang, X. Xu, H. Liu, and Y. Li, "Structure and bioactivity of zirconia nanotube arrays fabricated by anodization," *International Journal of Applied Ceramic Technology*, vol. 6, no. 5, pp. 636–641, 2009.
- [19] J. R. Sohn and D. H. Seo, "Preparation of new solid superacid catalyst, zirconium sulfate supported on γ -alumina and activity for acid catalysis," *Catalysis Today*, vol. 87, no. 1–4, pp. 219–226, 2003.

Research Article

The Physical Properties of Erbium-Doped Yttrium Iron Garnet Films Prepared by Sol-Gel Method

Ramadan Shaiboub, Noor Baa'yah Ibrahim, Mustafa Abdullah, and Ftema Abdulhade

School of Applied Physics, Faculty of Science and Technology, The National University of Malaysia, Selangor, 43600 Bangi, Malaysia

Correspondence should be addressed to Noor Baa'yah Ibrahim, baayah@ukm.my

Received 23 January 2011; Revised 27 February 2011; Accepted 4 April 2011

Academic Editor: Parvaneh Sangpour

Copyright © 2012 Ramadan Shaiboub et al. This is an open access article distributed under the Creative Commons Attribution License, which permits unrestricted use, distribution, and reproduction in any medium, provided the original work is properly cited.

$\text{Er}_x\text{Y}_{3-x}\text{Fe}_5\text{O}_{12}$ nanoparticle films ($x = 0.0, 0.6, 1.2, 2.0,$ and 2.5) have been synthesized by a sol-gel technique. All of the samples were annealed at 1000°C . The nanostructures were characterized by an X-ray diffractometer (XRD), the magnetic properties and the grain size were studied using a vibrating sample magnetometer (VSM), and a field emission scanning electron microscope (FE-SEM), respectively. The XRD patterns of the films show single phase structure. The sizes of the particles are in the range of 78 to 89 nm. The VSM result shows that the saturation magnetization of $\text{Er}_x\text{Y}_{3-x}\text{Fe}_5\text{O}_{12}$ films decreased with the increment of Er concentration (x).

1. Introduction

The rare-earth iron garnet (RIG) has the general unit formula ($\text{R}_3\text{Fe}_5\text{O}_{12}$), where R is either a trivalent rare-earth ion or yttrium. RIGs belong to the space group $Ia\bar{3}d$. The magnetic ions are distributed over three crystallographic sites with sublattice magnetization Ma [octahedral site, 16 Fe^{3+} ions in a], Md (tetrahedral site, 24 Fe^{3+} ions in d) and Mc dodecahedral site, 24 R^{3+} ions in c. The garnets have eight formula units in a cubic unit cell. The cubic unit cells of RIGs have approximately the same lattice constant which is of the order of 12 \AA [1], due to similar ionic radii of R^{3+} ions. Ionic distribution in garnet is represented as $\{\text{R}^{3+}\} [\text{Fe}_2^{3+}] (\text{Fe}_3^{3+}) \text{O}_{12}^{2-}$. The interaction between the Fe^{3+} ions in [a] and (d) sites is strongly antiferromagnetic due to strong superexchange interaction. The magnetic moment of the rare-earth ions in the {c} sublattice couples antiparallel with the resultant moment of Fe^{3+} ions. One of the common RIGs is YIG ($\text{Y}_3\text{Fe}_5\text{O}_{12}$) which have attracted much attention in telecommunications and data storage industries due to their interesting magnetic and magneto-optic properties [2]. The Y^{3+} in YIG has no magnetic moment, so the net magnetic moment in YIG is due to the unequal distribution of Fe^{3+} ions in the two different sublattices of [a] and (d). YIGs are also of scientific importance because of the wide variety

of magnetic properties that can be obtained by substituting yttrium with a rare-earth (RE) metal [3–9]. Most of the previous studies have concentrated on the preparation of Bi- and Ce-doped YIG (powder and films) nanoparticles because of their high Faraday rotation coefficient [10–17]. Few works have been carried out to study only Er-YIG powder nanoparticles [18–27]. In this paper we studied magnetic properties of Er doped YIG films in the formula $\text{Er}_x\text{Y}_{3-x}\text{Fe}_5\text{O}_{12}$ prepared by sol-gel method. Erbium is chosen because its ionic radius is (1.03 \AA), which is slightly less than ionic radii of yttrium (1.04 \AA) [28, 29], it has an extremely high verdet constant and largest Bohr magneton [30].

2. Experimental

The YIG precursor sol was prepared by a sol-gel method using reagent grade nitrates purchased from Aldrich, Milwaukee, WI, USA. Yttrium nitrate hexahydrate [$\text{Y}(\text{NO}_3)_3 \cdot 6\text{H}_2\text{O}$, 99–95% purity], iron(III) nitrate nonahydrate [$\text{Fe}(\text{NO}_3)_3 \cdot 9\text{H}_2\text{O}$, 98+% purity], and Erbium nitrate pentahydrate [$\text{Er}(\text{NO}_3)_3 \cdot 5\text{H}_2\text{O}$] have been used as the raw materials; 2-methoxyethanol and acetic acid were used as solvents. $\text{Fe}(\text{NO}_3)_3 \cdot 9\text{H}_2\text{O}$ and $\text{Y}(\text{NO}_3)_3 \cdot 6\text{H}_2\text{O}$ were dissolved in the 2-methoxyethanol and refluxed at 80°C for 3 hours.

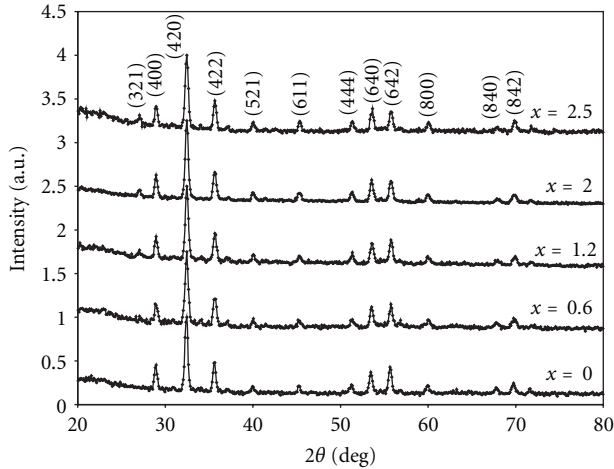


FIGURE 1: XRD patterns for $\text{Er}_x\text{Y}_{3-x}\text{Fe}_5\text{O}_{12}$ thin films.

The $\text{Er}(\text{NO}_3)_3 \cdot 5\text{H}_2\text{O}$ dissolved in acetic acid was added gradually into the Fe–Y solution. Then the refluxing process was continued for 3 hours. Then a small quantity of diethylamine was added to the mixture solution while the pH value was adjusted in the range of 2–3. After cooling down to room temperature, the solution was stirred for 3 days.

The gel was transformed into a film on a quartz substrate using the spin coating technique. The rate of the spinning process was 3500 rpm and it was done for 30 seconds. After the spinning process, the film was heated at 90°C for 2 hours to remove residual solvents. Then the heat treatment was carried out: initial heating at 350°C for 15 minutes at a heating rate of $3^\circ\text{C}/\text{min}$ to burn-off the organic materials followed by heating at 1000°C for 2 hours at a heating rate of $4^\circ\text{C}/\text{min}$ to crystalline the films. The characterizations were carried out using X-ray diffractometer (XRD), vibrating sample magnetometer (VSM), and field emission scanning electron microscope (FE-SEM).

3. Results and Discussion

3.1. X-Ray Diffraction Measurements. Figure 1 shows the XRD spectra for $\text{Er}_x\text{Y}_{3-x}\text{Fe}_5\text{O}_{12}$ thin films, ($0 \leq x \leq 2.5$) annealed at 1000°C for 2 hours. All of the samples show single phases with diffraction lines (hkl) corresponding to the cubic garnet structure. The family of planes (hkl) in the Er-YIG structure and the corresponding distance between two lattice planes d_{hkl} calculated from the experimental data are shown in Table 1. The theory data is according to the reference spectrum of a pure cubic garnet single phase formation YIG (JCPDS card no: 01-070-0953). The main peaks for $x = 1.2$, 2.0 and $x = 2.5$ belonging to (321) reflection plane originated at the $2\theta^\circ$ values of 27.014, 27.022, and 27.031 correspond to the spacing values of 3.298, 3.297, and 3.296 Å, respectively, which is one of the cubic garnet single phase formation according to the reference spectrum of (EIG) card no: 01-081-0131.

The lattice parameter “a” was calculated from combination of Bragg’s equation and d-spacing expression for cubic

system using the formula:

$$a = \left[\frac{\lambda^2}{4 \sin^2 \theta} (h^2 + k^2 + l^2) \right]^{1/2}, \quad (1)$$

where λ is the wavelength of Cu $k\alpha$ radiation with 1.54060 Å, θ = diffraction angle of X-rays.

The average crystallite size was calculated according to the Scherrer’s equation,

$$D = \frac{k\lambda}{\beta \cos \theta}, \quad (2)$$

where D is the mean crystallite size, k (0.89) is the Scherrer constant, λ is X-ray wavelength (0.154252 nm), and β is the relative value of the full width at half maximum (FWHM) of the diffraction peak (420). Table 2 summarizes the results of lattice constant and crystallite size of $\text{Er}_x\text{Y}_{3-x}\text{Fe}_5\text{O}_{12}$ thin films.

3.2. Nanostructural Properties. The purpose of FESEM analysis was to determine the grain size and to understand the process of grain growth. The nanostructures of all of the samples were studied using the field emission scanning electron microscope (FE-SEM) at the magnification of 300,000X (Figure 2). Most of the particles stuck to each other and form agglomerates due to their high surface energy [31]. The FESEM micrograph exhibited highly agglomerated particles having an average particle size of 82 nm. It was observed that the average particle size measured by FESEM is bigger than crystallite size measured by Scherrer’s formula. This means that the particles are not single crystals and may consist of 2 or 3 and more crystallites.

The samples were coated with thin layer of gold to avoid electrostatic charging during examination. The grains could not be seen clearly. This may be because of masking caused by the gold coating on the film’s surface. The average grain size is estimated from the FESEM and from the sample’s cross section for ($x = 0$). The small grains on the surface belong to the gold particles (10–20 nm). The formation of cracks and voids can be attributed to the lattice mismatch. Cracks can easily be generated in crystallized Er-YIG thin films. The FESEM was also used to measure the films thicknesses and the result was 380 nm. It should be noted that all preparation parameters that influence the film thickness such as the sol concentration, spinning rate, spinning duration, and amount of sol on the substrate were kept constant. The changing factor was only the x value in this study.

3.3. Magnetic Properties. The magnetic properties of the films were measured using the vibrating samples magnetometer (VSM) with a maximum applied field of 12 kOe at room temperature (25°C). Figure 3 shows the in-plane hysteresis loop for all of the films. The hysteresis curves indicate that the Er-YIG films annealed at 1000°C are soft magnetic materials.

The saturation magnetization (M_s) of the films decreased in a linear manner with the increment of Er concentration (x) (Figure 4(a)), and this can be related to the fact that

TABLE 1: The experimental data for Er-YIG structure.

(hkl)	(321)	(400)	(420)	(422)	(521)	(611)	(444)	(640)	(642)	(800)	(840)	(842)
$d_{hkl} (\pm 0.005) \text{ \AA}$	3.308	3.088	2.763	2.522	2.256	2.004	1.783	1.714	1.651	1.543	1.382	1.348

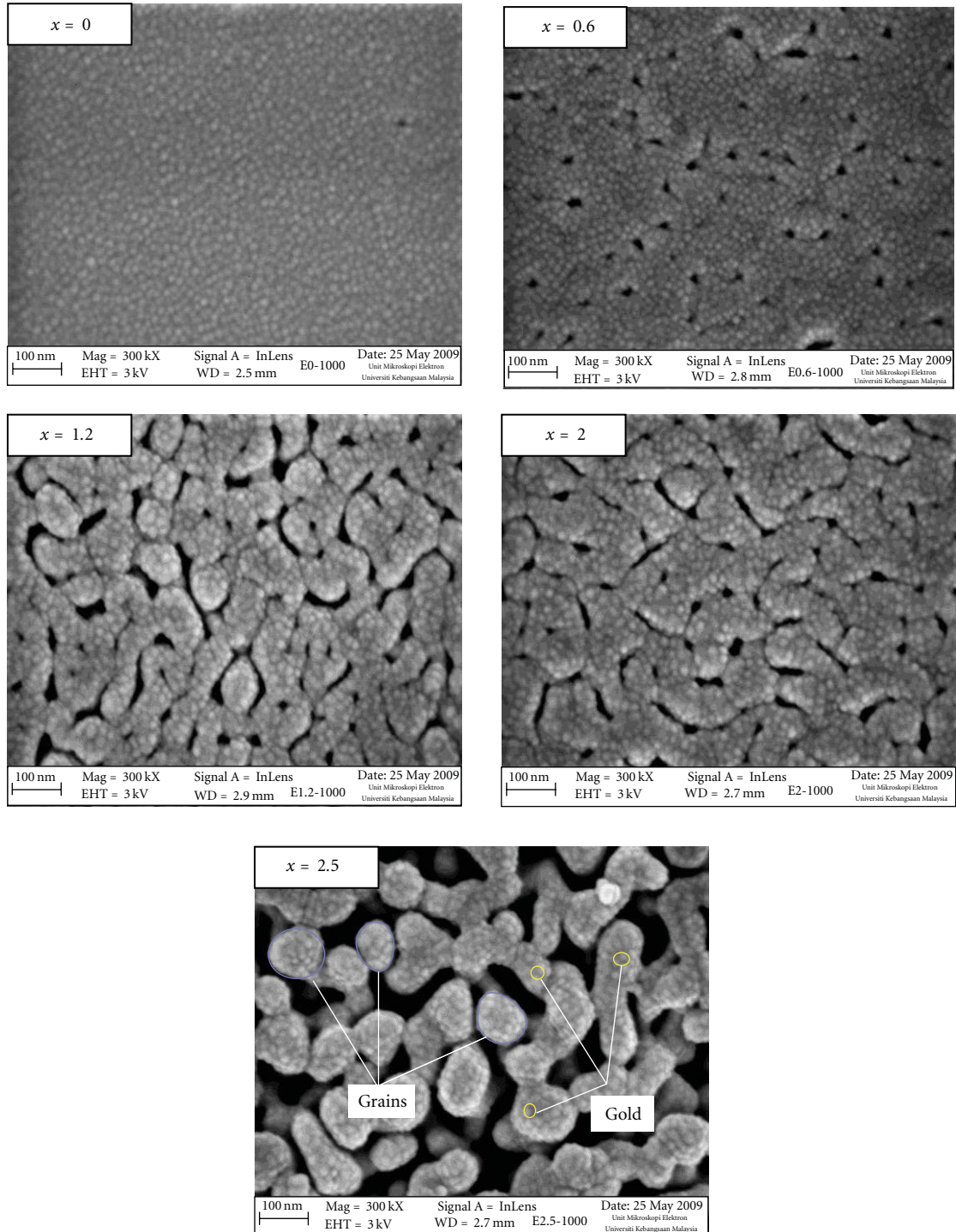


FIGURE 2: FE-SEM micrographs of $Er_xY_{3-x}Fe_5O_{12}$ thin films.

TABLE 2: Lattice constant “a” and crystallite size of Er-YIG thin films.

(x)	Lattice constant (Å)	Crystal size (nm)
0.0	12.354	24
0.6	12.338	21
1.2	12.324	23
2.0	12.325	24
2.5	12.320	23

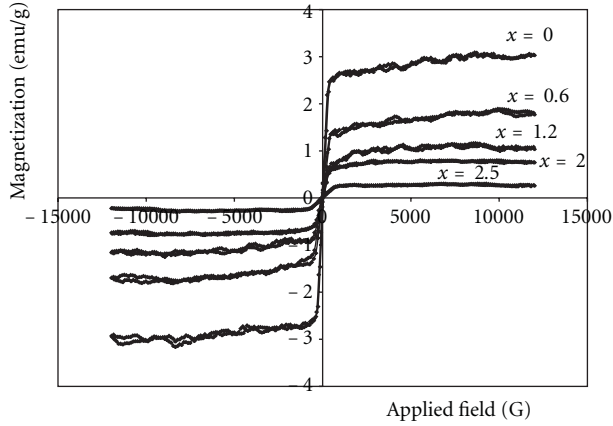
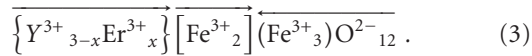
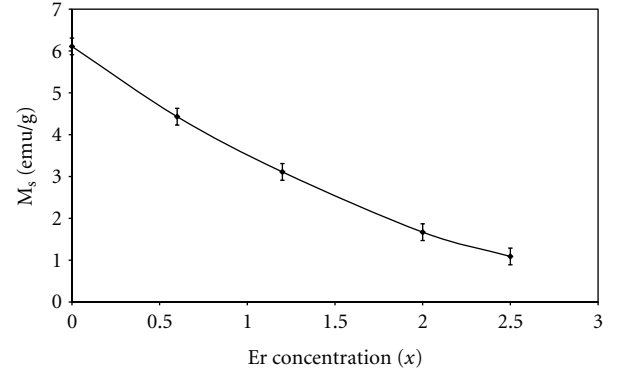


FIGURE 3: Hysteresis loop curve at 1000°C for $\text{Er}_x\text{Y}_{3-x}\text{Fe}_5\text{O}_{12}$ thin films.

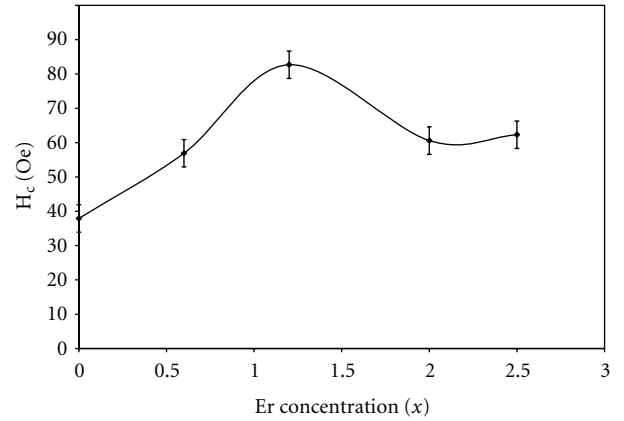
the magnetic moments of Er^{3+} ions align oppositely to the effective moments formed by Fe^{3+} ions [18]. According to Néel’s theory [32], there exist three magnetic sublattices in YIG: one {c} formed by the Er^{3+} ions occupying the dodecahedral sites, another [a] formed by Fe^{3+} ions occupying the octahedral sites and the third (d) formed by the Fe^{3+} ions occupying the tetrahedral sites. The two iron sublattices are coupled antiferromagnetically by the superexchange interaction acting via the intervening O^{2-} ions. The {c} sublattice is coupled antiferromagnetically with the two iron sublattices. At room temperature, the three sublattices moments align along the [111] direction. Therefore, the magnetic structure for such a mixed garnet can be represented by writing the garnet formula as



The net magnetic moments is $M = M_c - |Md - Ma|$. The coercivity (H_c) increases with x for $x = 0.0-1.2$, then decreases for $x = 1.2-2.5$ as shown in (Figure 4(b)). This can be due to nanometer particles of the films. When the particle size is about 89 nm, the coercivity of $\text{Er}_x\text{Y}_{3-x}\text{Fe}_5\text{O}_{12}$ ($0 \leq x \leq 2.5$) nanoparticles reached the greatest values. The magnetic properties of a magnetic material depend largely on the particle size distributions as the domain structure and magnetization process depends on particle size [33]. When the particle size is much larger than the critical size of a single domain, the coercivity is decided by magnetic displacement, so the value of coercivity is small. When the particle size is reduced to the critical size of single domain, the coercivity



(a)



(b)

FIGURE 4: The variation of (a) saturation magnetization and (b) coercivity with Er concentration for $\text{Er}_x\text{Y}_{3-x}\text{Fe}_5\text{O}_{12}$ thin films.

is decided by magnetic domain rotation, so the coercivity reaches the maximum. When the particle size is less than the critical size of single domain, the coercivity will be decreased for the existence of superparamagnetism [34].

4. Conclusion

Thin films of $\text{Er}_x\text{Y}_{3-x}\text{Fe}_5\text{O}_{12}$, ($x = 0.0, 0.6, 1.2, 2.0,$ and 2.5) have been prepared using a sol-gel method. The X-ray diffraction characterization shows that all of the samples have only a single phase garnet structure. The crystalline films are soft magnetic materials. The saturation magnetization is reduced with Er substitution because the magnetic moments of Er^{3+} ions coupled antiferromagnetically to the effective moment formed by Fe^{3+} ions. The coercivity of the films is maximum for $x = 1.2$. The coercivity for the nanocrystalline materials is small when they are in their multidomain state and it is maximum at the critical single domain size and decreases further with a reduction in grain size as it approaches superparamagnetism as the thermal energy is comparable to the anisotropy energy.

Acknowledgment

The authors would like to thank MOSTI for the science fund grant 03-01-02-SF0538.

References

- [1] M. Lahoubi, M. Guillot, A. Marchand, F. Tcheou, and E. Roudault, "Double umbrella structure in terbium iron garnet," *IEEE Transactions on Magnetics*, vol. 20, no. 5, pp. 1518–1520, 1984.
- [2] Y. Konishi, *Microwave Integrated Circuit*, Marcel-Dekker, New York, NY, USA, 1991.
- [3] M. A. Gilleo, "Ferromagnetic insulators: garnets," in *Ferromagnetic Materials*, Vol. 2, E. P. Wohlfarth, Ed., chapter 1, North-Holland, Amsterdam, The Netherlands, 1980.
- [4] S. Thongmee, P. Winotai, and I. M. Tang, "Local field fluctuations in the substituted aluminum iron garnets, $Y_3Fe_{5-x}Al_xO_{12}$," *Solid State Communications*, vol. 109, no. 7, pp. 471–476, 1999.
- [5] M. S. Lataifeh, "Magnetic study of Al-substituted holmium iron garnet," *Journal of the Physical Society of Japan*, vol. 69, no. 7, pp. 2280–2282, 2000.
- [6] M. J. Geselbracht, A. M. Cappellari, A. B. Ellis, M. A. Rzeznik, and B. J. Johnson, "Rare earth iron garnets: their synthesis and magnetic properties," *Journal of Chemical Education*, vol. 71, no. 8, pp. 696–703, 1994.
- [7] M. S. Lataifeh and A. Al-sharif, "Magnetization measurements on some rare-earth iron garnets," *Applied Physics A Materials Science & Processing*, vol. 61, no. 4, pp. 415–418, 1995.
- [8] M. S. Lataifeh, A. D. Lehlooh, and S. Mahmood, "Mössbauer spectroscopy of Al substituted Fe in holmium iron garnet," *Hyperfine Interactions*, vol. 122, no. 3-4, pp. 253–258, 1999.
- [9] M. Inoue, K. Arai, T. Fujii, and M. Abe, "Magneto-optical properties of one-dimensional photonic crystals composed of magnetic and dielectric layers," *Journal of Applied Physics*, vol. 83, no. 11, pp. 6768–6770, 1998.
- [10] M. Gomi, K. Satoh, and M. Abe, "New garnet films with giant Faraday rotation," in *Proceedings of the 5th International Conference on Ferrites*, C. M. Srivastava and M. J. Patni, Eds., pp. 919–924, Oxford and IBH, 1989.
- [11] T. Shintaku and T. Uno, "Preparation of Ce-substituted yttrium iron garnet films for magneto-optic waveguide devices," *Japanese Journal of Applied Physics*, vol. 35, no. 9A, pp. 4689–4691, 1996.
- [12] A. Tate, T. Uno, S. Mino, A. Shibukawa, and T. Shintaku, "Crystallinity of Ce substituted YIG films prepared by RF sputtering," *Japanese Journal of Applied Physics*, vol. 35, no. 6, pp. 3419–3425, 1996.
- [13] T. Shintaku, A. Tate, and S. Mino, "Ce-substituted yttrium iron garnet films prepared on $Gd_3Sc_2Ga_3O_{12}$ garnet substrates by sputter epitaxy," *Applied Physics Letters*, vol. 71, no. 12, pp. 1640–1642, 1997.
- [14] C. Y. Tsay, C. Y. Liu, K. S. Liu, I. N. Lin, L. J. Hu, and T. S. Yeh, "Low temperature sintering of microwave magnetic garnet materials," *Journal of Magnetism and Magnetic Materials*, vol. 239, no. 1-3, pp. 490–494, 2002.
- [15] H. Hayashi, S. Iwasa, N. J. Vasa et al., "Fabrication of Bi-doped YIG optical thin film for electric current sensor by pulsed laser deposition," *Applied Surface Science*, vol. 197-198, pp. 463–466, 2002.
- [16] M. Huang and S. Zhang, "Growth and characterization of rare-earth iron garnet single crystals modified by bismuth and ytterbium substituted for yttrium," *Materials Chemistry and Physics*, vol. 73, no. 2-3, pp. 314–317, 2002.
- [17] M. C. Sekhar, J.-Y. Hwang, M. Ferrera et al., "Strong enhancement of the Faraday rotation in Ce and Bi comodified epitaxial iron garnet thin films," *Applied Physics Letters*, vol. 94, no. 18, Article ID 181916, 2009.
- [18] H. Xu, H. Yang, and L. Lu, "Effect of erbium oxide on synthesis and magnetic properties of yttrium-iron garnet nanoparticles in organic medium," *Journal of Materials Science: Materials in Electronics*, vol. 19, no. 6, pp. 509–513, 2008.
- [19] N. I. Tsidaeva, "The magneto-optical activity of rare-earth ion in Y-substituted erbium and neodymium iron garnets," *Journal of Alloys and Compounds*, vol. 408–412, pp. 164–168, 2006.
- [20] J. Ostoréro and M. Guillot, "High field induced magnetic anisotropy of Al-substituted erbium iron garnet single crystals," *IEEE Transactions on Magnetics*, vol. 37, no. 4, pp. 2441–2444, 2001.
- [21] P. Novák, V. A. Borodin, V. D. Doroshev, M. M. Savosta, and T. N. Tarasenko, "NMR of Fe in erbium-yttrium iron garnets," *Hyperfine Interactions*, vol. 59, no. 1–4, pp. 427–430, 1990.
- [22] P. Feldmann, M. Guillot, H. Le Gall, and A. Marchand, "Faraday rotation in erbium-yttrium iron garnet," *IEEE Transactions on Magnetics*, vol. 17, no. 6, pp. 3217–3219, 1981.
- [23] N. Tsidaeva and V. Abaeva, "The investigation of mechanisms of the magneto-optical activity of rare-earth iron garnet single crystals," *Journal of Alloys and Compounds*, vol. 418, no. 1-2, pp. 145–150, 2006.
- [24] N. I. Tsidaeva, "The magnetic and magneto-optical properties of Y-substituted erbium iron garnet single crystals," *Journal of Alloys and Compounds*, vol. 374, no. 1-2, pp. 160–164, 2004.
- [25] P. Feldmann, H. Le Gall, M. Guillot, and A. Marchand, "Anisotropy of the Faraday rotation in erbium-yttrium iron garnet below the compensation temperature," *Journal of Applied Physics*, vol. 53, no. 3, pp. 2486–2488, 1982.
- [26] J. Ostoréro and M. Guillot, "Magneto-optical properties of Sc-substituted erbium-iron-garnet single crystals," *Journal of Applied Physics*, vol. 83, no. 11, pp. 6756–6758, 1998.
- [27] P. Feldmann, H. Le Gall, J. M. Desvignes, M. Guillot, and A. Marchand, "Faraday rotation in single crystal erbium iron garnet," *Journal of Magnetism and Magnetic Materials*, vol. 21, no. 3, pp. 280–284, 1980.
- [28] R. D. Shannon and C. T. Prewitt, "Revised values of effective ionic radii," *Acta Crystallographica Section B*, vol. 26, no. 7, pp. 1046–1048, 1970.
- [29] Y. Q. Jia, "Crystal radii and effective ionic radii of the rare earth ions," *Journal of Solid State Chemistry*, vol. 95, no. 1, pp. 184–187, 1991.
- [30] A. Di Biccari, "Sol-gel processing of $R_xY_{3-x}Al_yFe_{5-y}O_{12}$ magneto-optical films," M.S. thesis, Materials Science & Engineering Department, Blacksburg, Va, USA, 2002.
- [31] S. Verma, S. D. Pradhan, R. Pasricha, S. R. Sainkar, and P. A. Joy, "A novel low-temperature synthesis of nanosized NiZn ferrite," *Journal of the American Ceramic Society*, vol. 88, no. 9, pp. 2597–2599, 2005.
- [32] D. Rodica, M. Mitric, R. Tellgren, H. R. Rundlof, and A. Kremenovic, "True magnetic structure of the ferrimagnetic garnet $Y_3Fe_5O_{12}$ and magnetic moments of iron ions," *Journal of Magnetism and Magnetic Materials*, vol. 191, no. 1-2, pp. 137–145, 1999.
- [33] S. Chikazumi, *Physics of Magnetism*, Wiley, New York, NY, USA, 1964.
- [34] L. Zhao, H. Yang, Y. Cui, X. Zhao, and S. Feng, "Study of preparation and magnetic properties of silica-coated cobalt ferrite nanocomposites," *Journal of Materials Science*, vol. 42, no. 11, pp. 4110–4114, 2007.